TÉCNICO LISBOA

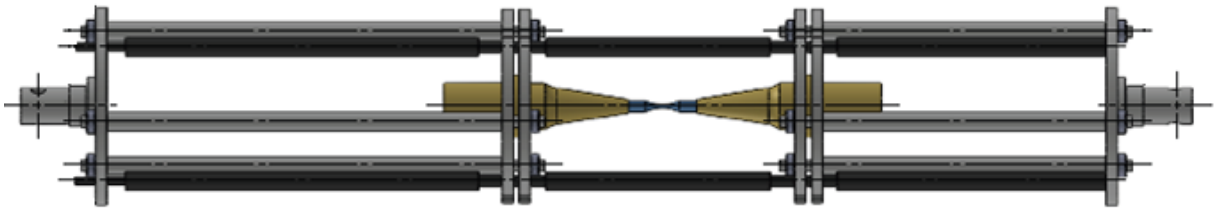

Development of an Equipment for Conducting Fatigue Tests in the VHCF Regime with Stress Ratios other than -1

Margarida Barroso Paiva Gonçalves Verdade

Thesis to obtain the Master of Science Degree in

Mechanical Engineering

Supervisors: Prof. Luís Filipe Galrão dos Reis
Dr. Pedro Ferreira Rodrigues da Costa

Examination Committee

Chairperson: Prof. Paulo Rui Alves Fernandes
Supervisor: Prof. Luís Filipe Galrão dos Reis
Member of the Committee: Prof. Rui Fernando dos Santos Pereira Martins

November 2022

Declaration

I declare that this document is an original work of my own authorship and that it fulfills all the requirements of the Code of Conduct and Good Practices of the Universidade de Lisboa.

Acknowledgments

First and foremost, I would like to thank my supervisors, Prof. Luís Reis and Dr. Pedro Costa, for their assistance, and without whom this dissertation would not have been possible. Additionally, I would like to express my gratitude to Pedro Teixeira and João Vicente for their patience and wise advice concerning the manufacturing processes, which represented an important part of the development of this dissertation. I am grateful to my colleague and friend José Henrique Lopes, for being present throughout all stages of this dissertation, and with whom I shared my accomplishments and concerns. I would also like to acknowledge Frederico Alves for his helpful input regarding the use of Siemens Software NX™.

I would like to express a special thanks to my boyfriend João Ribeiro for his love, patience, kind advice, and for being present in every moment along the way, especially in those I could not endure alone. I am further grateful to my beloved friends Leonor Campos, Rafael Sousa, Sofia Gonçalves, and Ana Faria for their unconditional support concerning not only my academic journey but also every other aspect of my life.

Finally, but not less important, I would like to express my profound gratitude to my parents and grandparents for never failing to provide me with the all the support I needed to complete this journey, and for always having faith in me. I hope I can make you proud.

Financial support from Portuguese Fundação para a Ciência e Tecnologia (FCT) is acknowledged through project PTDC/EME-EME/7678/2020, Giga-Cycle Fatigue Behaviour of Engineering Metallic Alloys.

Resumo

Esta dissertação detalha o desenvolvimento de um sistema ultrassónico e de uma estrutura de suporte para conduzir ensaios de fadiga em condições axiais no regime de muito elevado número de ciclos com tensão média aplicada diferente de zero ($R \neq -1$). Dimensionou-se o sistema para ser introduzido numa máquina eletromecânica para aplicar e controlar a carga estática de tração imposta. Os componentes mecânicos do sistema ultrassónico foram projetados através de um processo iterativo recorrendo ao método dos elementos finitos. O sistema ultrassónico foi projetado de forma que a frequência de ressonância do modo de vibração axial desejado fosse de 20 kHz. Conduziram-se análises experimentais para avaliar o comportamento do sistema ultrassónico desenvolvido sob diferentes condições de carregamento. A relação tensão-deslocamento foi avaliada (i) analiticamente, usando as equações da literatura, (ii) numericamente, através de uma análise de elementos finitos, e (iii) experimentalmente, utilizando como instrumentos de medida um extensómetro e um laser. Desenvolveu-se uma metodologia para estabelecer as condições ultrassónicas para a realização dos testes de fadiga com tensão média especificada diferente de zero. Por fim, realizou-se ensaios de fadiga para provetes idênticos utilizando o sistema desenvolvido, apresentando-se os resultados de vida à fadiga e análises das respetivas superfícies de fratura. Os resultados obtidos demonstram que o sistema permite a realização de ensaios de fadiga com rácios de tensão diferentes de -1, e que se pode recorrer aos métodos analíticos ao invés dos demorados métodos numéricos para determinar a relação tensão-deslocamento, uma vez que foi possível provar que ambos os métodos levam a resultados semelhantes.

Palavras-chave: Fadiga Ultrassónica, Rácio de Tensão, Tensão Média, Frequência de Ressonância, Método dos Elementos Finitos, Método Analítico

Abstract

This dissertation details the development of an ultrasonic system and support structure which allow for conducting fatigue tests under axial conditions in the very high cycle regime with a superimposed mean stress ($R \neq -1$). The overall mechanical system was designed to fit into an electromechanical machine which applies and controls the tensile static load imposed onto the system. The mechanical components of the ultrasonic system were designed through an iterative process using the finite-element method. The ultrasonic system was designed in such a way that the resonance frequency of the required axial mode of vibration is of 20 kHz. Experimental analyses were then conducted to evaluate the mechanical behaviour of the developed ultrasonic system under different loading conditions. The stress-displacement relation was evaluated (i) analytically using the equations provided by the available literature, (ii) numerically resorting to a finite-element analysis, and (iii) experimentally using as instruments a strain gauge and a laser vibrometer. Additionally, a methodology for establishing the desired ultrasonic conditions for conducting the fatigue tests with a superimposed mean stress was drawn. Finally, fatigue tests were conducted for identical specimens using the developed mechanical system, and the fatigue results and fracture surfaces analyses were presented. The obtained results demonstrate that the developed system and support structure allow for experimentally conduct fatigue tests with stress ratios different from -1, and that one may resort to the analytical methods rather than the time consuming numerical ones to determine the stress-displacement relation, since these two methods have proven to lead to similar results.

Keywords: Very High Cycle Fatigue, Stress Ratio, Mean Stress, Resonance Frequency, Finite Element Method, Analytical Method

Contents

List of Tables

List of Figures

Chapter 1

Introduction

Today's society has become increasingly more dependent on mechanical technology. For example, the number of flights between 2004 and pre-COVID 2020 has risen from 23.8 to 40.3 million per year[1]. These numbers strongly showcase a growing need to guarantee the safety and reliability of aircraft and their mechanical components. Traditional methods for studying the lifetime of mechanical components relied on statistical analyses (Bathias, 1999). However, according to Bathias (1999), the problem with these approaches is that the predicted lifespans not always match the real lifespans of the mechanical components, and one way of mitigating this issue is to evaluate the mechanical components' materials, resorting to *very high cycle fatigue* (VHCF) testing. When mentioned in the context of material's behaviour, fatigue refers to the phenomenon consisting on the initiation and propagation of cracks in a given material due to being subjected to cyclic loadings. This phenomenon represents 90% of the failures in elements of engineering applications (Lesperance et al., 2021). For this reason, the study of fatigue in materials subjected to a very high number of loading cycles is crucial to the design of more reliable mechanical components.

Fatigue is considered to be a by-product of the 19^{th} century Industrial Revolution, since the length, in km, of railway axles was significantly increasing in countries such as Great Britain, France, Germany and Russia (Zenner and Hinkelmann, 2019). By that time, serious accidents started to happen often, caused mostly by axles, couplings and rail failure, with catastrophic consequences. Inevitably, the importance of this phenomenon became evident and, in the middle of the 19^{th} century, August Wöhler, who is for many the founding father of fatigue strength research (Zenner and Hinkelmann, 2019), proved that materials may, in fact, fail when subjected to cyclic stresses far below its static strength.

Over the past decades (and particularly nowadays), the consequences of energy, climate and war crises have become increasingly evident, becoming the catalysts for energy transition policies. According to Gielen et al. (2019), renewable energies play the most important role, since its share on the total primary energy supply is presumed to grow from 15% in 2015 to 63% in 2050. The authors also state that wind and solar photovoltaic technologies are expected to be the ones with the highest growth. Modern wind turbines are highly prone to fatigue failure, since they are expected to operate at a very

[1] `https://financesonline.com/number-of-flights-worldwide/`

high number of rotating cycles while subjected to dynamic loads. Catastrophic failures may lead to injuries, fatalities, shortage of energy supply and economic losses. Moreover, economic crises may also contribute to extend the service time beyond the design life of certain structures or machines, due to difficulties associated with their replacement (Sakai et al., 2006).

The fact that scientists and engineers are nowadays aware of the possibility of a catastrophic failure of materials due to gigacycle fatigue, the evaluation of the materials behaviour in the VHCF regime in a quantitative, reliable, rigorous and more economic way has become of extreme importance, justifying the growing need for ultrasonic fatigue testing machines.

1.1 Objectives

This dissertation contributes to the scientific community by designing, manufacturing and evaluating both a support structure and an ultrasonic system assembled into an electromechanical machine with the purpose of testing materials in the VHCF regime. The ultrasonic system allows for specimens' fatigue testing and the support structure allows for the imposition of an applied static load. Both an analytical and a numerical evaluation of the stress-displacement relation (which relates the maximum stress in the specimen with the displacement amplitude of the lower end of the ultrasonic system) were performed alongside an experimental evaluation of the overall system in a laboratory environment. The experimental stress-displacement relation was then compared against the ones obtained by the analytical and numerical evaluations (with a 10.23% and 11.16% difference, respectively). Finally, fatigue tests were conducted on two identical specimens.

1.2 Outline

The remainder of this dissertation is organised as follows. **Chapter 2** addresses the need for ultrasonic fatigue testing machines and presents their working principle. The necessary scientific concepts required for the comprehension of this document are also provided alongside the equations needed to conduct the analytical analysis of an axisymmetric specimen of variable section. The chapter then concludes by presenting some available literature in the field. **Chapter 3** introduces the structural elements developed while detailing the design, assembling and disassembling procedures of the ultrasonic system and support structure. It also details the properties of the materials used throughout the different analyses. **Chapter 4** details the employed methodology to obtain the horns' geometry and two different specimens, detailing the conducted analytical and numerical analyses. It then discusses the results obtained for each individual component, and the overall ultrasonic system under different loading conditions. **Chapter 5** fully details the experimental procedures and their respective results, discussing and comparing the findings with the ones obtained by both the analytical and numerical evaluations. It also presents a method for conducting ultrasonic fatigue tests with a superimposed mean stress. It concludes by showcasing the results obtained in the fatigue tests using two identical specimens. Finally **Chapter 6** concludes the dissertation and discusses possible future lines of work.

Chapter 2

Background

This chapter introduces the core concepts used throughout the dissertation, and the working principle of ultrasonic fatigue testing machines and the analytical solution of the specimen to be employed. Finally, some available literature in the field regarding ultrasonic fatigue testing under axial and non-axial conditions are presented.

2.1 Fatigue in the Very High Cycle Regime

There are three base conditions that must be verified simultaneously so that fatigue can occur, which are the presence of (i) cyclic loading, (ii) local plastic deformation and (iii) tensile stresses. Naturally, compressive stresses are not capable of propagating any existent cracks. In a given situation, where all three conditions are present, one existent crack grows extremely slowly with each loading cycle, until it reaches a critical size. Once the critical size is reached, the crack propagates fast, leading to a sudden and total failure of the mechanical component, often called *catastrophic failure*. Even for cyclic load amplitudes lower than the yield stress of the material, fatigue failure may still occur (de Moura Branco, 1998).

From Wöhler's experiments resulted the very first S-N curves (Bathias and Paris, 2005), also known as Wöhler curves (Figure 2.1a). These curves show the evolution of fatigue strength, S_f, as the number of loading cycles, N, increases. The classic S-N curves show one horizontal asymptote for high number of cycles, denoting the existence of a fatigue limit, i.e., an endurance limit.

In the words of Schijve (2003), the fatigue limit "is the stress amplitude for which the fatigue life becomes infinite in view of the asymptotic character of the S-N curve". This horizontal line is representative of an unrealistic situation, meaning that if the material did not fail after a high number of cycles, typically $10^6 - 10^7$ cycles, then it would almost surely never fail as the number of cycles continues to increase.

In 1999, after conducting several experiments, Claude Bathias, showed that even after 10^7 cycles, fatigue failure could still occur in many alloys. On top of that, Bathias was also able to quantify the decrease of the fatigue resistance, stating that in some cases this value could decrease up to 100 MPa or even 200 MPa (Bathias, 1999). The established 'fatigue limit' definition, largely used and statistically

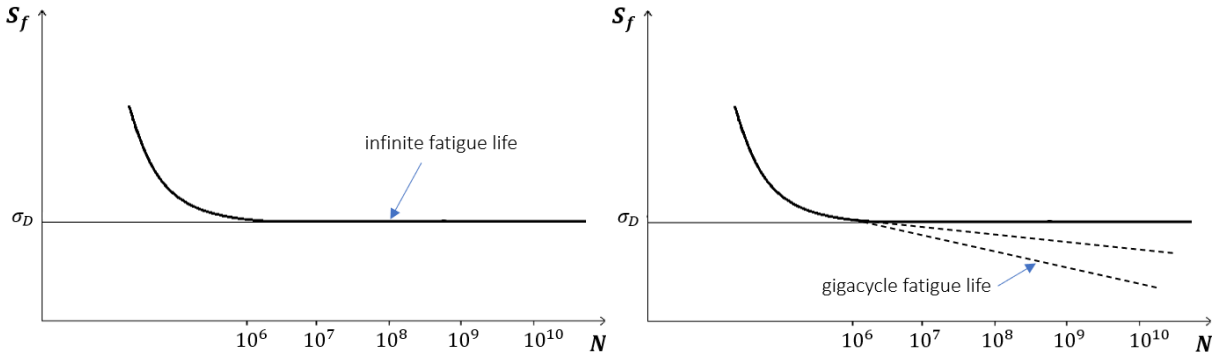

Figure 2.1: The concepts of infinite and gigacycle fatigue life (adapted from (Bathias and Paris, 2005)).

determined, was proven to be misaligned with reality. Such studies, along with experiments conducted by Marines et al. (2003), Pyttel et al. (2011) and Mayer et al. (2013), among others, corroborate the hypothesis that statistical analysis does not guarantee safety for several materials, since the S-N curves in the gigacycle regime in several cases do not have an horizontal asymptote, meaning an infinite life does not exist (figure 2.1b). Consequently, the terms *gigacycle regime* and *very high cycle regime* entered the scientists vocabulary. This regime occurs between 10^7 and 10^{12} loading cycles, and any fatigue phenomenon materialising in this regime is called *gigacycle fatigue* or *very high cycle fatigue* (VHCF).

Until the beginning of the 20^{th} century, the popularity of statistical methods to foresee the S-N curves of materials in the VHCF regime was due to their economical convenience. If the fatigue tests were to be performed in a conventional machine at 100 Hz up to 10^8 cycles, the time needed to complete one test in one specimen was of 300 hours. Naturally, this was not economically feasible, justifying the need of statistical methods to foresee the behaviour of materials under high number of load cycles. Nevertheless, relying on a statistical estimate of the fatigue limit for a very high number of loading cycles is not a reliable approach to evaluate the S-N curves behaviour in the gigacycle regime, thus it is necessary to resort to methods different from the conventional ones. Hence, new testing devices are needed. In this sense, ultrasonic fatigue testing machines started being developed during the 20^{th} century.

2.2 Working Principle of Ultrasonic Fatigue Testing Machines

What distinguishes an ultrasonic fatigue machine from a conventional one is the machine's working frequency. While conventional machines are limited to 100 Hz, the ultrasonic ones operate at frequencies much higher, typically 20 kHz. Nevertheless, the frequency range from ultrasonic machines can go from 15 kHz to 30 kHz. This new machines accelerate the testing process, allowing to theoretically test materials up to 10^9 cycles in just 14 hours. If the same test were to be performed in a conventional machine, it would take 3 years to test one single specimen (Bathias and Paris, 2005). Ultrasonic fatigue testing machines enables researchers to progress faster by conducting fatigue tests up to the gigacycle

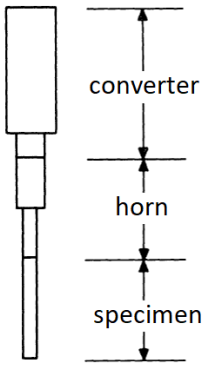

Figure 2.2: Compulsory elements to perform ultrasonic fatigue tests. Adapted from Willertz (1980).

regime in a short period of time and economising at the same time.

The essential components for every ultrasonic fatigue testing machine are (i) a power supply unit, (ii) a piezoelectric (or magnetostrictive) transducer, (iii) one or more ultrasonic horns, with or without boosters, (iv) a specimen, and (v) a control unit. Figure 2.2 is a generic representation of the basic structure needed to perform the experiments.

The power supply unit transforms a electrical signal of 50 or 60 Hz from the grid into a sinusoidal electrical signal of much higher frequency, typically 20 kHz. Connected to the power supply unit, there is the piezoelectric transducer, also called *converter*, which proportionally transforms the incoming electrical signal of 20 kHz into a longitudinal ultrasonic mechanical wave of the same frequency. The mechanical wave is then induced into the ultrasonic horn coupled to the converter. The horn and the booster amplify the displacement amplitude of the mechanical wave generated by the transducer (Soares et al., 2018). Ultrasonic horns are designed to undergo the highest displacement amplitudes in the section in contact with the specimen. Depending on the type of loading imposed onto the specimen, its geometry may vary. Every fatigue test must be conducted with a control unit support, which programmes, controls, records and measures the applied load, assuring all components vibrate at the required frequency during the whole experiment, while also collecting data from the experiment. Cooling systems are also often incorporated in the ultrasonic fatigue testing machines, such as cooling fans.

The working principle of ultrasonic fatigue tests is based on the natural frequency of the components. Taking the example of Figure 2.2, where the mechanical wave is induced longitudinally into the load train, if the working frequency of the converter is 20 kHz, then the horn, booster, and specimen must be designed so that their individual natural frequency at their desired longitudinal mode matches the 20 kHz. Altogether, the ultrasonic set must resonate at 20 kHz at the required longitudinal mode. If the fatigue tests were to be performed under torsional or bending loads, the design of the ultrasonic set would have to be designed accordingly.

During an ultrasonic fatigue experiment, the presence of all vibration modes (axial, bending, torsion) is inevitable. It is the designer responsibility to guarantee that the resonance frequencies of the undesirable vibration modes are sufficiently distanced from the working mode. Therefore, one must ensure that the influence of the undesired modes on the ultrasonic set performance is negligible.

2.3 Ultrasonic Fatigue Concepts

2.3.1 Wave Interference

Mechanical waves are disturbances that propagate in a medium. The simplest waves oscillate periodically with a fixed frequency and wavelength[1]. Waves behave differently when encountering obstacles of distinct natures, for example, if an acoustical wave travelling in a medium encounters a physical obstacle, it will be reflected back.

A wave with no sense of motion is a *standing* or *stationary wave*. Standing waves result from the interference of two waves with the same exact frequency and amplitude. If both waves are propagating in the same direction, the result of their interference is a moving wave, whereas if they are propagating in opposite directions, the resulting wave appears to be fixed in space. Standing waves may therefore be a result of the interaction between an incident and a reflected wave. When interference occurs, the waves energies may either cancel one another (destructive interference) or add to one another (constructive interference)[2].

Figure 2.3a represents two identical sinusoidal waves, y_1 and y_2, with equal amplitudes, frequencies and phases, propagating in the same medium but in opposite directions. Wave functions y_1 and y_2 are given by equation 2.1. Although Figure 2.3b represents an identical situation, in this scenario the sinusoidal waves are out of phase, diverging by $180°$. Consequently both waves compensate for one another, resulting in destructive interference. In this situation both waves cancel each other (Serway and Jewett, 2018).

$$y_1 = A\sin(kx - \omega t) \quad y_2 = A\sin(kx - \omega t) \tag{2.1}$$

Interference between both sinusoidal waves occurs, hence the resulting wave is a standing wave of function $y = y_1 + y_2$, which may be rewritten as equation 2.2.

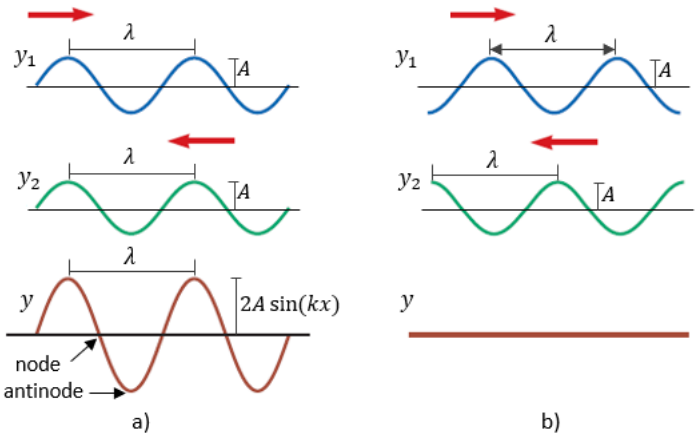

Figure 2.3: The mechanism of wave interference. a) Constructive interference. b) Destructive interference. Adapted from (Serway and Jewett, 2018).

[1] https://www.britannica.com/science/wave-physics
[2] https://www.britannica.com/science/standing-wave-physics

$$y = (2A \sin kx) \cos \omega t \tag{2.2}$$

In equation 2.2 A is the amplitude of both incident and reflected waves, $2A \sin(kx)$ is the amplitude of the standing wave and ω is the angular frequency. This equation describes a simple harmonic motion where all elements of the medium oscillate at the same angular frequency. Equation 2.2 indicates that the displacement amplitude of a standing wave is zero for values of x that verify the following condition:

$$kx = 0, \pi, 2\pi, 3\pi, ... \tag{2.3}$$

Since $k = \frac{2\pi}{\lambda}$, then the standing wave displacement amplitude is zero for the values of x presented in equation 2.4. These points are the wave *nodes*.

$$x = 0, \frac{\lambda}{2}, \lambda, \frac{3\lambda}{2} ... = \frac{n\lambda}{2}, \quad \text{for } \; x = 0, 1, 2, 3, ... \tag{2.4}$$

On the contrary, the *antinodes* are the values of x for which the displacement amplitude is the greatest. The values of x that verify the condition $kx = \pm 1$ give the antinodes position along the longitudinal axis. Such condition may also be written in the form presented in equation 2.5.

$$kx = \frac{\pi}{2}, \frac{3\pi}{2}, \frac{5\pi}{2}, ... \tag{2.5}$$

The x values in equation 2.6 verify condition 2.5, so they are called the wave *antinodes*.

$$x = \frac{\lambda}{4}, \frac{3\lambda}{4}, \frac{5\lambda}{4}, ... \tag{2.6}$$

These considerations lead to the conclusion that the gap between two consecutive nodes is $\lambda/2$. The same conclusion applies to two consecutive antinodes, whereas the gap between a node and an adjacent antinode is equal to $\lambda/4$.

One typical scenario leading to constructive interference in ultrasonic fatigue testing is the one where a mechanical wave is propagating through the ultrasonic set, and when it hits the free end of the specimen, it is reflected back in phase with the incident wave. The boundary condition must be free so that the incident and reflected wave are in phase. Otherwise, by the Newton's Third Law, the boundary would exert an equal, but opposite, force on the specimen and the phase of the resulting wave would differ $180°$ from the incident one.

2.3.2 The Resonance Phenomenon

Altogether, the equipment described in section 2.2 aims to excite the specimen to its resonance frequency at one of its longitudinal modes of vibration. Resonant frequency is defined as the oscillation of a certain system at its natural frequency. In other words, the phenomenon of *resonance* occurs when a dynamic load is periodically applied to a system, at a frequency equal or close enough to the natural frequency of the system where the dynamic load is acting. If this condition is met, the system will

oscillate in such a way that its displacement amplitudes are much higher than when other frequencies, named *non-resonant frequencies*, are applied (Halliday et al., 2013).

When a structure vibrates in resonance, it develops a certain shape associated with that particular frequency. To that specific deformed shape is given the designation *mode shape*. For every particular natural frequency, there is an associated mode shape, and both are closely related to the material properties and boundary conditions of the system. For instance, for the same geometry, if the Young's modulus is changed, then the natural frequency of the system will also change, while the mode shapes will remain unaffected. However, different mode shapes will appear if the boundary conditions are changed. It is also important to note that in an oscillating structure, all mode shapes are present. Nevertheless, when a certain resonant mode is being directly excited, the remaining mode shapes may have an influence on the directly excited mode. Their influence upon that mode depends on how close their resonance frequency is from the directly excited mode, and also on the shape of the modes. Costa et al. (2019) consider that the resonant mode of interest to be excited by the ultrasonic converter can become susceptible to the influence of other modes of vibration when these develop within a difference of 0.5 kHz from the mode of interest.

In ultrasonic fatigue tests the specimen is excited in resonance, meaning the waves propagating through the specimen are in constructive interference. Both Bathias and Paris (2005) and Willertz (1980) gave a detailed view of how a sound wave actually propagates through the specimen to create resonance. For the sake of simplicity, both authors resorted to the simplest specimen design: a straight bar of uniform diameter and length L (figure 2.4). Considering the situation where a sound wave is induced longitudinally at one of the ends of the described specimen, the wave will propagate through the specimen until reaching the other end. There, the wave will be reflected and will travel longitudinally but in the opposite direction, until it reaches the end where it has been induced into in the first place.

There are two types of waves: longitudinal and transverse (torsional) waves. Equations 2.7 and 2.8 (Bathias and Paris, 2005) give the velocity at which a longitudinal and torsional sound wave propagates through a material, respectively.

$$c = \sqrt{\frac{E(1-\nu)}{(1+\nu)(1-2\nu)\rho}} \tag{2.7}$$

$$c = \sqrt{\frac{G}{\rho}} \tag{2.8}$$

For slender shapes (cross section area $<<$ length), as in the case of specimens, it can be considered that mechanical waves do not propagate transversely to the longitudinal axis, implying the displacement in the transverse direction has a negligible effect. Thereby only longitudinal displacement is considered and the wave may be considered flat. Thus the mechanical wave energy may be considered to be uniformly distributed along each and every cross section, only changing with the axial distance to the wave source (Freitas et al., 2011). The Poisson effect may also be neglected and equation 2.7 transforms into equation 2.9. Since no transverse displacement is considered, the velocity of the transverse wave can be discarded, meaning equation 2.8 is no longer of interest for ultrasonic tests under axial conditions.

$$c = \sqrt{\frac{E}{\rho}} \tag{2.9}$$

Still regarding the straight bar of uniform diameter specimen, its resonance length L is, according to Bathias, inversely proportional to the frequency f, and directly proportional to the velocity at which the longitudinal wave propagates through the material $\sqrt{\frac{E}{\rho}}$, as shown by equation 2.10.

$$L = \frac{1}{2f}\sqrt{\frac{E}{\rho}} \tag{2.10}$$

Taking as an example a steel specimen of uniform section with an elasticity modulus, E, of $200GPa$ and a density, ρ, of $7800kg/m^3$, equation 2.10 allows to determine the resonance length, L, for specimens under different frequencies, f. Table 2.1 shows how small a specimen would have to be in order to be tested under frequencies as high as 92 kHz and 199 kHz. As conventional fatigue tests are typically performed at 100 Hz, the specimens are naturally longer than the ones used in ultrasonic fatigue tests. The resonance length of the specimen is thus the parameter setting an upper limit for the frequencies used to perform ultrasonic fatigue tests.

Table 2.1: Frequency dependency on the resonance length of a specimen. From Bathias and Paris (2005).

f [kHz]	L [mm]
20	127
92	27.5
199	13.2

A sound wave requires a certain amount of time to propagate twice the length of the specimen. That time is given by $2L/c$. The specimen is in resonance if the injected and reflected waves are in phase. In order for this to occur, the period of the induced mechanical wave must be equal to $2L/c$ (Willertz, 1980).

Figure 2.4 shows how the displacement and strain amplitude are distributed along the specimen in resonance. The curves indicate the following:

- the displacement amplitude, A, is maximal at both ends of the specimen;
- the displacement amplitude, A, is null in the specimen centre. This is called a *displacement node*;
- the strain amplitude, $\frac{dA}{dx}$, is maximal in the middle of the specimen,
- the strain amplitude, $\frac{dA}{dx}$, is null at both specimen ends. This is called a *stress node*;

The displacement node corresponds to the same cross section where strain, stress and strain rate are maximal.

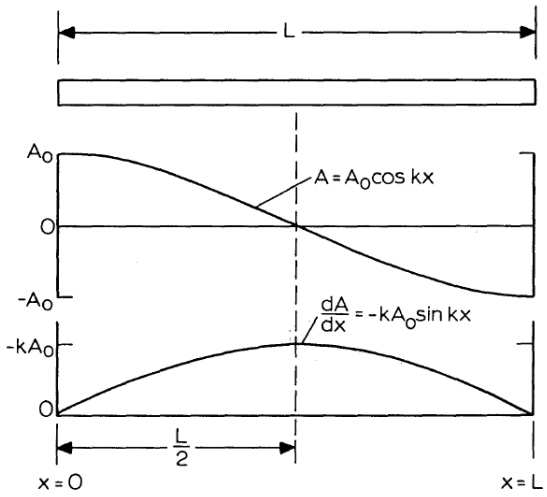

Figure 2.4: Straight bar of uniform diameter, and correspondent displacement and strain distribution along its length, L. Adapted from Willertz (1980).

2.4 Analytical Solution for the Variable Section Specimen

Despite the simplicity associated with machining and reproducing straight specimens, these are not typically used to perform ultrasonic fatigue tests. Instead, specimens with circular cross-sections with non-constant radius (*hourglass* geometry) are generally used. This specimen geometry was employed by Mayer (2006), Schuller et al. (2013), Furuya and Takeuchi (2014), Huang et al. (2016), Soares et al. (2018), among others.

This profile imposes the minimum cross section area at the centre of the specimen, where stress concentration will occur, reducing the need of applying excessively high loads to obtain the desired stress amplitudes in the middle section. The variable profile also prevents the specimen from absorbing and accumulating too much heat energy, hence reducing the need for powerful cooling equipment (Willertz, 1980). Bathias and Paris (2005) give an estimate for the the resonance length of a specimen, and its displacement and stress distribution along the longitudinal axis.

For an axisymmetric specimen, as in Figure 2.5, the profiles of the constant and variable cross section regions are defined as follows:

$$y(x) = R_2, \qquad \text{for } \; L_2 < |x| < L \tag{2.11}$$

$$y(x) = R_1 \cosh \alpha x, \qquad \text{for } \; |x| < L_2 \tag{2.12}$$

Where $L = L_1 + L_2$, and α is given by equation 2.13.

$$\alpha = \frac{1}{L_2} \operatorname{arcCosh}\left(\frac{R_2}{R_1}\right) \tag{2.13}$$

An estimate for the resonance length is given by equation 2.14.

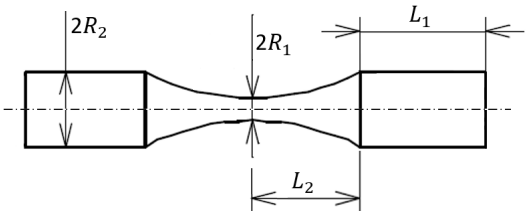

Figure 2.5: General representation of an hourglass specimen. Adapted from Bathias and Paris (2005) and Furuya (2008).

$$L_1 = \frac{1}{k}\arctan\left(\frac{1}{k}\left[\beta\coth(\beta L_2) - \alpha\tanh(\alpha L_2)\right]\right) \tag{2.14}$$

Where k is obtained from equation 2.15, in which c is given by equation 2.9, and ω by 2.16.

$$k = \sqrt{\frac{\omega}{c}} \tag{2.15}$$

$$\omega = 2\pi f \tag{2.16}$$

And also,

$$\beta = \sqrt{\alpha^2 - k^2} \tag{2.17}$$

Bathias and Paris (2005) made a comparison between a hyperbolic cosine profile, also known as catenary, and circumferential profile. It was concluded that up to a deviation of 2 mm from both sides of the middle section of the specimen, the catenary and circumferential profiles only differ by a maximum of approximately 0.9%. Since the circumferential profile is easier to machine, it may be used instead of the catenary one for the design of ultrasonic fatigue specimens.

The strain and stress equations for the variable section region of the specimen are respectively given by equations 2.18 and 2.19 presented in Bathias and Paris (2005).

$$\varepsilon(x) = A_0\varphi(L_1, L_2)\frac{\left[\beta\cosh(\beta x)\cosh(\alpha x) - \alpha\sinh(\beta x)\sinh(\alpha x)\right]}{\cosh^2(\alpha x)} \quad \text{for } |x| < L_2 \tag{2.18}$$

$$\sigma(x) = E_d A_0\varphi(L_1, L_2)\frac{\left[\beta\cosh(\beta x)\cosh(\alpha x) - \alpha\sinh(\beta x)\sinh(\alpha x)\right]}{\cosh^2(\alpha x)} \quad \text{for } |x| < L_2 \tag{2.19}$$

Where

$$\varphi(L_1, L_2) = \frac{\cos(kL_1)\cosh(\alpha L_2)}{\sinh(\beta L_2)}. \tag{2.20}$$

For the constant section region of the specimen, i.e., the cylindrical region, the corresponding strain and stress equations are, respectively, equations 2.21 and 2.22.

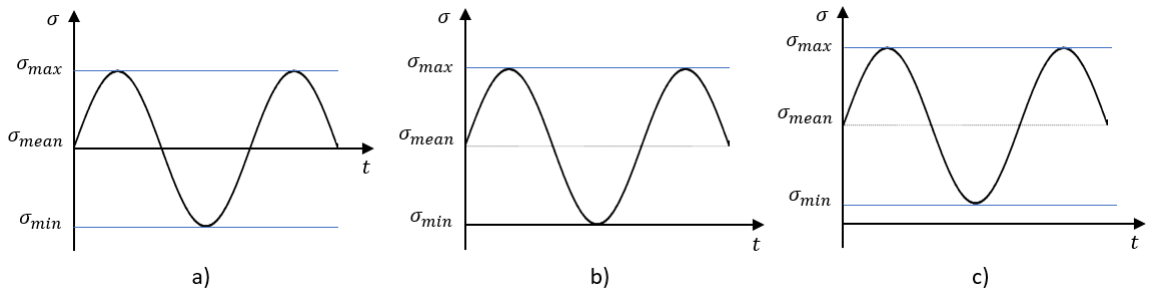

Figure 2.6: Stress fluctuations under different conditions. a) Fully reversed cyclic loading ($R = -1$). b) Repeated stress ($R = 0$). c) Fluctuating stress ($R > 0$).

$$\varepsilon(x) = kA_0 \sin(k(L - x)) \qquad \text{for} \quad L_2 < |x| < L \tag{2.21}$$

$$\sigma(x) = E_d kA_0 \sin(k(L - x)) \qquad \text{for} \quad L_2 < |x| < L \tag{2.22}$$

When designing the specimen geometry one must ensure the reduction of the diameter in the specimen central region is smooth enough to avoid reflection of the acoustic wave in this region (Mayer, 1999). Such phenomenon must occur exclusively at the free end of the specimen or else at the end of another device bolted to the second end of the specimen, as it will be explained further ahead in the document.

2.5 The Stress Ratio Concept

Considering the ultrasonic assembly of Figure 2.2, it is clear that one end of the specimen is in contact with the horn, whilst the other one is free. This setup is employed to perform ultrasonic fatigue tests in fully reversed condition, i.e., with no mean stresses, meaning the absolute values of both maximum and minimum stress amplitudes of the load are equal (Figure 2.6a).

The maximum and minimum stress amplitudes of a cyclic loading are correlated by the *stress ratio* (equation 2.23). Thereby, the setup of Figures 2.2 and 2.7 is associated with a *stress ratio* equal to -1.

$$R = \frac{\sigma_{min}}{\sigma_{max}} \tag{2.23}$$

A cyclic loading in fully reversed condition imposed on a body may be accompanied by a superimposed constant *mean stress* (Figure 2.6 b,c). In the context of ultrasonic fatigue testing machines, the superimposed *mean stress* may be obtained by applying a static load. The static load is often applied using a second horn that will be in contact with the lower free end of the specimen (Bathias, 2006). The *mean stress* of a cyclic loading is given by equation 2.24.

$$\sigma_{mean} = \frac{\sigma_{max} + \sigma_{min}}{2} \tag{2.24}$$

Reference	Stress Ratios	Induced Stress	Specimen
Sakai et al. (2006)	0; 0.5	axial	flat hourglass
Xue et al. (2007)	0.5	bending	flat disc
Kovacs et al. (2013)	0.1; 0.5; 0.7	axial	dog-bone
Schuller et al. (2013)	0.1; 0.5	axial	hourglass
Furuya and Takeuchi (2014)	0; 0.3	axial	hourglass
Huang et al. (2016)	0.1; 0.5; 0.7	axial	hourglass
Brugger et al. (2016)	0.1	biaxial bending	flat disc

Table 2.2: Commonly used *stress ratios* for mean stresses different from -1.

Table 2.2 displays the stress ratios employed by different authors, and the respective induced stress state and the geometry of the used specimens. Ultrasonic fatigue torsion tests are typically carried out under fully reversed cyclic torsion loading, i.e., with $R = -1$. Authors such as Xue and Bathias (2010), Schuller et al. (2013) and Nikitin et al. (2015) all performed torsion tests under this condition. Nevertheless, a mechanical setup to perform torsion fatigue tests with static superimposed loads is described in Mayer et al. (2015).

2.5.1 The Influence of the Stress Ratio on Fatigue Strength

In practical applications outside laboratories (e.g. compressor blades of aero engines), cyclic loads are often accompanied by mean stresses (Huang et al., 2016). Sakai et al. (2006) evaluated the fatigue strength for a high carbon chromium bearing steel under axial loading up to more than 10^9 cycles at 50 Hz and, reported results showing that for $-1 \leq R \leq 0.5$ the fatigue limit tends to decrease almost proportionally as the mean stress increases. Later, Huang et al. (2016) investigated the fatigue strength for a titanium alloy (TC-17) under static tensile loading in the VHCF regime at room temperature and at 20 kHz and also reported a decrease in fatigue strength due the presence of mean stresses.

Nevertheless, opposite results have also been reported: Mahfuz et al. (1995) investigated the effect of the stress ratio on the fatigue life on carbon-carbon composites at room temperature and under a frequency of 3 Hz. The stress ratios employed were 0, 0.2 and 0.4. The results showed that the higher the stress ratio, the higher the fatigue strength of the carbon-carbon composites. However, the logic behind the reported results may be considered to be questionable.

Hence, studying the materials behaviour when subjected to dynamic loads with a mean stress is of great relevance for engineers. The knowledge obtained from such studies helps engineers in the decision-making process of selecting adequate materials for various different practical applications.

2.6 The Evolution of Ultrasonic Fatigue Machines

The first ultrasonic fatigue testing machine was developed in the early 20^{th} century by Bertram Hopkinson. This machine had an electromagnetic resonance system of 116 Hz. Some years later, in 1925, Charles Frewen Jenkin used the same method as his predecessor to test wires of steel, copper and iron at 2.5 kHz. In 1929 Jenkin published again, this time obtaining 10 kHz using a pulsating air resonance system. It was in the middle of the century, in 1950, that Mason made great changes in this field of investigation. Mason used piezoelectric and magnetostrictive transducers capable of converting an electrical signal of 20 kHz into controlled mechanical vibrations of the same frequency, where sound waves were used to fracture materials (Bathias and Paris, 2005).

Meanwhile, much higher frequencies were tested, for instance 92 kHz and 199 kHz. Although these much higher frequencies may accelerate even further the process of fatigue testing in the gigacycle regime, they are not practical. The reason behind such statement is related to the specimen size. As it will be showed further ahead, the length of the fatigue specimen is inversely proportional to its frequency. As Willertz (1980) and Bathias and Paris (2005) stated, if the frequency is too high, then the specimen would have to be very small.

Along with tiny specimens, several problems arise, for instance the machining process becomes non practical due to the difficulties associated with tolerances. Moreover, necessary measurements to evaluate results become more difficult to perform. Also, problems associated with energy-dissipation arise, so the specimen would tend to accumulate more energy than supposed in the form of heat. Taking this into account, the most widely used frequency to perform ultrasonic fatigue tests is the value proposed by Mason, i.e., 20 kHz.

2.7 Ultrasonic Fatigue Testing Machines for Axial Conditions

Figure 2.7 represents the most simple ultrasonic fatigue testing condition, in which the piezoelectric transducer transmits a longitudinal cyclic motion onto the horn at a frequency matching the natural frequency of the system at one of its longitudinal modes, which is often 20 kHz by design. This type of fatigue tests may either be conducted under fully reversed condition or with a superimposed constant mean stress.

2.7.1 Longitudinal Ultrasonic Fatigue Testing under Fully Reversed Condition

Several studies have been conducted concerning uniaxial ultrasonic fatigue under fully reversed condition, such as Mayer (2006), Lage et al. (2012), Soares et al. (2018) and Lesperance et al. (2021). The ultrasonic fatigue tests are conducted in the elastic regime until the end of the experiment, i.e., until fatigue failure.

Figure 2.7 shows the stress and displacement distribution curves along a resonant system consisting of one converter, one horn and one axisymmetric specimen. This testing condition is characterised by

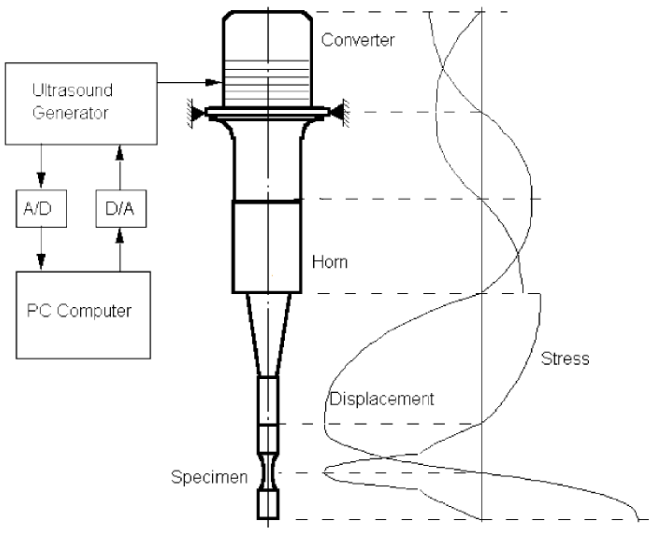

Figure 2.7: Stress and displacement distribution along the ultrasonic system under $R = -1$. Adapted from Bathias and Paris (2005).

the presence of (i) four stress nodes, and consequently four displacement antinodes, and (ii) three displacement nodes and consequently four stress antinodes (Bathias and Paris, 2005).

At the connections between elements the displacement is the highest and the stress is minimum (stress nodes). Stress nodes at the connections ensure their stability throughout the experiment. If there were no stress nodes at the connections, consequences such as the horn or the specimen unscrewing themselves during the fatigue tests could occur. Other possible consequence is that it might alter the dynamic behaviour of the resonant system and compromise the test results.

At the centre of the specimen the stress is maximum and there is a displacement node. As the fatigue tests are conducted in the elastic regime (governed by the Hooke's Law), then the strain is maximum at this location as well. This is the fatigue testing region.

2.7.2 Longitudinal Ultrasonic Fatigue Testing with a Superimposed Constant Mean Stress

As stated in subsection 2.5, a constant mean stress is applied my means of an applied static load. A second horn is then added to the system (Figure 2.8a), being its natural frequency the same as the other components at the desired longitudinal mode. The static load is applied by the horns connected to the specimen through mounting devices, which must therefore be placed at displacement nodes, as represented in Figure 2.8b. Applying the static load at displacement nodes ensures damping of the working frequency does not occur (Mayer, 1999). Different values for the constant mean stress are then obtained by adjusting the static load intensity. The ultrasonic system of Figures 2.8a and 2.8b exhibits a set of stress and displacement nodes and antinodes as follows:

- three displacement nodes (DN): one at the centre of the specimen, and one at the sections where the static load is applied;

- two displacement antinodes (DA): one at each horn-specimen connection;
- two stress nodes (SN): one at each horn-specimen connection;
- one stress antinode (SA) located at the centre of the specimen.

Huang et al. (2016) studied the effect of mean stresses on the behaviour of a compressor blade titanium alloy in the gigacyle regime by installing a piezoelectric fatigue system on the static electric tension machine (SHIMADZU-20kN) in order to apply static loads.

Also, Furuya and Takeuchi (2014) evaluated the Ti-6Al-4V alloy fatigue properties under tensile mean stress in the VHCF regime. The experiments were conducted under a superimposed axial loading in the SHIMADZU USF2000 machine, which is equipped with a load frame for this purpose. The ultrasonic set is composed of two high rigidity boosters and two horns, one of each at both specimen ends. Similarly, Bathias (2006) also conducted experiments in an ultrasonic fatigue machine with a superimposed static load by means of a second horn.

Mayer et al. (2013) describes a testing equipment developed at the Institute of Physics and Materials Science of the University of Natural Resources and Life Sciences (BOKU) in Vienna, assembled into a servo hydraulic machine to perform experiments under constant and variable amplitude loading conditions. Two mounting devices were used to apply the superimposed load. The author only resorts to one horn, and the displacement amplitude constraint at the ends of the specimen are assured by rods of half or full wavelength, implying both ends of the rods are displacement nodes, meaning the load is applied without damping the resonance system.

Finally, considerations on the ultrasonic set design must be taken into account to avoid bending stresses from compromising the tests results. To assure symmetry of the ultrasonic set, both horns must present identical geometries. Moreover, undesirable bending stresses may occur due to the presence of static loads, so perfect alignment of the load train is required to avoid such situation. Unwanted bending stresses may also be avoided by requiring low tolerances regarding the symmetry of the load train.

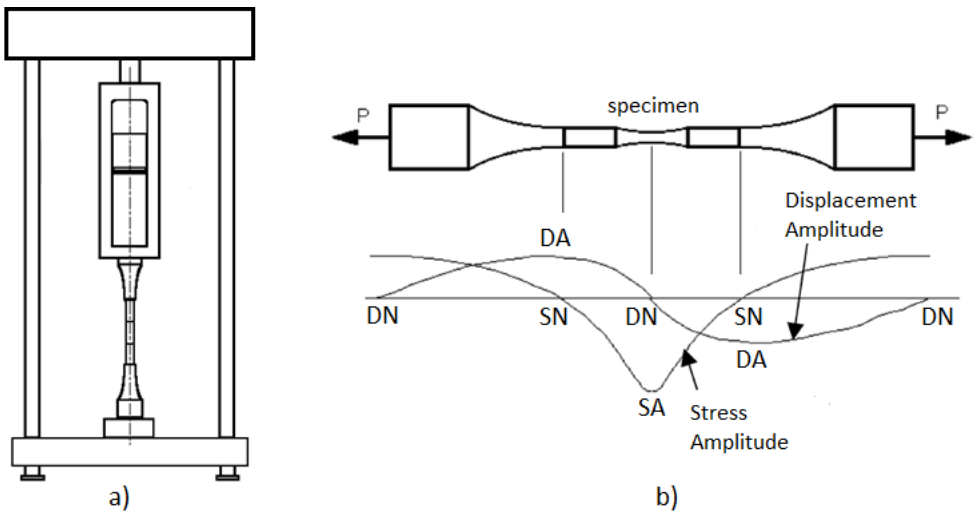

Figure 2.8: a) System layout for conducting fatigue tests under $R \neq -1$. b) Displacement and stress distribution along the ultrasonic system with an applied static load, P, and respective displacement and stress nodes and antinodes. Pictures adapted from Bathias and Paris (2005).

2.7.3 Ultrasonic Horn Design

Ultrasonic horns are devices whose function consists on magnifying the displacement amplitude of an mechanical wave that travels through them. Horns are solid bodies that have two stress free surfaces, being those surfaces both its ends (Eisner, 1963). In order to magnify the displacement amplitude, both surfaces must have considerably different cross section areas. One must take into consideration the following information:

- If $S_i > S_o$, then the output displacement amplitude decreases;
- If $S_i = S_o$, then the output displacement amplitude does not change;
- If $S_i < S_o$, then the output displacement amplitude increases.

Where S_i and S_o are the horn input and output surface areas, respectively. Given the information above, it is straightforward that the output surface area must be smaller than the input one. The changes in both areas must be accompanied by length adjustments in order to preserve resonance (Willertz, 1980).

The ratio of the maximum to the minimum cross section areas is given by equation 2.25. Since all cross sections are circles of area $S = \frac{\pi d^2}{4}$, then it is possible to relate the areas ratio, R_A, with the diameter ratio, R_D.

$$R_A = \frac{S_i}{S_o} = \left(\frac{d_i}{d_o}\right)^2 = R_D^2 \tag{2.25}$$

Willertz (1980) summarised the different ultrasonic horn geometry profiles. Figure 2.9 shows the different horn profiles. The simplest profile to produce is the *stepped* one, and has the advantage of being capable of magnifying input displacement amplitudes into almost any value. Nonetheless, it is prone to develop stress concentrations in the section where the diameter abruptly decreases, possibly leading to crack formation. Consequently, this type of profile may fail prematurely due to fatigue. Besides, the steep change of the cross section area disturbs the propagation of the mechanical waves along the ultrasonic horn due to the reflection phenomenon. To avoid this phenomenon, the radius of the transition must be greater diameter of the horn. Thus, smooth transitions of the cross sections diameter are preferable to guarantee an efficient propagation of the sound waves through the ultrasonic set (Mayer, 1999).

Figure 2.9 shows that the *conical*, *exponential*, *catenoidal* and *Fourier* profiles have smaller and more uniformly distributed amplitude stresses, which makes them less susceptible to fatigue failure. The author also stated that the *Fourier* profile, proposed by Eisner (1963), might be considered the best horn geometry, since it is capable of producing the highest displacement amplification with the greatest strength and stiffness. In fact, for a amplification factor of 100, Edward Eisner's *Fourier* design is only 2.6 times less stiff in bending than the *stepped* design, being simultaneously 130 times stiffer than the *exponential* one. Hence the *Fourier* design is a good compromise between the *stepped* and *exponential* designs, which at the time of publication of Eisner's scientific article, were the most popular profiles for longitudinal vibration.

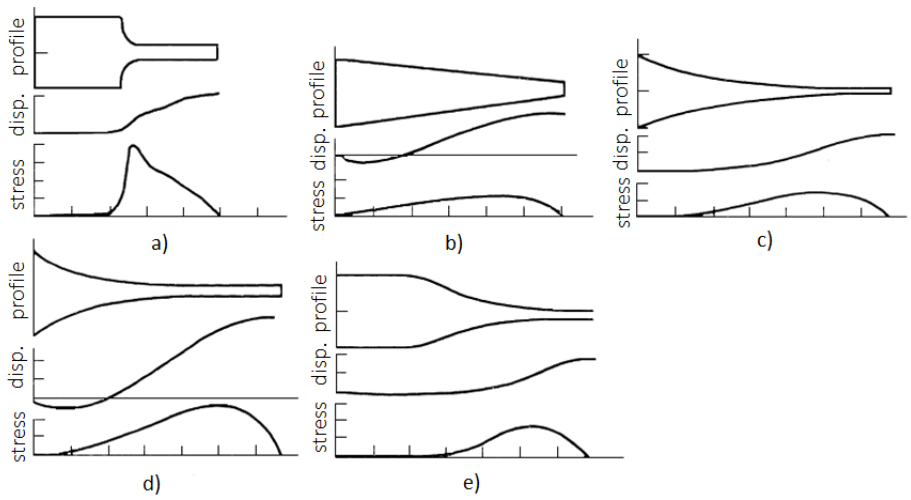

Figure 2.9: Different profiles of amplifying horns and correspondent displacement and stress distribution. a) Stepped. b) Conical. c) Exponential. d) Catenoidal. e) Fourier. Adapted from Willertz (1980).

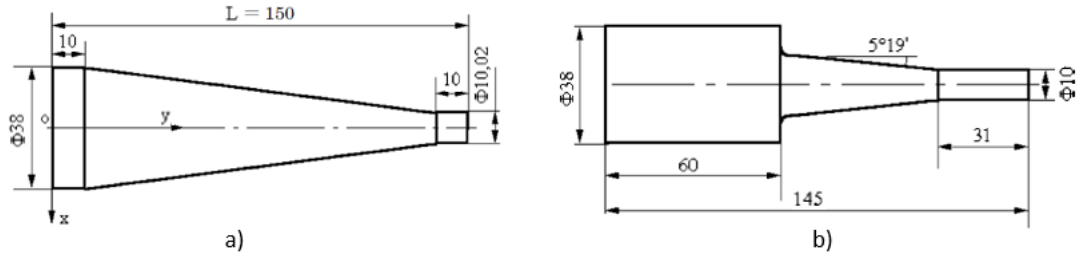

Figure 2.10: Amplifying horns. a) Conical profile. b) *Fourier* profile. Dimensions in mm. Adapted from Bathias and Paris (2005).

The amplification factor is the ratio of the output displacement amplitude, V_1, to the input displacement amplitude, V_2, as stated on equation 2.26 (Bathias and Paris, 2005). The value of the amplification factor may vary from 1 to 40 (Mayer, 1999). Also, multiple horns may be attached to each other in order to achieve multiple increments of the displacement amplitude.

$$F_{amp} = \left| \frac{V_1}{V_2} \right| \tag{2.26}$$

Bathias and Paris (2005) compared two different ultrasonic horn designs: one based on the *conical* profile (Figure 2.10a) and the other one based on the *Fourier* profile (Figure 2.10b). The experiments were carried out in three different environments: at room temperature, in liquid nitrogen and in liquid helium. The results have shown a preference for the *Fourier* inspired profile in both cryogenic environments, since it was capable of producing higher stresses and amplification factors. Both horns present a cylindrical body on both ends to increase stiffness without affecting the amplification factor. The introduction of these bodies may help repelling parasite modes that might affect the working mode (Freitas et al., 2011).

2.8 Ultrasonic Fatigue Testing Machines for Non-Axial Conditions

Ultrasonic fatigue testing machines for torsion and bending have been developed in some laboratories, such as Mayer et al. (2015), Mayer (2016), Marines-Garcia et al. (2007), Bathias and Paris (2005) and Xue et al. (2007). Section 2.2 enumerates the basic components of an ultrasonic fatigue testing machine. Such resonant components are common to all so far designed ultrasonic fatigue systems, apart from the number of horns and boosters used. That number is dependent on the design of each particular system, and on each particular test condition as well.

The principle of applying the static loading onto a displacement node in the booster is consistently applied to all ultrasonic fatigue tests under superimposed mean stresses.

In the present section, bending and torsion loading conditions will be briefly described, as they will emphasise how to apply the described ultrasonic concepts towards the desired fatigue stress state.

2.8.1 Bending Fatigue Testing Machines

A three-point bending ultrasonic fatigue testing machine was developed in Bathias's laboratory, in France. The system described in Bathias and Paris (2005) and (Xue et al., 2007), requires one horn and one booster to operate. As opposed to ultrasonic axial fatigue systems, ultrasonic three-point bending fatigue systems impose transverse vibration onto the specimen. Thus, the specimen, must be designed so that its intrinsic frequency of transverse vibration matches the working frequency of the system (Xue et al., 2007). The specimen has a rectangular geometry, and the horn delivers the sinusoidal load at the centre of the specimen. The upper face of the specimen is thus under compression, whereas the lower face is under tensile stresses. Ultrasonic fatigue tests under bending conditions can be performed by introducing the ultrasonic system into a tensile testing machine, as represented in Figure 2.11a (Bathias, 2006). The place where the mounting device is coupled to the ultrasonic system must be in accordance with the mechanism described in section 2.7.2, i.e., at a displacement node.

More recently, a testing device to conduct fatigue tests under ultrasonic biaxial loading was developed by Brugger et al. (2016). The specimen is a smooth flat disc, and is placed on a frame with a torus ring. The contact area between the lower face and the frame is therefore a circle. By means of an axial ultrasonic horn with a hemispherical indenter, a sinusoidal load is applied to the upper face of the specimen, exactly in its centre, imposing bending stresses onto the disc. In ultrasonic biaxial bending, the horn imposes longitudinal vibration onto the specimen, which must then be designed so that its natural frequency for axial displacements matches the working frequency of the system. The crack initiation site is at the centre of the lower face, where the biaxial stress state is maximal. Tests with superimposed mean stresses are possible by coupling this device to an electromechanical testing machine by means of three columns and two hollowed discs located at a displacement node, as represented in Figure 2.11b.

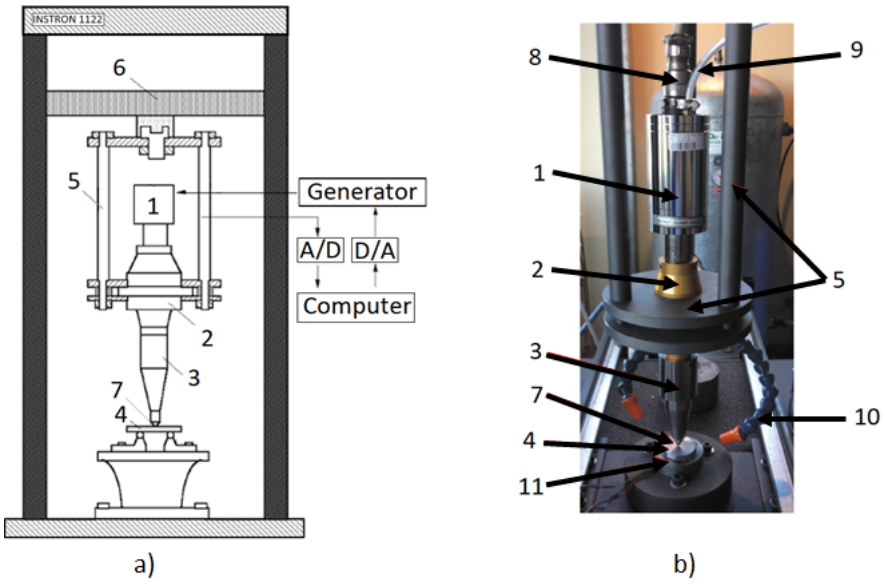

Figure 2.11: Ultrasonic fatigue testing devices for bending stresses. a) Three-point bending. Adapted from Bathias and Paris (2005). b) Biaxial bending. Adapted from Brugger et al. (2016).
Legend: (1) piezoelectric converter, (2) booster; (3) horn; (4) specimen; (5) mounting device; (6) crosshead; (7) hemispherical indenter; (8) 20 kHz electric signal generator; (9) and (10) converter and specimen air cooling systems; (11) frame ring (not visible).

2.8.2 Torsion Fatigue Testing Machines

Ultrasonic fatigue tests under torsion require an ultrasonic torsion converter, which imposes torsion waves onto the vibrating parts. All vibrating parts must be carefully designed to resonate at the frequency of the torsion converter. Although the centre section of both torsion and tension-compression specimens have the same shape, to achieve resonance in torsion fatigue testing, the size of the vibrating components must be smaller compared to other types of ultrasonic fatigue testing. This is explained by equation 2.27, which implies the shear modulus is smaller than the Young's modulus (Bathias and Paris, 2005).

$$E = 2G(1 + \nu) \tag{2.27}$$

Mayer (2016) describes an ultrasonic equipment to perform fatigue tests under cyclic torsion under the fully reversed condition. The mechanical system is composed by a converter, a mounting part, an ultrasonic torsion horn to amplify the rotational oscillations, and a specimen with a free end.

Also, Mayer et al. (2015) presented for the first time an ultrasonic fatigue setup capable of performing experiments under torsion with superimposed mean stresses. In this setup, both ends of the specimen are coupled to ultrasonic horns, and twist in opposite directions. The horns will have a vibration node in a determined section, similar to any other described horn. A torque disc is integrated into the lower mounting device of the mechanical system in order to introduce a static torque by means of weights.

Nonetheless, some years earlier Marines-Garcia et al. (2007) had presented a different approach using an axial converter instead of a torsional one. This mechanical setup consists on two distinct sections: A and B. The axial ultrasonic horn (Horn 1) integrating section A is directly connected to the

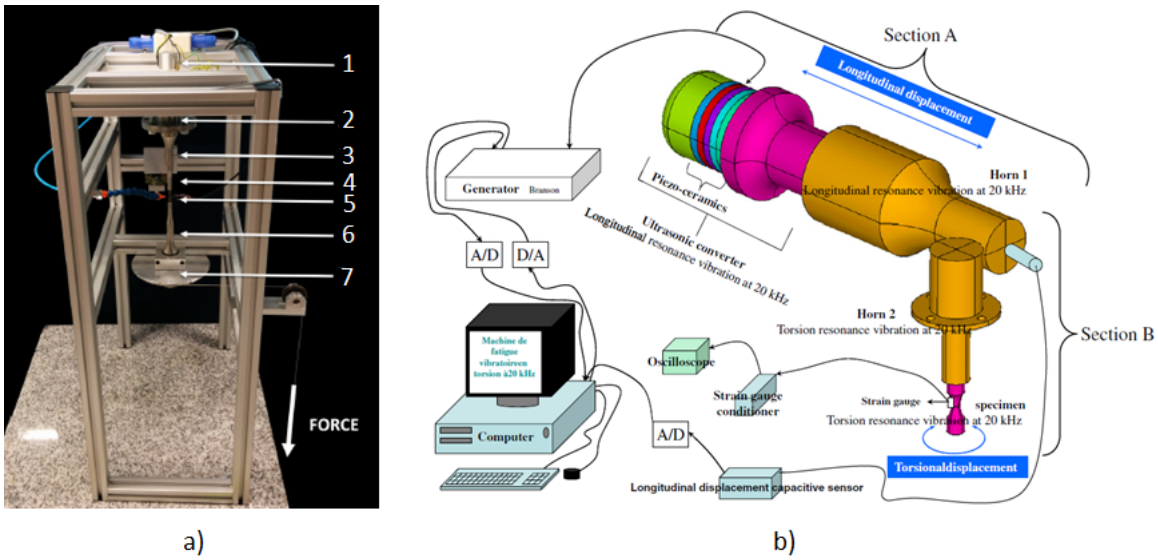

a) b)

Figure 2.12: Mechanical devices for conducting ultrasonic fatigue tests under torsional stresses. a) With a superimposed static torsion load. Adapted from Mayer et al. (2015). b) Resorting to an axial converter. Adapted from Marines-Garcia et al. (2007).
Legend: (1) ultrasonic converter, (2) upper mounting part, (3) and (6) ultrasonic horns, (4) vibration gauge, (5) specimen, (7) rotating disc and lower mounting part.

axial transducer, which induces longitudinal vibrations onto Horn 1. To convert the axial displacement obtained in section A into torsional vibration, section B, consisting on a torsional horn (Horn 2) and torsional specimen, was added to the system by means of a pin. Thus, while section A vibrates at its axial mode, section B vibrates at its pure torsional mode, both at the same frequency. In the words of Marines-Garcia et al. (2007), this solution proves a "*loading train designed to vibrate on its axial mode can be the source of power over another body which as been calculated to vibrate on torsion mode*". Hence, if one is to perform torsional ultrasonic fatigue tests and has at disposal a tension-compression fatigue testing device, there is no need to purchase a new machine specifically for this purpose.

Chapter 3

Machine Structure and Materials

One main goal of this dissertation is the design and manufacture of a support structure to superimpose a static load onto an ultrasonic system, via an electromechanical testing machine. This chapter provides the information on the developed structure for performing the ultrasonic fatigue tests under axial condition with a superimposed static load and the properties of the materials of the elements of the structure, ultrasonic horns and specimens.

3.1 Machine Structural Elements

The structure design had three main constraints: (i) applying a static load using the electromechanical machine onto an ultrasonic system without influencing its resonance state , (ii) designing the structure and the ultrasonic system to fit within the limits of the available workspace (1000 mm) of the electromechanical testing machine, and (iii) the structure must be relatively easy to assemble and disassemble. For this chapter, it is only critical to refer that both horns were designed with an outer ring working as a support device, as will be exposed in Chapter 4.

The developed structure was based on the structure from Figure 2.11. The structure developed in the scope of the present work consists of two parts which may hereby be referred as *cages* (composed of three discs each and three rods). The upper *cage* will move with the electromechanical machine crosshead, while the lower *cage* is fixed and supports the second ultrasonic horn (Figure 3.1a).

Both upper and lower *cages* are coupled to the electromechanical machine crosshead and bottom of the electromechanical testing machine, respectively, by means of one disc (respectively upper and lower disc) and one link element. In simple words, the structural apparatus regarded as *mounting device* in Figure 2.11 is also implemented at the bottom of the electromechanical machine. Finally, two guide rods were designed to primarily establish the required alignment of the *cages* to avoid bending stresses that may compromise the axial ultrasonic fatigue tests. The design of these guide elements includes changes in their geometry, allowing for the electromechanical machine crosshead and upper *cage* to ascend and descend after the entire structure is assembled into the electromechanical testing machine, hence facilitating the assembling and disassembling procedures. These features also add versatility to

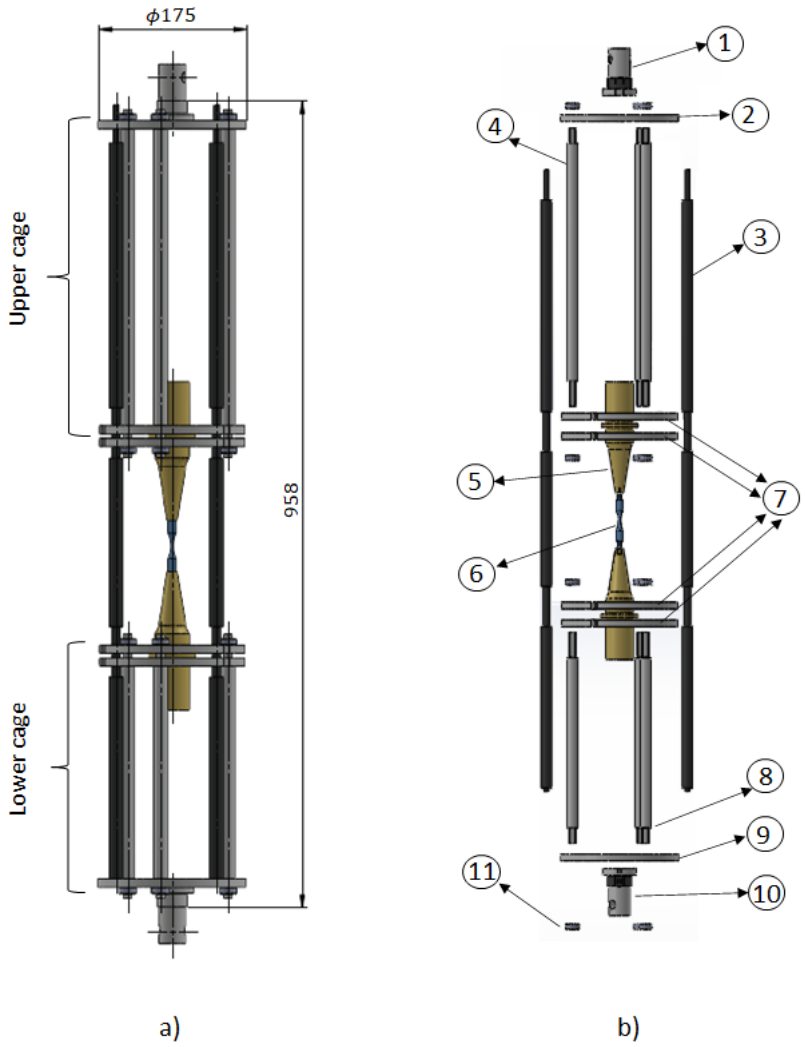

Figure 3.1: a) Principal dimensions of the developed structure and cage identification. Dimensions im mm. b) Exploded view of the structure from the front view. **Legend**: (1) link element, (2) upper disc, (3) guide rod, (4) upper rod, (5) horn, (6) specimen, (7) teared discs, (8) lower rod, (9) lower disc, (10) threads.

the structure, in the sense that allows testing specimens of different lengths. Figure 3.1b illustrates the exploded view of the assembly to better clarify how the different mechanical elements interlock.

Despite only having two guide rods, three radial tears (long rounded through holes) were machined in the discs (number 7 of Figure 3.1b), providing not only a simple way of assembling and disassembling the structure, but also the possibility of adapting the location of these guide elements whenever necessary. All six discs were machined and drilled together to ensure uniformity of the outer circular surface (Figure 3.2a), and optimal alignment of all equally spaced holes and tears (Figure 3.2b). As previously mentioned, a good alignment of these elements will facilitate the structure assembly and will prevent bending, which may compromise the ultrasonic set and the tension-compression fatigue test.

The link elements (Figure 3.2c) were designed to follow the electromechanical connection configuration, and to allow for an independent $360°$ continuous rotation of the upper and lower discs that feature a spotface on one of the surfaces (Figure 3.3a). The lower and upper discs are fixed to their respective link elements by means of a M12 thread, a compression ring and a pin, as in Figure 3.3b. The combination

of these features facilitate the assembling procedure and works as an adjustment mechanism that contributes to the mitigation of problems associated with the misalignment of the *cages* that could impact the specimen. Finally, Figure 3.4 shows the horns-teared discs connection configuration. The ultrasonic horns are designed with an outer ring that will fit between two teared discs in a sandwich arrangement.

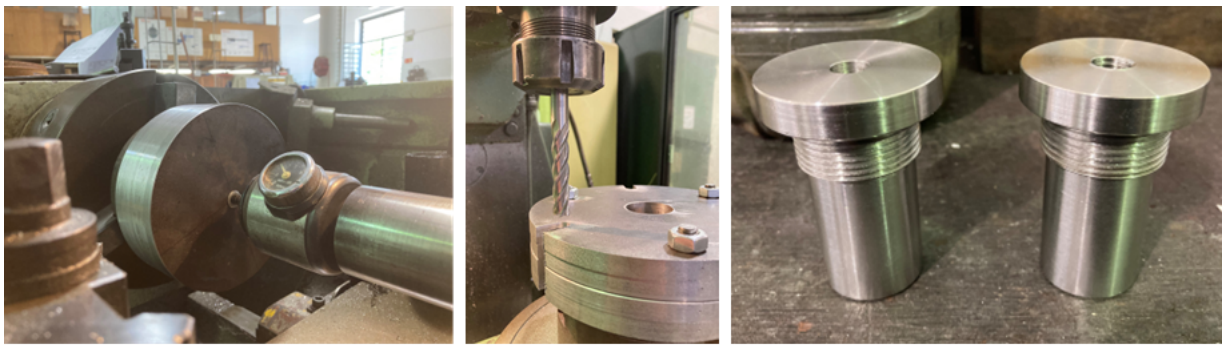

Figure 3.2: Machining procedures. a) Machining of the discs in the lathe machine. b) Drilling procedure of the tears. c) Link elements.

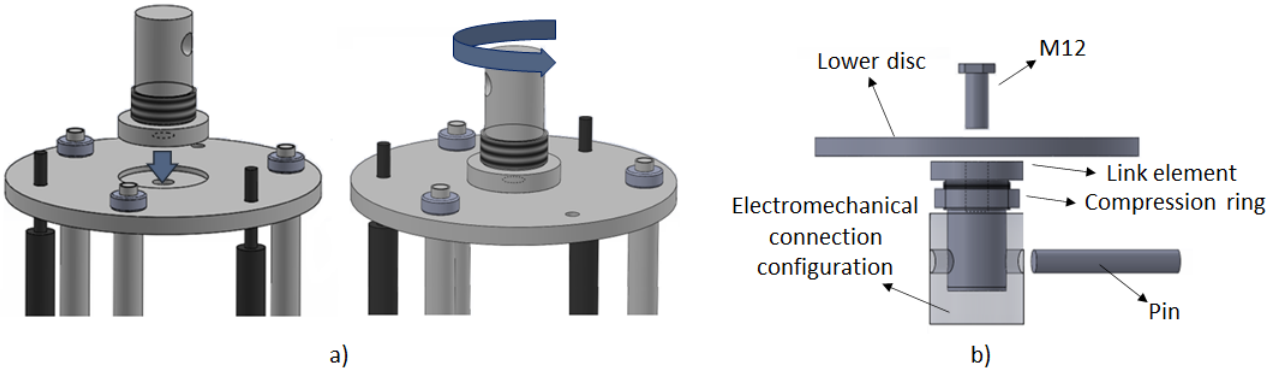

Figure 3.3: Detail on the connection upper/lower discs-link elements. a) Rotation mechanism. b) Exploded view of the complete connection configuration.

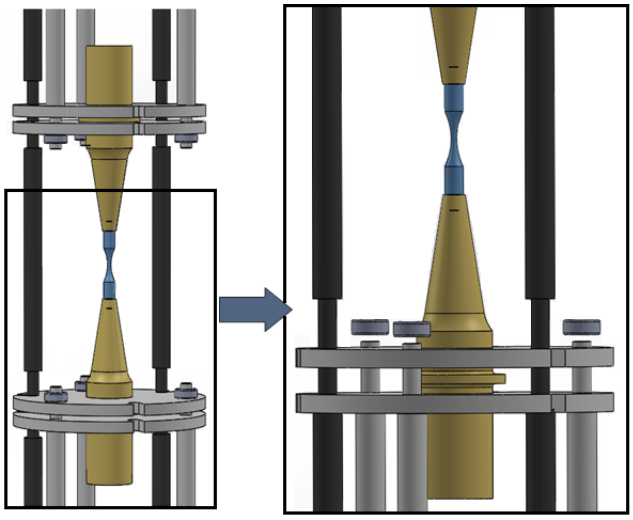

Figure 3.4: Detail on the connection horn-teared discs.

3.2 Assembling Procedure

The teared discs are numbered from 1 to 4. This identification allows selecting and assembling the discs sequentially to guarantee perfect alignment. The numbered surfaces must be facing upwards and the numbers should be aligned. During the assembling stage all threads must be tight enough to prevent the structure from disassembling, but loose enough to allow for adjustments so that the specimen can be introduced into the load train without being subjected to prejudicial loads. A load cell of at least 10 kN has to be installed in the electromechanical machine before assembling the structure. Two people are strongly recommended to perform the following steps.

1. Assemble the piezoelectric transducer to the superior horn together with teared disc (no 4);
2. Assemble the upper *cage* **outside** of the electromechanical machine by adding the three upper rods and teared disc (no 3);
3. Assemble both lower and upper link elements to the electromechanical machine by means of the respective pins and compression rings;
4. Couple the upper *cage* to the upperr link element by means of a M12 thread and rise the electromechanical machine crosshead;
5. Place the lower disc (of the lower *cage*) on top of the bottom link element and screw the second M12 thread;
6. Add the three inferior rods to the inferior disc and disc number 1;
7. Place the lower ultrasonic horn on teared disc (no 1);
8. Place teared disc (no 2) on top of the lower ultrasonic horn;
9. Add the guide rods to the structure by first inserting the upper part of the rods in the appropriate holes of the upper disc, then carefully slide the rods into the teared discs and finally fit the lower end of the guide rods in the respective holes of the lower disc;
10. Screw the specimen to the lower horn and move the electromechanical machine crosshead down slowly and carefully until the tip of the upper horn is close to the upper end of the specimen, ensuring the specimen thread is aligned with the threaded hole on the tip of the upper horn;
11. Move the electromechanical machine crosshead slowly and screw the specimen by rotating the superior horn. It is of great importance to control the load during this procedure by using the Bluehill Universal software;
12. Tighten all threads completely to mitigate some existent looseness;
13. Carefully remove the guide rods (see section 5.4 for further clarification).

3.3 Disassembling Procedure

Similarly to the assembling procedure, the structure must be disassembled by two people by following consecutively the steps below.

1. Loosen the threads of the lower *cage*, except for the M12 that couples the *cage* to the bottom link element;
2. To remove the specimen consider the following options:
    - if the specimen did not fracture, then follow instruction 11 from the *Assembling Procedure* but move the electromechanical machine crosshead upwards with the guide rods still in place
    - if the fracture is total, remove the guide rods and move the electromechanical machine crosshead upwards to ensure adequate space for disassembling the lower *cage*, and then unscrew both parts of the fractured specimen;
3. Disassemble the inferior *cage* by sequentially removing disc 2, the horn, disc 1, the rods, the inferior disc and link element;
4. Move the electromechanical machine crosshead downwards and carefully remove the entire upper *cage* by carefully unscrewing the M12 thread that couples the *cage* to the electromechanical testing machine;
5. Disassemble the elements of the upper *cage* **outside** of the machine;
6. Disassemble the upper link element.

3.4 Material Properties

The material used for manufacturing the mechanical elements of the structure, namely all rods and discs, was a structural carbon steel of grade S275JR. The elements of this steel were coated to prevent oxidation. The ultrasonic horns were manufactured in a CK45 steel, and concerning the specimens two materials were tested: a generic steel and a 7075 aluminium alloy. However, as will be discussed in Chapter 5, although specimens of both materials were evaluated under the finite element method (FEM), the experimental tests were only conducted for the aluminium alloy specimen.

Tables 3.1 and 3.2 provide the chemical composition of S275JR and Al7075 respectively. Table 3.3 provides the mechanical properties of all materials employed in the development of the present work, including the structural elements and ultrasonic set components (horns and specimens).

Table 3.1: Chemical composition of the S275JR steel.

C[%]	**Mn**[%]	**Si**[%]	**S**[%]	**P**[%]	**Ti**[%]	**Cu**[%]	**Al**[%]	**V**[%]	**Nb**[%]	**Cr**[%]	**Ni**[%]	**Mo**[%]	**N**[%]
0.160	0.370	0.010	0.010	0.013	0.001	0.030	0.030	0.002	0.002	0.050	0.020	0.003	0.004

Table 3.2: Chemical composition of the 7075 aluminium alloy.

—	**Si**[%]	**Fe**[%]	**Cu**[%]	**Mn**[%]	**Mg**[%]	**Cr**[%]	**Zn**[%]	**Ti**[%]	
Min	—		1.2	—	2.1	0.18	5.1	—	**Zr** +**Ti**
Max	0.40	0.50	2.0	0.30	2.9	0.28	6.1	0.20	0.25

Table 3.3: Mechanical properties of the materials employed in the structural elements, horns and specimens.

Material	E $[GPa]$	ρ $[kg/m^3]$	ν	σ_{yield} [MPa]	σ_{rup} [MPa]
S275JR	—-	—-	—-	275	419
Steel	200	7800	0.30	—-	—-
Al7075	72	2800	0.33	600	666
Ck45	210	7800	0.29	—-	—-

Chapter 4

Finite Element Method and Numerical Results

This chapter details the procedure employed to obtain the geometry of the ultrasonic horns and two different specimens. Each component of the resonant system is numerically evaluated and the correspondent results are presented. The overall mechanical system is also studied resorting to finite element analysis (FEA) under different loading conditions.

4.1 Ultrasonic Horn Modelling Procedure

The modelling procedure of the horns consisted on two distinct stages. The first design stage consisted on obtaining an adequate horn geometry, resonating at the working frequency of the machine, with a displacement node at a suitable location for installing the mounting device. Ensuring that the resonance frequencies of the undesirable mode shapes were sufficiently distanced from the working frequency of the machine was also included in the first modelling phase. The second design stage was dedicated to tuning the resonance frequency and evaluating the stability of the displacement node through a mesh convergence analysis.

The ultrasonic horns geometry was obtained through an iterative process based on structural finite-element analyses computed on Siemens Software NX™. The natural frequencies and mode shapes for each geometry iteration of the ultrasonic horn were determined resorting to a free boundary condition modal analysis (SOL 103 Real Eigenvalues), using the *Lanczos* method and the *Nastran* solver. The results of the analysis characterise its mechanical behaviour when subjected to dynamic loading. All modal analyses performed considered damping to be negligible, meaning the variation of the natural frequencies due to damping is inappreciable.

4.1.1 Horn Mesh Generation

To optimise the process for attaining the final geometry of the ultrasonic horns, two types of elements were used, each at different phases of the design procedure. Linear elements hold two nodes per edge, whereas the quadratic ones hold three nodes per edge. The presence of an additional node at each edge allows for the definition of the deformation with quadratic functions, leading to more accurate results. Since clear identification of undesirable mode shapes near the working frequency of the ultrasonic machine is required, it was decided to resort to quadratic tetrahedral and hexahedral elements of 10 and 20 nodes, respectively.

The iterative process for obtaining the final geometry of the horns was conducted with a mesh composed of 3 sided solid 3D elements of 10 nodes, i.e., CTETRA(10) elements (Figure 4.1), due to implementation advantages. The element size was set to 5 mm throughout the process, which was the size recommended by the software, resulting in relatively short computational times.

In the second stage of the modelling procedure, aiming the creation of a structured grid composed of a more uniform and symmetrical mesh around the axis of symmetry of the horn, the structural analysis was repeated with a mesh of hexahedral elements of 20 nodes - CHEXA (20) - generated with the *3D Swept Mesh* command (Figure 4.2). This type of mesh provides more accurate results and symmetrical mesh pattern compared with the tetrahedral one, yet requires significant geometry decomposition into appropriate simple geometries and removal of features, such as *fillets* and *chamfers*, which can be challenging and time consuming. By applying this type of element exclusively on the last stage of the iteration process, one may save a significant amount of time.

To create an hexahedral mesh, the final horn geometry was decomposed into simpler hexahedral meshable geometries, as represented in Figure 4.3, using the *Split Body* command. To guarantee mesh symmetry in all cross sections along the horn, radial partitions were implemented. Radial partitions also ensure the existence of nodes distributed along the axial symmetry axis, which are useful to obtain the displacement and stress results along that axis. This method creates several independent parts, all behaving as one rigid body. In that sense, the *Mesh Mating Condition* was implemented, ensuring connectivity between the meshes of the individual parts at the specified interfaces, ultimately merging the nodes of every solid.

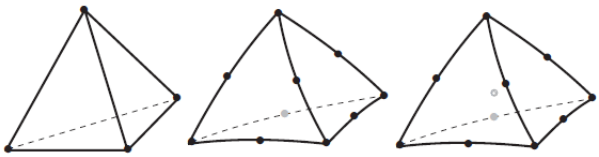

Figure 4.1: 4-, 10- and 11-node tetrahedral elements (CTETRA). Adapted from Nastran (2010).

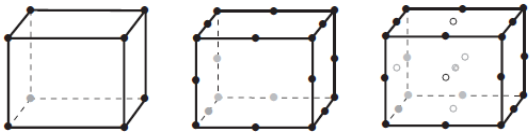

Figure 4.2: 8-, 20- and 27-node brick elements (CHEXA). Adapted from Nastran (2010).

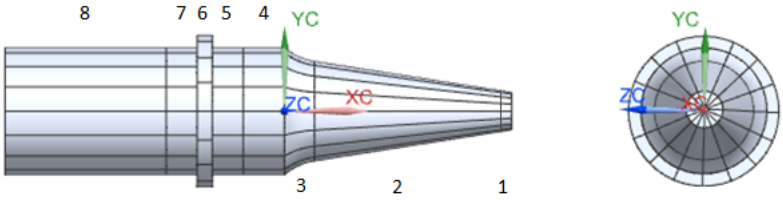

Figure 4.3: Ultrasonic horn views and respective necessary split bodies to the CHEXA(20) mesh generation.

Besides the essential transverse partitions needed to employ the hexahedral mesh, for instance partition 2-3, 3-4, 5-6 and 6-7, supplementary partitions 1-2, 4-5 and 7-8 were also included. Partition 1-2 is of particular relevance for providing a relatively small volume at the tip of the horn, where the mesh may be refined independently from the subsequent part. A convergence analysis of the hexahedral mesh was performed on the final geometry. As the size of the elements decreased, the need of increasing the number of radial partitions emerged.

4.1.2 Stop Criteria

The defined stop criteria of the iterative process consists on the observation of (i) the resonance frequency at the desired longitudinal mode at approximately 19800 Hz, and (ii) the displacement node at an adequate location in the cylindrical region.

Although ultrasonic fatigue tests are typically conducted at 20 kHz, the decision of aiming 19800 Hz is related to the fact that the properties of the material of the horns might be slightly different from the ones defined in the structural analysis, eventually resulting in the horns not resonating at the intended frequency. This variance in the properties of the material must be considered, thus the geometry of the ultrasonic horn was developed to provide a location where geometry adjustments could be performed to mitigate its effects (Freitas et al., 2011).

The CK45 steel has been used in ultrasonic applications in *Laboratório de Ensaios Mecânicos e de Materiais* of Instituto Superior Técnico, and by experience it is known that the actual resonance frequency of CK45 steel parts is expected to be from 100 Hz up to 200 Hz lower than the design natural frequency. Consequently, the horns were deliberately designed a few millimetres longer in the L_2 region (see Figure 4.4) to resonate at a lower frequency, guaranteeing the possibility of adjusting frequency post manufacture by removing length.

Finally, concerning the location of the displacement node, it was stipulated that a constant section region of at least 20 mm long is needed at both sides of the displacement node, where the ring (partition 6 of Figure 4.3) is to be implemented. The lower limit of 20 mm considers (i) the ring thickness to be implemented, and (ii) the thickness of the mounting device discs.

4.1.3 Horn Geometry

Along with the dimensions provided on Table 4.1, Figure 4.4 establishes the initial geometry of the iterative process for obtaining the final horn geometry. The starting geometry consisted on a rough

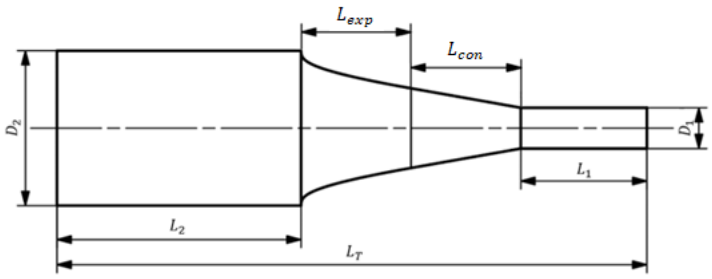

Figure 4.4: Initial geometry of the horn and corresponding identification of the dimensions of interest.

approximation of the variable profile of Figure 2.10b, which was obtained as a consequence of the insufficient information provided by Bathias and Paris (2005) about this region geometry. The mechanical properties of the material are not provided either, therefore for the first iteration the material properties considered were the following: $E = 202$ GPa, $\rho = 7800\ kg/mm^3$ and $\nu = 0.3$. At the tip of each horn, one female thread M6 is included to ensure coupling of the specimen to the horn, similarly to Furuya and Takeuchi (2014). The coupling is established in a way that there are no hollow spaces that could affect the waves propagation, and modal shape of the horns. On this account, the female threads could be removed from the finite-element analyses. According to Montalvão and Wren (2017), the same concept can be applied to the male thread of the superior horn, which is considered to be part of the piezoelectric transducer.

For the initial geometry, the approximation of the variable profile consisted on the sectioning of the variable section region into two separate regions with distinct profiles: exponential (L_{exp}) and conical (L_{con}). Nevertheless, all remainder and most relevant dimensions were kept identical to the original geometry. Despite having started with an exponential profile region like Bathias and Paris (2005), this profile was later replaced by a circular one due to the fact that circular profiles are simpler to represent in technical drawings. Otherwise, the profile would have to be represented by its mathematical equation.

Table 4.1: Dimensions and resonance frequency of the working mode along the iterative process using CTETRA(10) elements.

Iteration	Material	$D_1[mm]$	$D_2[mm]$	$L_1[mm]$	$L_2[mm]$	$L_T[mm]$	$L_{con}[mm]$	$F_{long}[Hz]$
0	Gen. Steel	10	38	31	60	145	27	22587.2
...	...	...	...	...	...	...	...	...
11	CK45 Steel	12	41	0	88	162	64.3	20126.1
12	CK45 Steel	12	41	0	90	164	64.3	19887.5
13	CK45 Steel	12	41	0	91	165	64.3	19803.8

Preserving the initial overall horn shape would involve the adjustment of 6 independent variables (L_1,L_2, D_1, D_2, L_{con} and L_{exp}) in order to obtain the desired resonance frequency. With the aim of simplifying the iterative process, D_2 was set to 41 mm to match the diameter of the transducer, and the L_1 variable was removed from the problem. Although the cylindrical part of length L_1 had a significant contribution to the horn stiffness, Bathias (2006) and Ritz and Beck (2017) conducted gigacycle fatigue tests disregarding the cylindrical tip. Both exponential and conical horns from *Laboratório de Ensaios Mecânicos e de Materiais* of Instituto Superior Técnico do not present the cylindrical tip either. In that

way, the dimension of the problem was reduced from 6 to 4 independent variables.

Throughout the iterative process, it was observed that both resonance frequency and the location of the displacement node were influenced by adjustments in the geometry of the ultrasonic horn as follows: (i) a decrease in L_1 leads to an increase of the resonance frequency, and a shift of the displacement node towards the input section; (ii) an increase in D_1 leads to a decrease of the resonance frequency, and a shift of the displacement node towards the output section; (iv) an increase in L_2 leads to a decrease in the resonance frequency, and a shift of the displacement node towards the input section.

The resonance frequency results for the longitudinal mode of vibration from iterations 11 to 13 listed in Table 4.1 indicate the extent to which the resonance frequency would be altered by adjusting the L_2 parameter post manufacture.

4.1.4 Displacement Amplitude Distribution along the Horn

The identification of the displacement node location and determination of the amplification factor were accomplished by creating a list of the displacement amplitudes along the horn longitudinal axis using the Siemens Software NX™ *query curve* command. The *query curve* was defined by all nodes along the horn axis of symmetry ($z = 0 \wedge y = 0$), resulting in a dataset of 170 nodes. The nodes coordinates along the x axis and the respective displacement results were then postprocessed to obtain the normalised displacement amplitude distribution curve, displayed on Figure 4.5. The results were normalised between -1 and 1 due to the fact that in the modal analysis under the free-free boundary condition the system is simply under free vibration. The software automatically chooses a value for the displacement and then associates that result with a certain stress value. Consequently, the software outputs results which require normalisation between -1 and 1 before being interpreted. The obtained displacement curve is consistent with the displacement amplitude distribution curve of Figure 2.7.

The most adequate location for introducing the ring for installing the mounting device is on the displacement node, which was determined by establishing a range of acceptable values for the displacement amplitudes. It was stipulated that any displacement amplitude value that deviated up to 5.00%

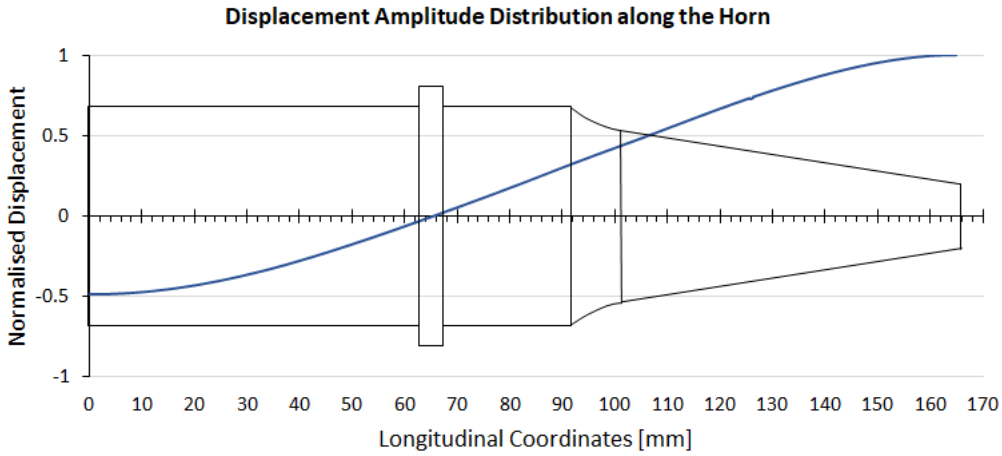

Figure 4.5: Displacement distribution along the ultrasonic horn.

from the reference value, i.e., 0.00 $\pm$ 5.00%, would be satisfactory. Table 4.2 lists the most relevant longitudinal coordinates and respective displacement values for evaluating the most suitable ring location. The resulting workable length is of 7.80 mm, and is situated in the $[61.10; 68.90]$ mm interval.

Table 4.2: Longitudinal coordinates along the horn and correspondent displacement values.

Longitudinal Coord. [mm]	Normalised Displacement Amplitude	Deviation from reference [%]
0.0	-0.481	-48.10
...	...	...
59.6	-0.065	-6.50
61.1	-0.049	-4.90
62.5	-0.032	-3.20
64.2	-0.013	-1.30
65.8	0.006	0.60
67.5	0.026	2.60
68.9	0.043	4.23
70.4	0.060	6.00
...	...	...
165.0	1.000	100.00

Taking into consideration that the assembly of the structural components of the ultrasonic machine involve the imposition of compressive stresses on both rings, it is indispensable to design these mechanical elements against structural instability. Considering the mechanical properties of the material, it was reasoned that a thickness of 5.00 mm for both horn rings was sufficient to prevent them from losing their faculty to withstand the applied loads. To further reduce the amplitude displacements in the ring region, the central cross section of the this element was aligned with the midpoint of the $[61.10; 68.90]$ mm interval, i.e. at $x = 65$mm, resulting in the placement of the ring in the sub-interval $[62.5; 67.5]$ mm. Hence, the maximal displacement allowed over the ring area is deviated 3.20% from the reference displacement value (0.00 mm). The ring diameter (55 mm) was decided upon a compromise between machining, material block availability and proper surface contact with the mounting device discs.

Applying the results of Table 4.2 to equation 2.26, it is possible to determine the amplification factor of the horn, which is explicit in equation 4.1. Taking into account the aforementioned range of possible values for this parameter (subsection 2.7.3), the result of 2.08 is considered adequate.

$$F_{amp} = \left| \frac{1}{-0.481} \right| \approx 2.08 \tag{4.1}$$

4.1.5 Stress Amplitude Distribution along the Horn

The stress distribution along the horn was determined resorting to an analogous *query curve* to the one used for the displacement amplitude distribution. The graph of Figure 4.6 represents the stress distribution along the x axis, and denotes the existence of two stress nodes, one at each extremity, meaning both surfaces are stress free. From Table 4.3 one can conclude the stress amplitude at the input and output surfaces are inappreciable (1.80% and 1.20%, respectively).

A comparison between Figures 2.7 and 4.6 allows to understand if the resulting stress curve is in

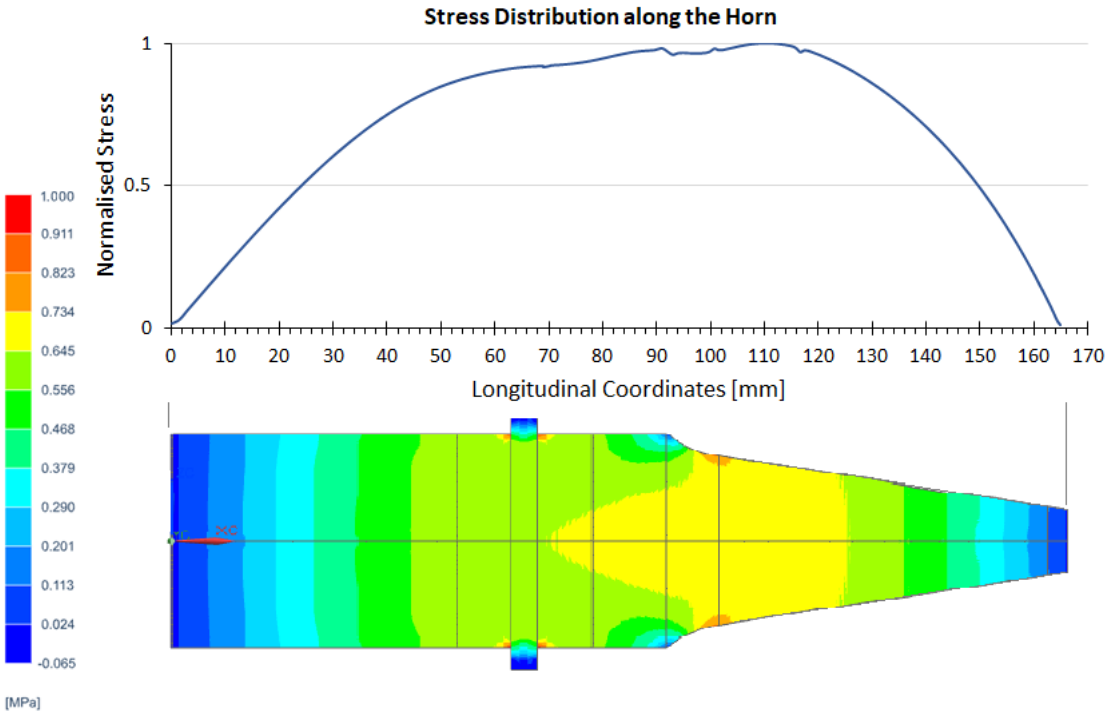

Figure 4.6: Stress distribution along the horn, where the coloured image depicts the stress distribution along the x0z plane.

accordance to what is expected based on literature. It is concluded that the stress curve corresponding to the horn length is consistent with the obtained stress results via finite-element analysis.

The sharp edges connecting the body of the horn to the ring act as stress raisers (which is evident in Figure 4.6). However, in reality at both these positions two fillets are placed instead, which were not included in the FEM analysis with the hexahedral mesh due to their complex geometry. Despite being possible to perform the modal analysis (*fillets* included) by resorting to tetrahedral elements, the results would not provide any additional relevant information besides the fact that the stress would be distributed over broader area, hence reducing the stress concentration problem. As such, the stress results over the sharp edges may be neglected due to not being in accordance with reality, i.e., the final horn geometry.

Table 4.3: Longitudinal coordinates along the horn and correspondent stress values.

Longitudinal Coord. [mm]	Normalised Stress Amplitude	Deviation from reference [%]
0.0	0.018	1.80
1.4	0.031	3.10
2.8	0.062	6.20
...	...	...
163.9	0.050	5.00
164.4	0.027	2.70
165.0	0.012	1.20

4.1.6 Mesh Convergence Analysis

Figure 4.7 resumes the mesh convergence analysis procedure and respective results. This procedure was conducted on the final horn geometry (ring included), to understand the extent to which the size of the elements affected the results accuracy. The initial test was performed based on the mesh sizes proposed by the Siemens Software NX™. In every iteration, the mesh size was simultaneously refined and adapted to the geometry of each *split body* (Figure 4.3).

The mesh of the 2^{nd} iteration was highly refined and proved to be impossible to process with the available hardware at the time, resulting in the failure of the modal analysis. A 3^{rd} iteration was nonetheless performed resorting to a mesh 20.00% smaller than the one used in the 1^{st} iteration, instead of the 40.00% of the 2^{nd} iteration.

From the 1^{st} to the 3^{rd} iteration, for an increase of 56.30% of the number on elements, the resonance frequency decreased less than 1 Hz. Additionally, it is observed that the same result is obtained with the 2 mm tetrahedral mesh (table 4.1). These results prove the natural frequency has indeed converged.

Iteration	Body	Mesh Type	Refinement [%]	Mesh Size [mm]	# Elements	Resonance Frequency of the Longitudinal Mode [Hz]
Initial	Horn (tip)	CHEXA(20)	–	1.5	32685	19813.3
	Horn(1)	CHEXA(20)		1.5		
	Horn(2)	CHEXA(20)		2.25		
	Booster(1)	CHEXA(20)		2.87		
	Booster+Disk(1)	CHEXA(20)		2.87		
	Ring	CHEXA(20)		3.43		
	Booster+Disk(2)	CHEXA(20)		2.87		
	Booster(2)	CHEXA(20)		2.87		
1st	Horn (tip)	CHEXA(20)	50	0.75	73152	19804.7
	Horn(1)	CHEXA(20)	40	0.9		
	Horn(2)	CHEXA(20)	40	1.4		
	Booster(1)	CHEXA(20)	40	1.7		
	Booster+Disk(1)	CHEXA(20)	40	1.7		
	Ring	CHEXA(20)	40	2.1		
	Booster+Disk(2)	CHEXA(20)	40	1.7		
	Booster(2)	CHEXA(20)	40	1.7		
2nd	Horn (tip)	CHEXA(20)	50	0.4	–	FAILED
	Horn(1)	CHEXA(20)	40	0.5		
	Horn(2)	CHEXA(20)	40	0.8		
	Booster(1)	CHEXA(20)	40	1		
	Booster+Disk(1)	CHEXA(20)	40	1		
	Ring	CHEXA(20)	40	1.3		
	Booster+Disk(2)	CHEXA(20)	40	1		
	Booster(2)	CHEXA(20)	40	1		
3rd	Horn (tip)	CHEXA(20)	20	0.6	114336	19803.8
	Horn(1)	CHEXA(20)	20	0.7		
	Horn(2)	CHEXA(20)	20	1.1		
	Booster(1)	CHEXA(20)	20	1.4		
	Booster+Disk(1)	CHEXA(20)	20	1.4		
	Ring	CHEXA(20)	20	1.7		
	Booster+Disk(2)	CHEXA(20)	20	1.4		
	Booster(2)	CHEXA(20)	20	1.4		

Figure 4.7: Mesh convergence procedure for the ultrasonic horn.

4.2 Ultrasonic Specimen Modelling Procedure

The present section describes the development procedure to obtain ultrasonic specimens with a 20 kHz resonance frequency. The resonance length for each specimen is first determined analytically, being the specimens geometries and frequencies subsequently analysed and adjusted numerically. To ensure that the developed method can be applied to independent specimens, two ultrasonic specimens of different materials and geometries were studied.

4.2.1 Analytical Resonance Length for the Steel and Aluminium Specimens

Two different specimens were analytically determined following Bathias and Paris (2005). All equations employed were already extensively presented and explained in section 2.4. The respective dimensional combinations were computed using Matlab software with the mechanical properties listed on Table 3.3 (steel and Al7075). Both specimens followed the Figure 2.5 hourglass shape with a circular curvature.

The Ti–6Al–4V alloy ultrasonic specimen tested by Furuya and Takeuchi (2014) under tensile mean stress conditions served as a basis when determining the initial geometric parameters that defined the aluminium specimen. For both steel and AL7075 Table 4.4 lists the established initial dimension values considered and the required resonance frequency. The analytical resonance lengths, L_1, for both specimens, are displayed in Table 4.5, along with the necessary parameters for their computation.

Table 4.4: Data for computing L_1 using the equations disclosed in section 2.4.

Parameter	Steel	Al7075	S.I. Units
R_1	$2.0 \cdot 10^{-3}$	$1.5 \cdot 10^{-3}$	m
R_2	$5.0 \cdot 10^{-3}$	$5.0 \cdot 10^{-3}$	m
L_2	$25.0 \cdot 10^{-3}$	$15.0 \cdot 10^{-3}$	m
f	20000.0	20000.0	Hz

Table 4.5: Results obtained by applying the data of Table 4.4 to the equations disclosed in section 2.4.

Parameter	Analytical Result (Steel)	Analytical Result (Al7075)	S.I. Units	Equation
α	62.672	124.921	m^{-1}	2.13
c	$5.064 \cdot 10^3$	$5.071 \cdot 10^3$	m/s	2.9
ω	$1.257 \cdot 10^5$	$1.257 \cdot 10^5$	rad/s	2.16
k	24.817	24.781	rad/m	2.15
β	57.549	122.439	-	2.17
L_1	0.011	0.015	m	2.14

4.2.2 Numerical Solutions for the Steel and Aluminium Specimens

Both specimens design were developed resorting to quadratic hexahedral elements of 20 nodes represented on Figure 4.2. The *split body* technique was employed in the specimens to ensure (i) adequate simple geometries so that the hexahedral elements could be implemented, and (ii) mesh

symmetry in all specimen sections. Finally, the nodes of subsequent surfaces were merged using the *mesh mating condition*.

Numerical Resonance Length

The specimens geometries were developed in the Siemens Software NX™. Analogously to the horns modelling procedure, the specimens design process consisted on conducting modal analyses (SOL 103 Real Eigenvalues) assuming a free-free vibration configuration with no boundary conditions to evaluate their modes shapes and respective resonance frequencies. The assessed parameter was the resonance frequency of the desired longitudinal mode.

The procedure was initiated resorting to the analytical resonance length, which was afterwards adjusted so that the resonance frequency would further approach the working frequency of the machine (20 kHz) and the analytical and numerical results could be compared. Table 4.6 provides information about the iterative process for obtaining the resonance length, L_1, for the steel specimen. A resonance frequency of 20081.8 Hz was considered sufficient, since the ultrasonic horns have a significantly higher influence on the resonance frequency of the ultrasonic set.

Since the specimen to be experimentally tested was the Al7075 one, the process for determining L_1 was conducted with additional care, in order to procure a resonance frequency closer to 20 kHz, and hence ensure results as accurate as possible to later compare them with the experimental results. Table 4.7 resumes the most relevant stages of the Al7075 specimen iterative process, where the final resonance frequency was obtained after adjusting L_1. The final resonance frequency is of 19991.60 Hz. To procure a resonance frequency closer to 20 kHz, the resonance length would have to be adjusted in the hundredths or even in the thousandths place, which would be extremely difficult and expensive to machine.

Table 4.6: Iterative process for obtaining the resonance length of the steel specimen.

Iteration	$R_1[mm]$	$R_2[mm]$	$L_1[mm]$	$L_2[mm]$	f [Hz]
0	2.0	5.0	25.0	11.0	20141.1
2	2.0	5.0	25.0	11.1	20081.8

Table 4.7: Iterative process for obtaining the resonance length of the aluminium alloy specimen.

Iteration	$R_1[mm]$	$R_2[mm]$	$L_1[mm]$	$L_2[mm]$	f [Hz]
0	1.50	5.00	15.00	15.00	20218.80
...	...	...		...	...
3	1.50	5.00	15.40	15.00	19991.60

Following the iterative process for determining the numerical resonance length of the Al7075 specimen, a mesh convergence analysis was conducted to guarantee the result accuracy was not affected by the elements size. Figure 4.8 summarises the mesh convergence analysis process and the corresponding results. The convergence analysis was initiated with the Siemens Software NX™ recommended

Iteration	Body	Mesh Type	Refinement [%]	Mesh Size [mm]	# Elements	Resonance Frequency of the Longitudinal Mode [Hz]
Initial	Constant Profile Region	CHEXA(20)	–	1.39	2464	19991.6
	Variable Profile Region	CHEXA(20)		1.39		
1st	Constant Profile Region	CHEXA(20)	20	1.11	6240	19992
	Variable Profile Region	CHEXA(20)	30	0.97		

Figure 4.8: Mesh convergence analysis results for the Al7075 specimen.

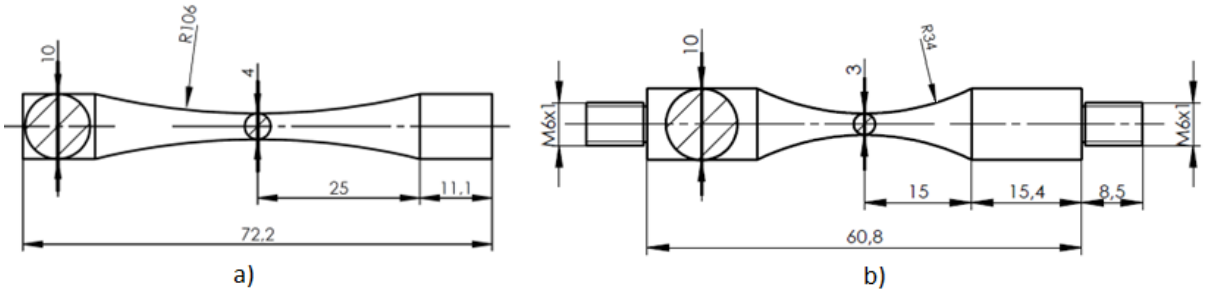

Figure 4.9: Technical drawings of the developed specimens, dimensions in mm. a) Steel; b) 7075 aluminium alloy.

mesh sizes. The number and location of the *split bodies* were kept constant throughout the entire mesh convergence analysis. From the initial stage to the 1^{st} iteration, the number of elements was increased by 153.25%, yet the resonance frequency varied by an absolute amount of 0.40 Hz. Considering the results found on Figure 4.8, no additional iterations were required to establish evidence that the resonance frequency has converged.

Equation 4.2 serves the comparison between the analytical and numerical results for the specimen resonance length, L_1^A and L_1^N, respectively. This comparison was only performed for the Al7075 specimen due to the fact that the iterative process for determining L_1^N for this specimen aimed a resonance frequency as close to 20 kHz as possible, as opposed to the steel specimen.

$$error[\%] = \left|\frac{L_1^A - L_1^N}{L_1^N}\right| = \left|\frac{15.00 - 15.40}{15.40}\right| \approx 2.60\% \tag{4.2}$$

A percentage error between the analytical and numerical resonance length of 2.60% confirms the proximity of both results. Figure 4.9a and 4.9b display the final steel and Al7075 specimen geometries. Once completed the structural analysis, one thread was added to each extremity of the Al7075 specimen to allow the coupling to the ultrasonic horns.

Displacement and Stress Distribution along the Steel and Al7075 Specimens

The displacement amplitude distribution for both specimens was obtained by creating a graph of the results along a *query curve*. Similarly to the ultrasonic horn finite-element analysis, the *query curve* was defined by all nodes along the specimen axis of symmetry ($z = 0 \wedge y = 0$), resulting in a dataset of 45 nodes for the Al7075 specimen and of 53 nodes for the steel one. The resulting datasets were then normalised by their respective maximum displacement value, resulting in curves with 1 as their uttermost value.

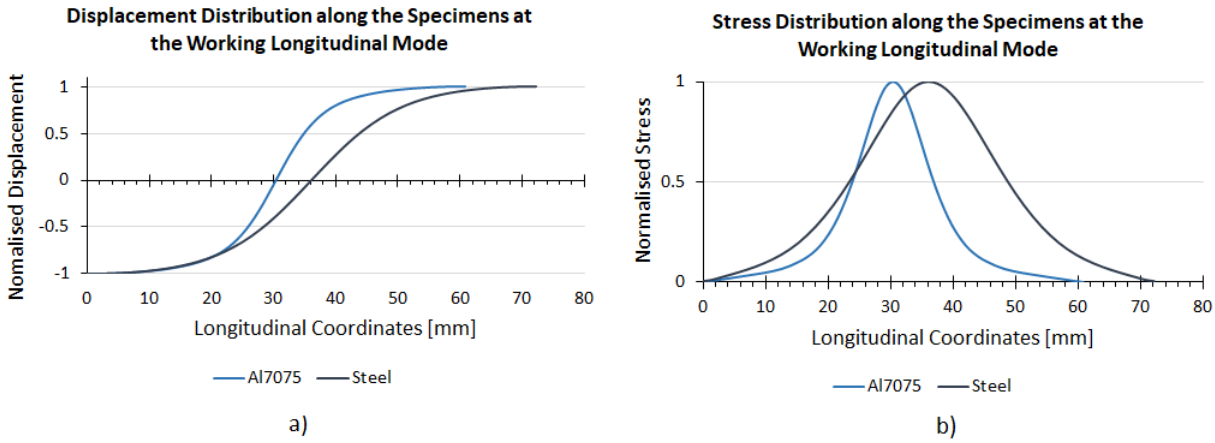

Figure 4.10: a) Displacement distribution along the steel and 7075 alloy specimen. b) Stress distribution along the steel and 7075 alloy specimen.

The curves of the displacement amplitude distribution along the specimens (Figure 4.10a) denotes the existence of one displacement node in the middle section of both steel and Al7075 specimens, and maximal displacement amplitudes at both its ends. The determined displacement curves are consistent with the displacement curve of Figures (i) 2.4 (constant section specimen in free vibration), (ii) 2.7 (variable section specimen in fully reversed condition) and (iii) 2.8 (variable section specimen with a superimposed mean stress).

Additionally, Table A.1 provides a more detailed view into the the most relevant displacement amplitudes along the aluminium specimen, which are the specimen mid-section and both extremities. It is observed that the displacement node stands exactly in the middle of the specimen, i.e., at $x = 30.4$ mm, whereas maximum displacement occurs at $x = 0.0$ and $x = 60.8$ mm.

The stress amplitude distribution curves were obtained resorting to the exact same method as the displacement amplitude curves. Concerning the curves of the graph of Figure 4.10b, it is noted that when approaching both ends, the stress amplitude rapidly decreases to zero, meaning both surfaces are stress free in both specimens. Additionally, a stress peak at both middle sections is evident, similarly to Bathias' statement represented in Figure 2.7. Table A.2 details the most relevant stress amplitudes along the aluminium specimen, namely at the centre and extremities.

4.3 Ultrasonic Set Numerical Analysis

The assemblage procedure and numerical analyses were performed on the Siemens Software NX™. Due to the complex nature of the loading condition of the experimental tests, various numerical analyses were performed under different loading and constriction conditions. The procedure was divided into three stages: (i) with no load and no boundary conditions imposed, (ii) with applied load and boundary conditions, (iii) with no applied load but with boundary conditions.

4.3.1 Free-Free Vibration Configuration with No Boundary Conditions

The first stage of the numerical analysis consisted on executing a modal analysis (SOL 103 Real Eigenvalues) with neither loads nor boundary conditions applied. The aim was to assess the mode shapes and respective resonance frequencies in a specified frequency range in the free-free vibration condition, and to ultimately evaluate the influence of the load and boundary conditions on the mode shapes and resonance frequency of the system.

The established frequency range consisted on the frequency spectrum between the lower limit of 15000 Hz and the upper limit of 23000 Hz. All mode shapes not included in this range were disregarded. The modes of vibration are numbered according to their order of occurrence in the frequency range for both ultrasonic systems. The chosen frequency range allows the searching for undesired resonance modes in the vicinity of the working mode that might affect its shape.

The results from the modal analysis regarding the ultrasonic set consisting on two horns and the steel and Al7075 specimen are displayed on Tables 4.8 and 4.9, respectively. The bending (BNDG), longitudinal (LONGL), and torsional (TOR) mode shapes occurring in the considered frequency range are listed. The results show that for both scenarios, two subsequent longitudinal modes of vibration lie within the established frequency range, therefore further evaluation of both mode shapes is required.

Mode Shape Identification	Mode Numbering	Resonance Frequency [Hz]
BNDG	1^{st}	16119.8
LONGL	1^{st}	18984.1
LONGL	2^{nd}	**19818.4**
BNDG	2^{nd}	20101.4
TOR	1^{st}	21846.5
TOR	2^{nd}	21952.4
BNDG	3^{rd}	22862.7

Table 4.8: Mode shapes and respective resonance frequency of the ultrasonic set comprising the steel specimen under the free-free vibration configuration with no boundary conditions.

Mode Shape Identification	Mode Numbering	Resonance Frequency [Hz]
BNDG	1^{st}	15212.3
BNDG	2^{nd}	17407.1
LONGL	1^{st}	19545.0
LONGL	2^{nd}	**19808.5**
TOR	1^{st}	22211.3
TOR	2^{nd}	22229.6
BNDG	3^{rd}	22312.1

Table 4.9: Mode shapes and respective resonance frequency of the ultrasonic set comprising the aluminium alloy specimen under the free-free vibration configuration with no boundary conditions.

The graph of Figure 4.11 displays the free-free modal analysis results for the displacement amplitudes of both longitudinal modes of vibration for both ultrasonic sets, providing a base for comparison. The results were obtained from *query curves* defined along the longitudinal axis of both resonant systems. For both systems, the 1^{st} longitudinal mode shape does not present a displacement node in the middle section of the specimen, in fact in this section the displacement amplitude achieves it utmost value. On the other hand, the 2^{nd} longitudinal mode not only exhibits a displacement node in the specimen mid-section, but also maximal displacement amplitude in both specimen-horn connections. This information is sufficient to conclude that the working longitudinal mode of vibration for the ultrasonic set with the steel specimen resonates at 19818.37 Hz, and at 19808.5 Hz for the system comprising the Al7075 specimen, if no load nor boundary conditions are applied. Actually, the curves of Figure 4.11 reveal that the 1^{st} longitudinal mode of both systems are equivalent concerning their shapes, and the

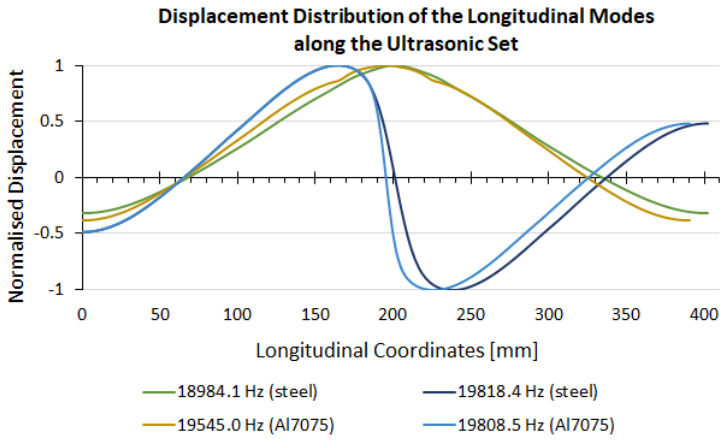

Figure 4.11: Displacement distribution of the first and second longitudinal modes, referred in Table 4.8 and Table 4.9, along the ultrasonic system for the steel and 7077 aluminium alloy specimens.

same applies to the 2^{nd} longitudinal mode shape of vibration.

Concerning the mode shapes developing in the vicinity of the working mode, for the steel specimen system the 2^{nd} bending mode of vibration is the nearest from the working mode shape, only apart by 283.0 Hz. The remainder mode shapes are sufficiently distanced from the working longitudinal mode ($>$ 500 Hz) and may therefore be disregarded.

The ultrasonic set comprising the aluminium alloy specimen likewise exhibits one mode shape that might interfere with the working longitudinal mode (the 1^{st} longitudinal mode), differing by 263.5 Hz. Similarly to the steel specimen ultrasonic set, the remainder vibration modes are distanced by more than 500 Hz, and may be considered negligible. However, once the boundary conditions are imposed, other mode shapes are expected to develop in both ultrasonic sets.

4.3.2 Loading Condition 1

The second numerical analysis consisted on the load employment to reproduce the effect of the static tensile load induced by the electromechanical machine. In the experimental procedure, once the resonant system is properly installed, the crosshead of the electromechanical machine moves either upwards or downwards, depending if the the tests are conducted under tensile or compressive conditions, respectively. As soon as the predetermined loading conditions are met, the electromechanical machine initiates the load control and its crosshead will be continuously adjusted to maintain the pre-established loading conditions. Replicating such conditions on the finite-element analysis proved to be difficult, due to the fact that if the upper outer ring was to be restricted in all directions, then the applied load would not have any effect on the middle section of the specimen, and would be impossible to simulate a VHCF test with a superimposed static load.

For the second stage of the finite-element analyses of both the resonant systems, a structural analysis was conducted resorting to the *Nastran* solver. The solution incorporated two distinct solution types: the subcases (i) *statics* - SOL 101 Linear Statics, and (ii) *normal modes* - SOL 103 Real Eigenvalues. To simulate a vibrating system with a superimposed mean stress, the applied load was defined in the

linear statics solution, which results served afterwards as base to the modal analysis. Additionally, the constraints were defined as follows: (i) inferior outer ring with all six degrees of freedom (DOFs) fixed, and (ii) superior outer ring with all DOFs fixed, except DOF1, allowing motion in the longitudinal direction.

Linear Statics Solution

Tables 4.10 and 4.11 display the results for the maximal displacement amplitudes obtained through the finite-element analyses for each static loading condition, for the steel and the Al7075 specimen, respectively. The analytical mean stress corresponds to the numerical maximal stress in the specimen, hence both results are also presented and compared.

The analytical mean stress was determined using equation 4.3, where F and A_{ms} correspond to the applied load and area of the mid-section of the specimen, respectively. Regarding the set including the steel specimen, the difference between the analytical and numerical stress results is of approximately 0.6% for every applied load, whereas for the set comprising the Al7075 specimen, the difference is of approximately 1.3%.

$$\sigma_{mean} = \frac{F}{A_{ms}} \tag{4.3}$$

Table 4.10: Analytical and numerical mean stress results (MPa), for different values of applied static loads (kN) for the ultrasonic system comprising the steel specimen.

Applied Load $[kN]$	Analytical Mean Stress [MPa]	Numerical Mean Stress [MPa]	Mean Stress Error [%]
1	79.6	80.1	0.62
2	159.2	160.1	0.56
3	238.9	240.2	0.54
10	796.2	800.7	0.56
20	1592.4	1601.4	0.56
100	7961.8	8007.1	0.57
300	23885.4	24020.0	0.56

Table 4.11: Analytical and numerical mean stress results (MPa), for different values of applied static loads (kN) for the ultrasonic system comprising the 7075 aluminium alloy specimen.

Applied Load $[kN]$	Analytical Mean Stress [MPa]	Numerical Mean Stress [MPa]	Mean Stress Error [%]
1	141.5	143.3	1.25
2	282.9	286.6	1.29
3	424.4	429.9	1.27

Figure 4.12 shows the stress amplitudes results from the numerical analysis, for an applied tensile load of 1 kN on the ultrasonic set comprising the Al7075 specimen. It can be observed that the maximum stress, 143.3 MPa, occurs in the middle section of the specimen. It was also observed that the maximum stress location remains unaffected as the applied tensile load increased. Analogous results were obtained for the ultrasonic set incorporating the steel specimen.

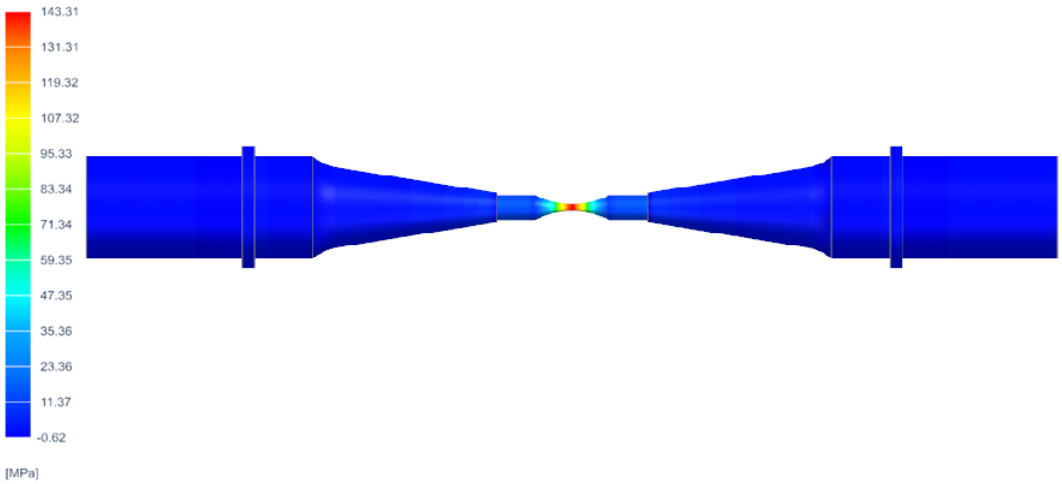

Figure 4.12: Stress results (in MPa) obtained from the Linear Statics Solution regarding the ultrasonic set comprising the Al7075 specimen.

Normal Modes Solution

The resultant modes of vibration for several applied tensile loads are displayed on Tables 4.12 and 4.13 for the ultrasonic sets comprising the steel and Al7075 specimens, respectively. The vibration modes are sorted from lowest to highest frequency. It is important to highlight the fact that the capacity of the used load cell was of 10 kN, meaning the purpose of the simulations that employed loads greater than that value is to merely assess the evolution tendency of the vibration modes, otherwise the change in the resonance frequency of some vibration modes would be imperceptible.

Table 4.12: Frequencies (in Hz) of the different modes of vibration that the ultrasonic system comprising the steel specimen develops in the for a given applied static load (in kN).

Load	1^{st}	1^{st}	1^{st}	2^{nd}	2^{nd}	3^{rd}	2^{nd}	3^{rd}	4^{th}
$[kN]$	BNDG	LONGL	TOR	TOR	LONGL	**LONGL**	BNDG	BNDG	BNDG
1	15909.6	16125.0	16750.2	16792.2	19333.1	**20144.9**	20323.9	20640.0	21213.9
2	15923.6	16125.0	16750.3	16792.3	19333.1	**20144.9**	20325.6	20651.1	21219.9
3	15937.6	16125.0	16750.4	16792.4	19333.1	**20144.9**	20327.1	20662.1	21226.1
10	16034.0	16125.0	16751.2	16793.1	19333.1	**20144.9**	20334.8	20732.5	21275.8
20	16167.1	16125.1	16752.3	16794.1	19333.1	**20144.9**	20341.3	20811.1	21365.5
100	17072.2	16125.6	16761.0	16802.0	19333.3	**20145.0**	20355.1	20988.2	22305.2
300	18575.0	16127.0	16782.5	16821.5	19333.7	**20145.4**	20363.2	21053.0	———

Table 4.13: Frequencies (in Hz) of the different modes of vibration that the ultrasonic system comprising the Al7075 specimen develops in the for a given applied static load (in kN).

Load	1^{st}	1^{st}	2^{nd}	1^{st}	2^{nd}	3^{rd}	2^{nd}	3^{rd}
$[kN]$	LONGL	TOR	TOR	BNDG	LONGL	**LONGL**	BNDG	BNDG
1	16321.9	16880.3	16888.2	17535.6	19878.4	**20158.4**	20400.9	21067.0
2	16321.9	16880.4	16888.3	17588.8	19878.4	**20158.4**	20401.0	21067.7
3	16321.9	16880.5	16888.4	17641.1	19878.4	**20158.4**	20401.2	21068.5

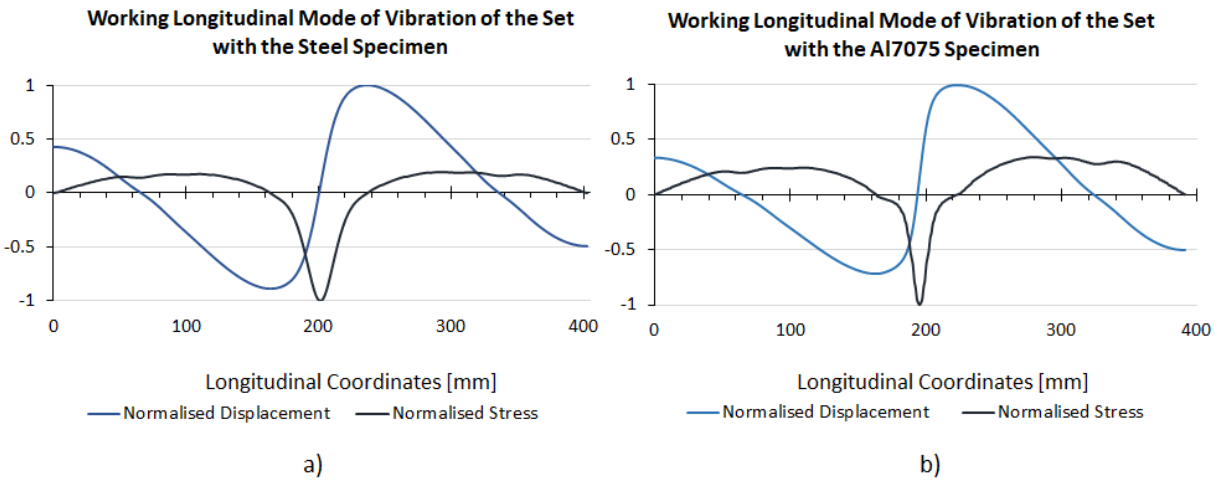

Figure 4.13: Displacement and stress distribution along the ultrasonic systems with an applied static load of 1000 N. a) System comprising the steel specimen. b) System comprising the Al7075 specimen.

The vibration mode required for conducting fatigue tests in axial conditions with a superimposed constant mean stress in the VHCF regime is the 3^{rd} longitudinal mode for both the steel and aluminium alloy specimen (tables 4.12 and 4.13, respectively). Figures 4.13a and 4.13b display the displacement and stress distribution curves corresponding to the 3^{rd} longitudinal mode of vibration with respect to the steel specimen resonant system and the aluminium alloy specimen system, respectively.

Although the curves of Figure 4.13 resemble the ones presented on Figure 2.8b, it is evident that both displacement and stress distribution curves are not symmetrical about the middle section of the specimen, which is even more perceptible in the resonant system comprising the Al7075 specimen. This mechanical behaviour may be a result of the applied asymmetrical boundary conditions, since for these particular analyses, the upper outer ring was allowed to move along the x axis. Being the defined constrictions slightly different from the actual constrictions presented on the experimental tests, it is important to evaluate the impact of the applied load in the resonant system behaviour to understand if one may safely perform other modal analysis disregarding the load, but imposing the true boundary conditions.

Comparing the results listed in Table 4.8 for the free-free vibration configuration with the results of Table 4.12, it was found that the resonance frequency of the working longitudinal mode of the system comprising the steel specimen increased by 1.62% and remained constant in the interval of possible applied loads, $[1, 10]$ kN. Regarding the Al7075 specimen, in the compared results from Tables 4.9 and 4.13, an increase of 1.74% was observed. The difference between the results remained constant in the $[1, 10]$ kN interval as well. These results evidence that once the tensile loads are applied, a negletable change ($<$ 2.0%) in the resonance frequency of the working mode is expected.

To better visualise the tendency of the modes as the applied load increases on the ultrasonic systems comprising the steel specimen, the results from Tables 4.12 and 4.13 were plotted. The resulting graphs are presented in Figures 4.14 and 4.15. An inspection to both graphs led to the following observations regarding the ultrasonic set comprising the steel specimen:

1. Ultrasonic Set comprising the Steel Specimen

   - The 1^{st} bending mode tends to approach the working mode of vibration for applied loads greater than 300 kN;
   - Both 3^{rd} and 4^{th} bending modes show clear evidence of diverging from the working mode as the applied load increases;
   - All the remainder vibration modes remain unaffected.

2. Ultrasonic Set comprising the Al7075 Specimen

   - In the assessed range of applied tensile loads, all vibration modes remain unaffected.

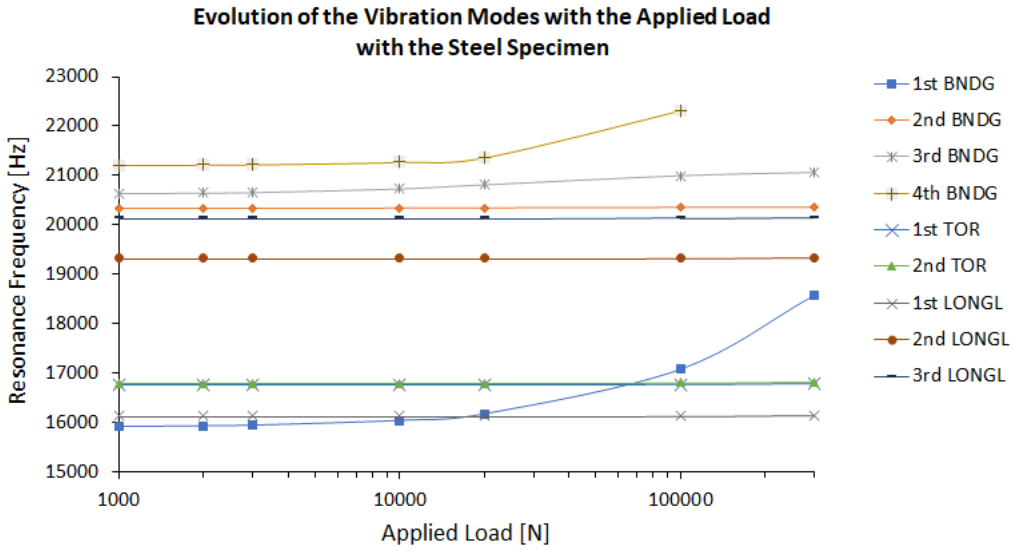

Figure 4.14: Evolution of the resonance frequency of each developing mode shape for an increasing applied static load regarding the ultrasonic system comprising the steel specimen.

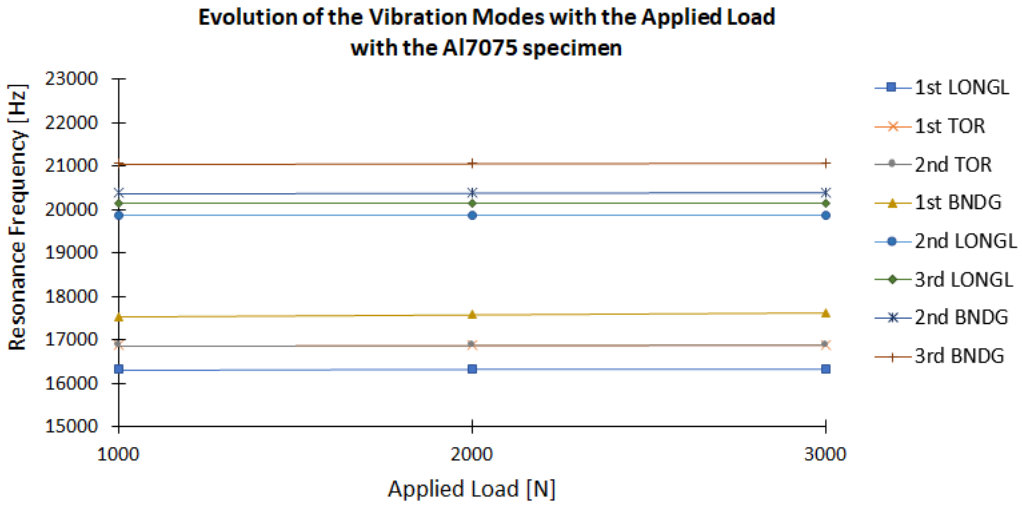

Figure 4.15: Evolution of the resonance frequency of each developing mode shape for an increasing applied static load regarding the ultrasonic system comprising the Al7075 specimen.

For tensile loads from 1000 N to 3000 N, both resonant systems behave similarly, since neither of them present any parasite mode that might potentially approach the working longitudinal mode of vibration. Based on these results, and considering the displacement amplitude in VHCF tests is extremely low (in the order of micrometers), it can be assumed that the mechanical behaviour of the ultrasonic system comprising the aluminium alloy specimen as the applied load increases, will be similar to the one presented by the system comprising the steel specimen. Therefore one may expect that in the range of possible applied tensile loads, the parasite modes are not expected to interfere with the working longitudinal mode of vibration in either resonant system. The fatigue tests under axial conditions in the VHCF regime may therefore be conducted under any tensile load applied by the load cell.

Additionally, the steady behaviour of the resonant frequencies of all vibration modes with the load increments in the $[1, 10]$ kN range, imply that load impact on the dynamic behaviour of the resonant systems is negligible. As such, one can safely conduct a modal analysis with the true constraints employed on the experimental procedure, while disregarding the load. Such analysis will enable the forecasting of the actual behaviour of the resonant systems.

4.3.3 Loading Condition 2

The analysis presented in this subsection aims to accurately replicate the boundary conditions applied onto the resonant system when conducting ultrasonic $R \neq -1$ VHCF tests. Although in the present section only the resonant system comprising the Al7075 specimen is analysed in further detail, an equivalent analysis was also conducted regarding the steel specimen, which results are presented in Appendix B.

Any resonant system consisting on the same ultrasonic horns but with a different axisymmetric hourglass ultrasonic specimen of either the same or a different material, still resonating at approximately 20 kHz, is expected to behave similarly to the one presented in this subsection. The expected similarity of the dynamic behaviours of the resonant systems is based on the facts that (i) the applied constraints do not vary with the system and (ii) each system is symmetrical about the centre of the specimen.

Regarding the imposed boundary conditions, it was established that both outer rings would be fixed, i.e., no movement was allowed in any direction. A modal analysis (SOL 103 Real Eigenvalues) was then executed using the *Nastran* solver.

Table 4.14 lists all the vibration modes resonating in the $[15, 23]$ kHz frequency range. Four longitudinal modes of vibration lie within the established frequency range, however only two of them (the 3^{rd} and 4^{th} longitudinal modes) present a resonance frequency close to 20 kHz. Therefore further evaluation of both mode shapes is required to verify which one of them is the mode of interest. Hence, the displacement distribution of both vibration modes were plotted and assessed (Figure 4.16a).

A 403 point *query curve* along the longitudinal axis ($z = 0 \wedge y = 0$) of the resonant system was defined to obtain the data corresponding to the displacement and stress distribution results across the resonant system. The dataset was defined ensuring the presence of one point in the middle section of the specimen, and consequently in the the exact centre of the resonant system, enabling the possibility

Table 4.14: Mode shapes and respective resonance frequency for the ultrasonic set comprising the aluminium alloy specimen under Loading Condition 2.

Mode Shape Identification	Mode Numbering	Resonance Frequency [Hz]
BNDG	1^{st}	15147.7
LONGL	1^{st}	16256.1
LONGL	2^{nd}	16388.1
TOR	1^{st}	16880.2
TOR	2^{nd}	16888.1
BNDG	2^{nd}	17735.4
LONGL	3^{rd}	19939.3
LONGL	4^{th}	**20193.8**
BNDG	3^{rd}	21047.6
BNDG	4^{th}	21088.6

of retrieving the displacement and stress values at this section. By inspecting the curves presented of Figure 4.16a, one may straightforwardly identify the 4^{th} longitudinal mode as the working resonant mode.

Figure 4.16b plots the displacement and stress distributions of the working mode. The distribution curve was plotted based on the data listed in Table B.4 (in the Appendix), which displays the normalised displacement amplitudes in the regions of greatest interest, namely the outer rings regions ($[62.2; 68]$mm and $[322.8; 328.6]$mm), the horn-specimen connections (165.0 mm and 225.8 mm), and the centre of the specimen (195.4 mm). The third column of Table B.4 (in the Appendix) quantifies the deviation of the displacement amplitude from the reference displacement value. It is possible to observe the following regarding the displacement distribution along the resonant system:

- The maximum displacement amplitude occurs symmetrically at both horn-specimen connections, i.e., at 165.0 mm and 225.8 mm;
- Three displacement nodes occur along the resonant system, being one exactly in the middle section of the specimen, i.e., at 195.4 mm, and the remainder two at each mounting device region;
- The deviation of the displacement amplitude from the reference value in both outer ring regions is inferior to 3.90%.

Table B.5 (in the Appendix) lists the stress amplitude values at the most relevant sections of the resonant system. One may therefore conclude the following:

- The resonant system presents four stress nodes, being two of them at each horn-specimen connection, other at the horn-converter connection, and one at the inferior horn free end. At all these locations, the stress amplitude is deviated by a maximum of 0.70% from the established reference value;
- The maximum stress amplitude occurs at the centre of the specimen, i.e., 195.4 mm, and the stress distribution curve is symmetrical about this location.

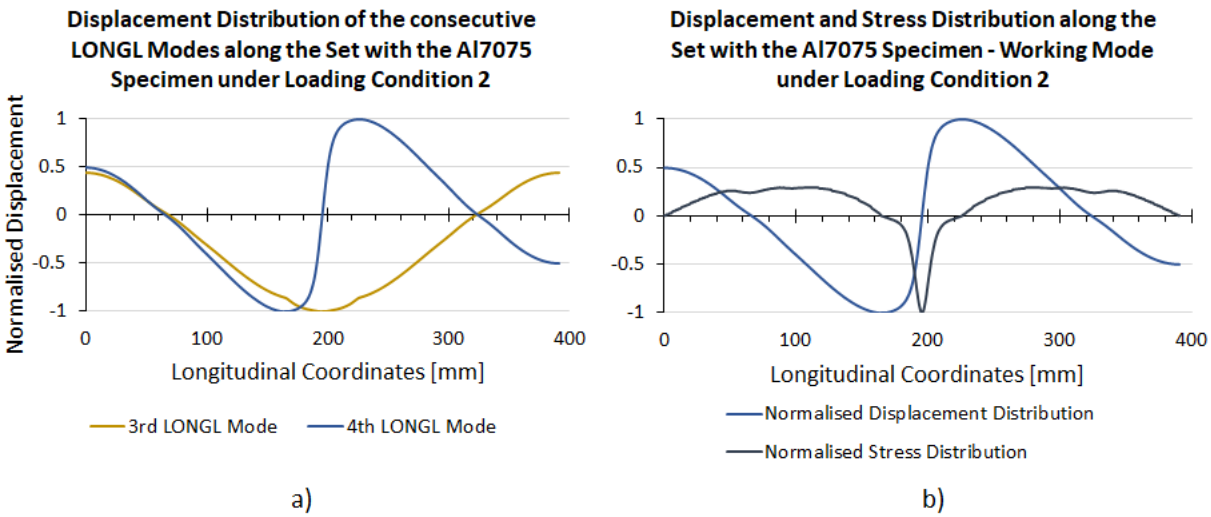

Figure 4.16: a) Displacement distribution along the system comprising the aluminium alloy specimen for the third and fourth longitudinal modes of vibration under Loading Condition 2 (see Table 4.14). b) Displacement and stress distribution of the working mode along the system comprising the aluminium alloy specimen under Loading Condition 2.

Chapter 5

Experimental Tests and Results

This chapter describes the procedures and equipment required to conduct the experimental tests, which were only performed on the aluminium alloy specimen. A series of preliminary experimental dynamic tests are presented and detailed, as well as experiments under different conditions. Finally, a new method developed for determining the experimental conditions required to meet a pre-established prerequisite is presented, along with the fatigue test results for two identical aluminium alloy specimens (Specimen 1 and Specimen 2).

5.1 Equipment

The experimental tests were conducted in an integrated system composed by a resonant system, a signal generator, a data acquisition system and a control system commanded through a LabView routine similar to Lage et al. (2012).

The resonant system consists of the piezoelectric transducer, the ultrasonic horns and the specimen, all assembled in series. Figure 5.1 showcases the schematic of the integrated system. The piezoelectric transducer is a 2.2 kW Branson with a 20 μm peak-to-peak of maximum amplitude, and is connected to the signal generator to convert the sinusoidal electrical signals of 20 ± 0.5 kHz into mechanical vibrations.

The signal generator unit was a Branson DC222 with a working frequency of 20 ± 0.5 Hz, with an external power supply unit (a Mean Well RS-100-24). The signal generator determines the resonant frequency by performing a frequency scan analysis.

The data acquisition system consists of the data acquisition device (DAQ), which is a NI USB-6351 that connects directly to the computer and allows monitoring the data from the pyrometer, laser and strain gauge by working as a bridge between them and the Labview routine. Subsection 5.1.2 provides information concerning strain gauges theory and the type employed.

The pyrometer was used to monitor the temperature of the specimen throughout the whole fatigue tests. The convenience of resorting to a pyrometer to assess the temperature fluctuations on the system under analysis over the experimental tests lies on the fact that no contact between the system and the device is required.

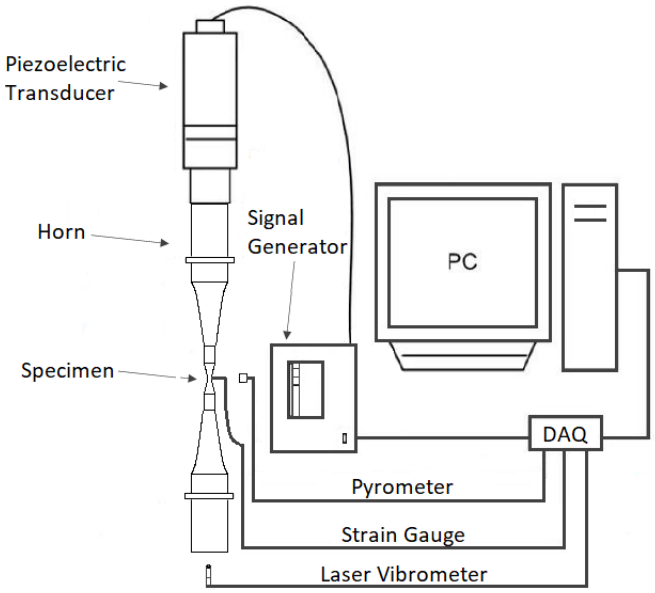

Figure 5.1: Schematic representation of the ultrasonic fatigue system under analysis.

The two-channel laser doppler vibrometer (LDC) with a Polytec OFV-518 fiber interferometer sensor head and a Polytec OFV 2082i electronic unit was used to determine both the displacement and phase of the body or system in analysis. Reflective tape was carefully placed and glued to the surface of interest of the body or system in analysis so that the laser beam could be adequately reflected in order to obtain accurate measures. Despite having two channels available, only one was necessary. The channel was placed perpendicularly to the surface of interest, at a distance of approximately 10 to 15 centimetres, using a magnetic stand equipped with an adjustable clamp holder.

The LabView routine may operate the piezoelectric transducer in two distinct conditions: (i) by controlling power, and (ii) by controlling the displacement amplitude. When testing under the power control condition, the operator is required to specify the working power in the LabView routine, and the system applies the highest displacement amplitude possible associated with the stipulated power. On the contrary, when testing under displacement control condition, the operator is required to specify the operating displacement amplitude, and the system applies the lowest power required to obtain the stipulated displacement amplitude. Additionally, the control system provides the possibility of interrupting the experiment whenever the pyrometer detects a temperature rise above a pre-established maximum temperature. The test is hence temporarily suspended until the temperature at the centre of the specimen drops to an acceptable value so that the test can be resumed. The LabView routine also determines the working frequency and displays the number of cycles until the end of the test.

A thermographic camera was used in the preliminary experimental dynamic tests to identify the regions of higher temperature along the specimen, hence confirming whether or not maximum stress was occurring in the middle section of the specimen. This device works by detecting infrared energy (IR) to produce thermal images. Longer periods of fatigue testing were possible due to the introduction of continuous cooling using fans pointing at the electromechanical machine electric engine and at the resonant system. Additionally, a blower was coupled to one of the guide rods and directed at the specimen.

5.1.1 Surface Preparation

The specimens must go through a succession of surface preparation procedures preceding the fatigue tests, such as surface finishing and coating.

Lesperance et al. (2021) stated that most aluminium alloys spend their entire fatigue life propagating existent cracks that originated from imperfections such as pores, oxide inclusions or secondary phase particles, and that the existence of those imperfections may accelerate the crack propagation rate. On that account, the surfaces of the specimens were smoothen using abrasive sheets of gradually finer grits, eliminating deep scratches that could be the site of crack initiation during the fatigue tests. Figures 5.2a and 5.2b show, respectively, the finished surface around the middle section of specimens 1 and 2.

Concerning the dynamic tests resorting to strain gauges, it is necessary to thoroughly clean the surface of the specimens before gluing the strain gauges, as will be explained in subsection 5.1.2. For the fatigue tests, the specimens were coated in a heat resistant matte black spray paint to help controlling the temperature.

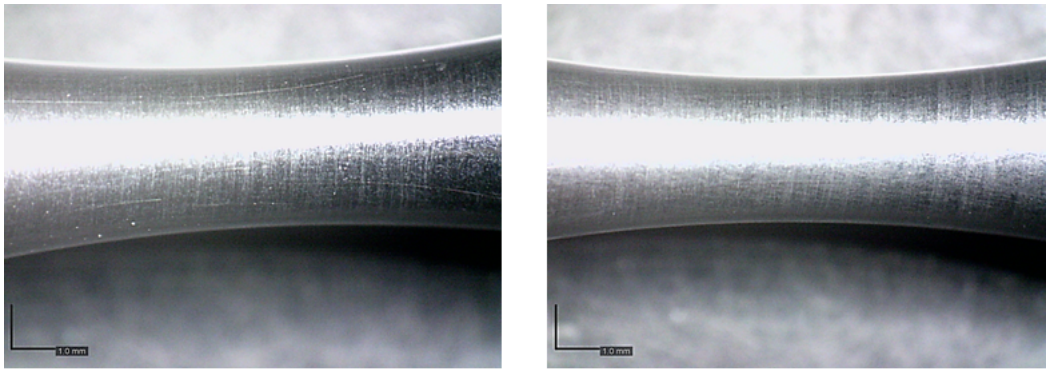

Figure 5.2: Surface finishing of the specimens. a) Specimen 1. b) Specimen 2.

5.1.2 Strain Gauges

Strain gauges were used to measure locally the ratio of the change in length of the specimen under testing, i.e., the strain parameter. As the axial specimens were designed to vibrate solely longitudinally (see subsection 4.2.2), a single strain gauge was sufficient to determine the strain fluctuations at the region of maximum strain and, consequently, maximum stress over the experimental tests. In the elastic regime the measured strain may be converted into stress results by applying the the Hooke's Law.

Strain gauges may vary in (i) size, (ii) shape, and (ii) number of gauges. These devices are glued to the region of interest by means of a proper adhesive, and are composed by an insulated conductive metal foil in a zig-zag pattern of parallel lines and two leads that pass the current through the gauge. Figure 5.3a[1] showcases the strain gauge and its main elements. The metal foil deforms in unison with the specimen, inducing a change in its electrical resistance: the electrical resistance increases when

[1] www.bestech.com.au/blogs/understanding-a-wheatstone-bridge-strain-gauge-circuit

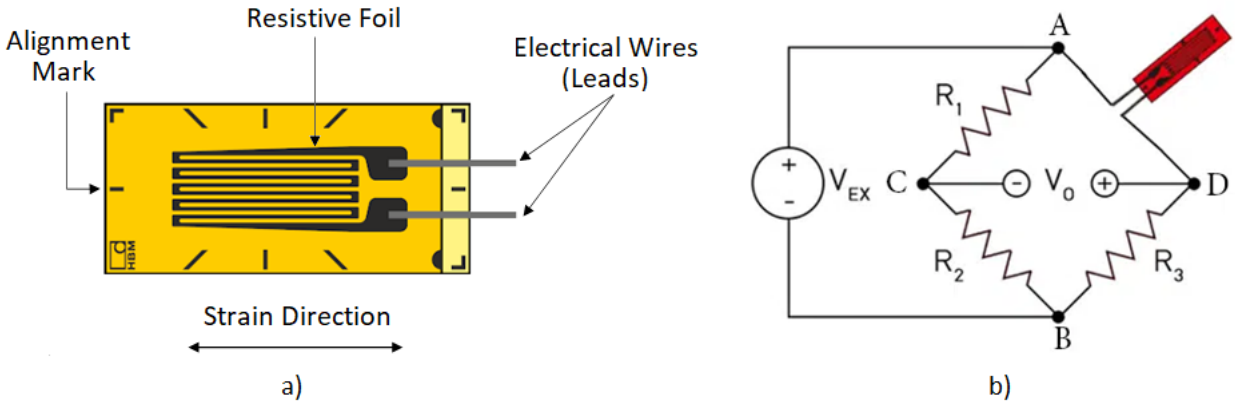

Figure 5.3: a) Strain Gauge ; b) Wheatstone Bridge (quarter bridge).

the foil is under tensile stresses, and decreases when under compressive stresses. The change in the electrical resistance of the foil is proportionally related to the strain by means of a *gauge factor*.

The change in the electrical resistance of the foil is measured by means of a Wheatstone bridge (see Figure 5.3b[2]), which consists of three resistors of known resistance and another resistor which is the strain gauge. The bridge circuit is connected to a DC power supply unit through points A and B, and the voltage is measured between points C and D of Figure 5.3b. This circuit may be employed either in *balanced* or *unbalanced condition*. When in *balanced condition* the voltage between points C and D equals zero ($V_0 = V_C - V_D = 0V$). Being the ratio R_1/R_2 fixed, and using a variable resistor for R_3, it is possible to regulate R_3 and hence to determine the value of the strain gauge resistance,R_x, using the equation $R_1/R_2 = R_x/R_3$.

For measuring strain the Wheatstone bridge is operated in the *unbalanced condition*. When the surface to which the strain gauge is glued to deforms, the strain gauge resistance changes accordingly, turning the circuit unbalanced: increased strain causes the voltage difference to rise, whereas no strain causes the circuit to balance. Due to the fact that the strain gauge resistance may be influenced not only by strain variations but also by temperature changes, it is usually of significant importance to select a strain gauge with a coefficient of thermal expansion that matches the one of the material under analysis. By ensuring similarity between these parameters, one may expect that both the material of the body and strain gauge stretch and shorten coherently, thus preventing unreliable measurements of the strain fluctuations. Additionally, it is of good practise to maintain the room temperature as constant as possible during the experimental procedures.

The strain gauge used for the tests was purchased from *Tokyo Sokki Kenkyujo Co., Ltd* and has the following characteristics: (i) gauge length of 1 mm, (ii) gauge resistance of $120 \pm 0.3\Omega$, (iii) gauge factor of $2.11 \pm 1\%$, and (iv) coefficient of thermal expansion of $11.8 \times 10^{-6}\ ^\circ/C$. In order to ensure adequate gluing of gauge to the surface of the specimen, the latter was cleansed using acetone. This solvent freed the surface of the specimen from dust, paint and grease residues.

After cleansing the surface, a *connecting terminal* was glued onto the surface of the specimen on the region of constant diameter (see Figure 5.4a). The centre of the specimen was also carefully marked

[2] www.bestech.com.au/blogs/understanding-a-wheatstone-bridge-strain-gauge-circuit

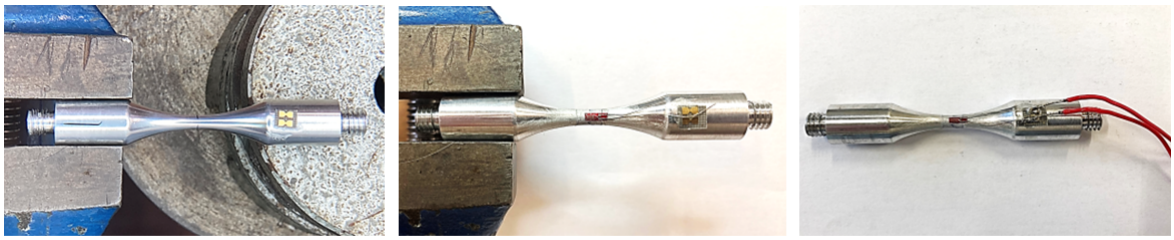

a) b) c)

Figure 5.4: Procedure for gluing the strain gauge to the specimen.

to ensure that the direction in which the gauge measures strain (identified with alignment marks) is adequately positioned onto the specimen. The strain gauge was glued onto the surface of the specimen, precisely in its mid-section (see Figure 5.4b), which is the region where the fatigue crack is most likely to initiate due to the specimen specific geometry. The electric wires of the strain gauge was then welded to the connecting terminal (see Figure 5.4c).

5.2 Preliminary Experimental Dynamic Tests

The present section describes and assesses the conducted preliminary experiments, which were conducted without superimposed static loading. The following experiments had the aim of (i) determine the amplification factor of the ultrasonic horn, (ii) ensure the specimen has an amplification factor of 1, meaning it does not amplify the wave that propagates through the system. In addition, tests on the complete resonant system under both unclamped and clamped conditions are described and their results presented.

5.2.1 Horn Amplification Factor Assessment

The experimental test to ascertain the amplification factor of the ultrasonic horn consisted on determining and comparing the displacement (i) at the booster only setup and (ii) at the lower end of one of the manufactured horns of this study attached to the previously measured booster. All displacement measurements were made using the described laser vibrometer equipment. The test was repeated for different transducer amplitudes. The booster used for conducting these tests was the one used in the Costa et al. (2019) experiments.

Figure 5.5 shows the displacement amplitude for an increasing transducer amplitude at the lower end of the booster and of the system comprising one booster and one horn. Both systems follow, as expected, a linear behaviour. By resorting to the slope of their respective linear regressions one may estimate the horn amplification factor. Recalling equation 2.26, the experimental horn amplification factor is given by equation 5.1.

$$F_{amp} = \frac{0.5606}{0.2667} = 2.10 \tag{5.1}$$

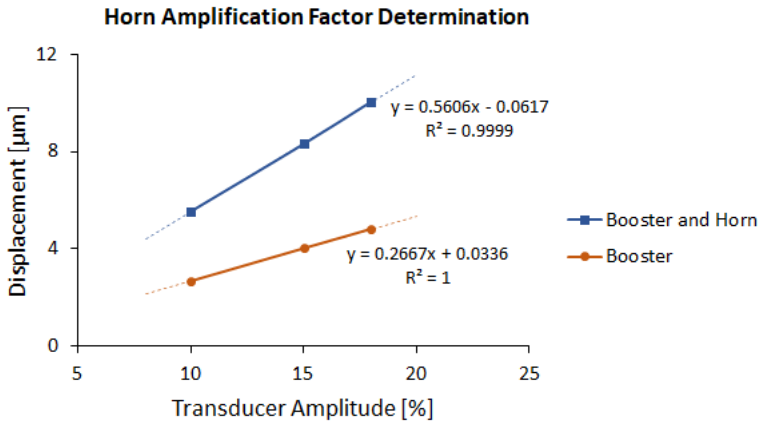

Figure 5.5: Horn Amplification Factor assessment based of the displacement measured for increasing transducer amplitudes. The booster employed in the experiments was one of the boosters available in the *Laboratório de Ensaios Mecânicos e de Materiais* of Instituto Superior Técnico.

The numerical analysis of the ultrasonic horn suggested an amplification factor of 2.08 (see subsection 4.1.4). The similarity of the numerical and experimental amplification factors indicate that the ultrasonic horn behaves consistently with the numerical results, with an inappreciable error of 0.95%.

Figure 5.6a displays the deformation speed fluctuations at the lower end of the *booster and horn* system over the entire test conducted under a transducer amplitude of 10%. One may observe (i) the initial static equilibrium, (ii) the transient response, which is an adjusting dynamic response of the system to the disturbance of its static equilibrium, and (iii) the steady-state response, which is the response of interest. Figure 5.6b shows the deformation speed fluctuations over a time interval of 0.001 s so that one may straightforwardly perceive the harmonic shape of the signal, meaning the behaviour of the *booster and horn* system is in fact in the elastic regime.

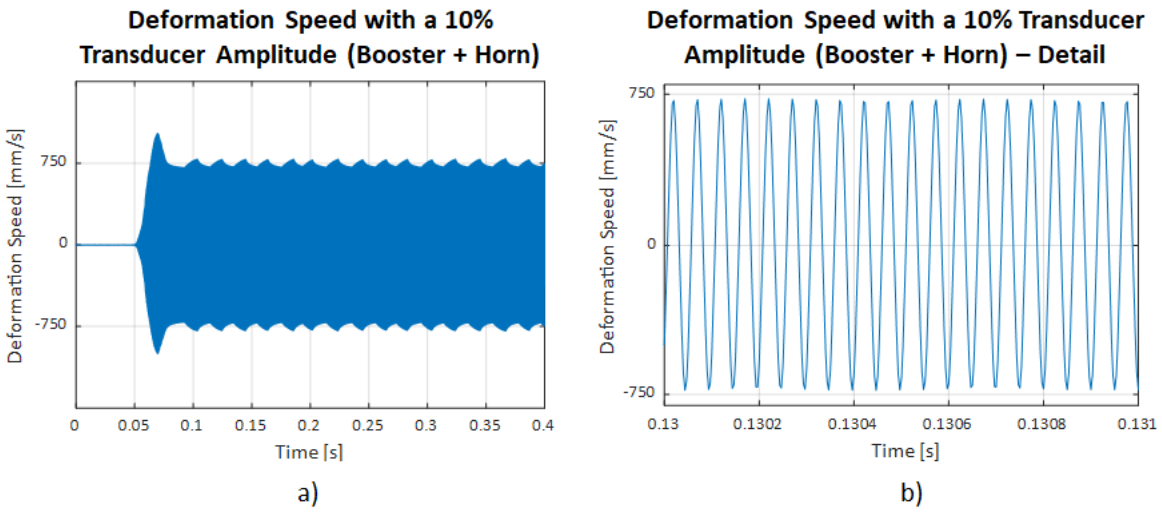

Figure 5.6: Deformation speed fluctuations of the system comprising one booster and one horn at a 10% transducer amplitude. a) Over the entire test. b) Over a period of 0.001 s.

5.2.2 Specimen Amplification Factor Assessment

The following preliminary experiment consisted on on determining and comparing the deformation speed measured (i) at the lower end of the horn in the booster-horn setup and (ii) at the lower end of the specimen for different transducer amplitudes.

Firstly, the laser vibrometer was used to determine the deformation speed at the lower end of the ultrasonic horn. Figure 5.7 displays the deformation speed fluctuations at the lower end of the system composed solely by the horn over (a) the entire test conducted under a transducer amplitude of 10%, and (b) a 0.001 s time interval. A set of points within the steady-state regime were identified to evaluate the deformation speed at a 10% power. In that regard, a sample of 10000 points in the steady-state regime was defined. The deformation speed was estimated based on the mean value of all values equal or above a specified threshold of 335 mm/s. The same methodology was employed to assess the deformation speed of the ultrasonic horn under a transducer amplitude of 15% and 20%, being the respective thresholds and results displayed in Table 5.1 and in Figure C.1. When resonating alone, although approaching an harmonic wave, the signal exhibits noise. It is unclear what may be causing the irregularities in the harmonic wave shape, since no other mode shapes were detected neither in the FEA within the $[19000; 21000]$Hz range, nor in the frequency scan analysis (as will be explained next).

Table 5.1: Deformation speed of the system comprising solely one horn.

	*P*10[%]	*P*15[%]	*P*20[%]
Threshold [mm/s]	335	490	660
Average [mm/s]	347.1	524.1	704.6

A frequency scan analysis was conducted to assess the dynamic response of the system, which in the present experiment is composed solely by the ultrasonic horn, to an induced current at increasing frequency. The analysis was performed by the control system of the transducer within the $[19450; 20450]$Hz range, and the results are presented in Figure 5.8. The results show that a single resonant mode of

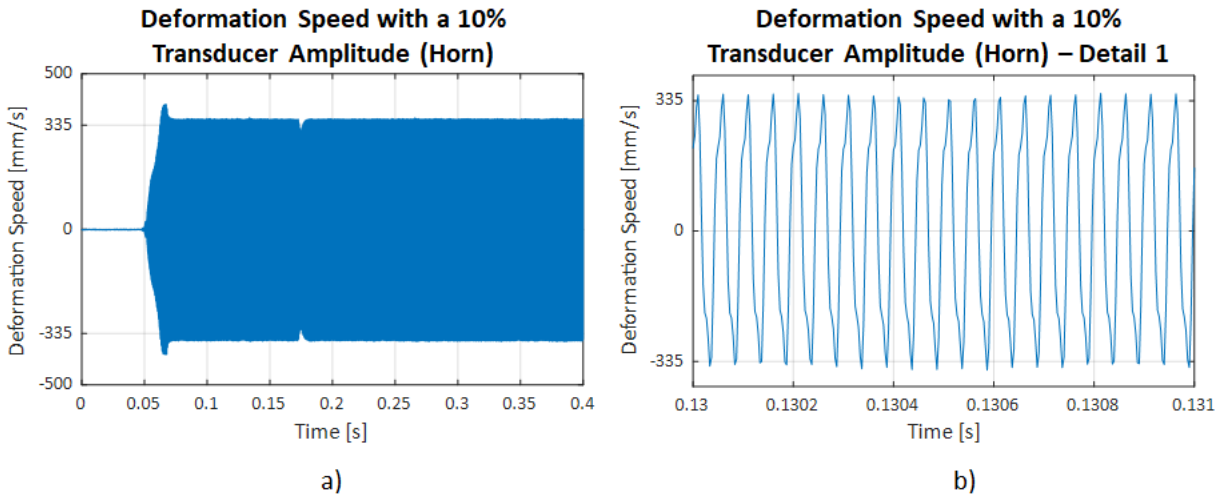

Figure 5.7: Deformation speed fluctuations of the system comprising solely one horn at a 10% transducer amplitude. a) Over the entire test. b) Over a period of 0.001 s.

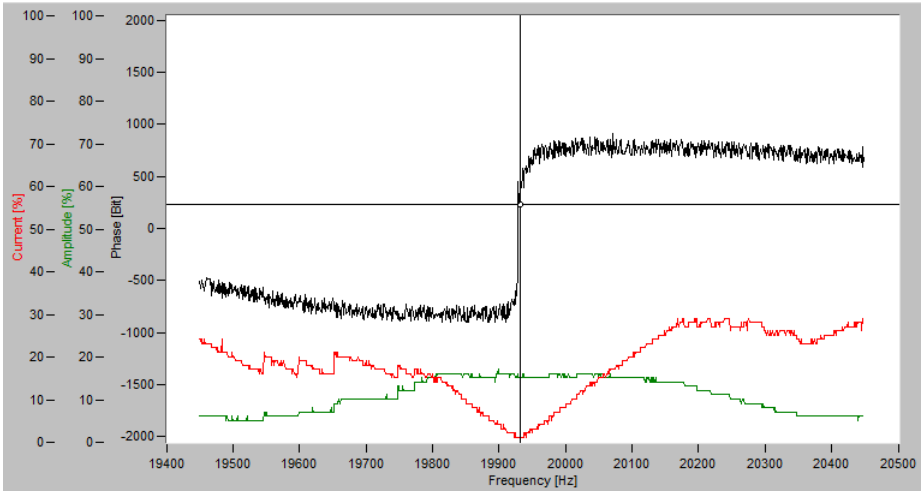

Figure 5.8: Frequency Scan result of the system comprising only one horn. Resonance frequency at 19931 Hz.

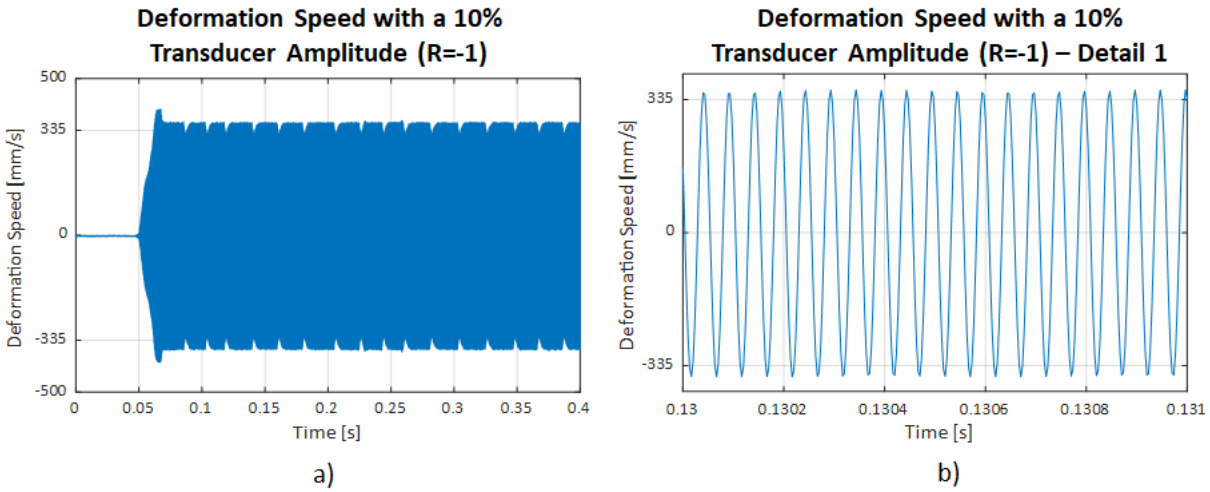

Figure 5.9: Deformation speed fluctuations of the system comprising one horn and the specimen at a 10% transducer amplitude. a) Over the entire test. b) Over a period of 0.001 s.

vibration develops in the specified frequency range. Its frequency corresponds to 19931 Hz, which represents a 127.2 Hz rise compared to the design resonance frequency (19803.8 Hz).

Afterwards, the experiment involving the developed horn and an uniaxial ultrasonic specimen in the R=-1 condition was conducted, as demonstrates proof of concept regarding the horn suitability for the ultrasonic fatigue tests. The same methodology was again employed to assess the deformation speed at the lower end of the specimen of the *horn and specimen* system in the fully reversed condition. Table 5.2 displays the deformation speed measured at the bottom of the ultrasonic system comprising the horn and the specimen. The fact that the aluminium alloy specimen of Figure 4.9b presents one thread on both extremities makes it inadequate for the present proof of concept experiment, therefore it was necessary to resort to other ultrasonic specimen only suitable for ultrasonic fatigue tests with no superimposed mean stress. Thus, for conducting this test an uniaxial hourglass specimen developed at *Laboratório de Ensaios Mecânicos e de Materiais* of Instituto Superior Técnico was used instead.

Figure 5.9a showcases the signal over the entire test of the system comprising the horn and the

specimen, whereas Figure 5.9b provides a view into the pure sinusoidal nature of the wave. Comparing the waves of Figures 5.7b and 5.9b, it is observable that by adding the specimen into the system, the noise of the propagating wave is eliminated. Hence, the wave travelling along the mechanical system assumes a pure harmonic shape. This result may indicate that one possible cause for the presence of the irregularities in the wave shape of horn may be the fact that the Branson piezoelectric transducer is designed to resonate alone at a frequency of approximately 20450/20500 Hz, which means that in the $[19450; 20450]$Hz frequency range the transducer does not exhibit any resonant mode shape. Since the incorporation of the specimen into the system corrects the shape of the propagating wave, therefore one may suspect that introducing the ultrasonic horn alone to the system may not be sufficient to getting the system to work properly, i.e., with an harmonic wave propagating through it.

Table 5.2: Deformation speed of the system comprising one horn and the specimen.

	*P*10[%]	*P*15[%]	*P*20[%]
Threshold [mm/s]	335	490	660
Average [mm/s]	349.4	520.2	697.8

The final stage of the analysis of the system composed by the superior horn and the ultrasonic specimen consisted on the execution of a frequency scan analysis to the same system. The scanning was performed for the same frequency range as the resonant system composed solely by the horn. Figure 5.10 presents the respective frequency scan result, indicating that the single resonant mode that emerges within the specified range of frequencies resonates at 19903 Hz.

Table 5.3: Comparison of the deformation speed of the system comprising solely one horn the system comprising one horn and the specimen.

	*P*10[%]	*P*15[%]	*P*20[%]
Rel. Difference [%]	0.69	0.74	0.97

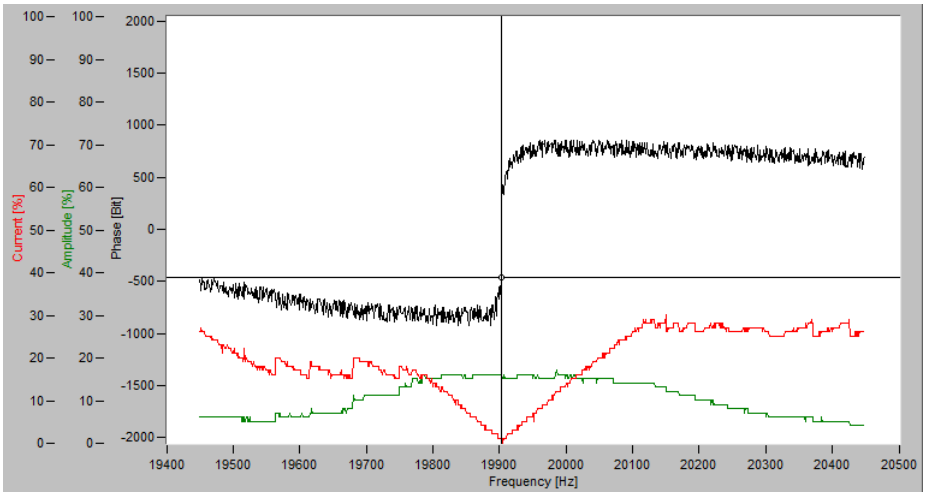

Figure 5.10: Frequency Scan result of the system comprising one horn and the specimen. Resonance frequency at 19903 Hz.

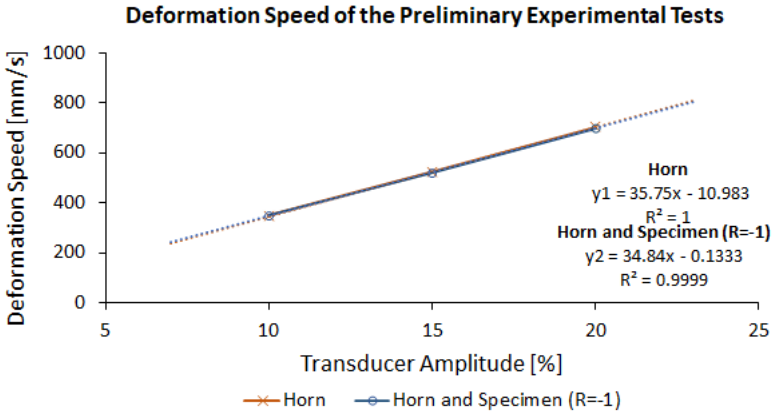

Figure 5.11: Comparison of the deformation speed of the system comprising only one horn and the system comprising one horn and the specimen. Both systems were tested under the unclamped condition.

Table 5.3 displays a negligible difference between the deformation speed of the horn alone and the horn-specimen setup, being 0.69%, 0.74% and 0.97% for 10%, 15% and 20% of the applied transducer amplitude, respectively. Additionally, Figure 5.11 displays the linear relation between the applied transducer amplitude and the deformation speed of both systems, as well as evidences their identical slopes. The slopes relation is of 1.03, demonstrating that the displacement amplitudes for both resonant systems are identical, which means the specimen presents an amplification factor of 1.

5.2.3 Dynamic Testing under the Unclamped Condition

The initial approach to testing the complete mechanical resonant system consisted on inducing a forced vibration with the piezoelectric converter into the unclamped system. The displacement was measured with the laser vibrometer at the lower end of the inferior horn at different transducer amplitudes. The results of the experiments were plotted and are presented on Figure 5.12a, which evidences the expected linear behaviour of the resonant system at the working frequency when subjected to an increasing transducer amplitude.

Additionally, a frequency scan analysis was performed, starting at a frequency of 19450 Hz and stopping at 20450 Hz (with a 1 Hz step), which results are displayed in the graph of Figure 5.12b. By analysing the *current*, *amplitude* and *phase* curves, it is possible to conclude that two vibration modes resonate within the specified frequency range. Their respective resonance frequencies were determined as follows: (i) the frequency ranges in which the *amplitude* is higher than the *current* were identified, and (ii) the *phase* dataset was analysed to identify the frequency values at which the *phase* was at zero degrees. As a result, the frequencies of the first and second mode of vibration emerging in the analysis were identified as 19684 Hz and 19966 Hz, respectively.

Regarding the numerical results, two longitudinal modes are expected in the range $[19450; 20450]$Hz (see Table 4.9), which are the 3^{rd} and 4^{th} longitudinal modes, resonating at 19545.0 Hz and 19808.5 Hz, respectively. When compared with the numerical results, the experimental results present therefore a higher resonance frequency for both modes of vibration: 139 Hz higher for the 3^{rd} longitudinal mode, and 157.5 Hz for 4^{th} longitudinal mode.

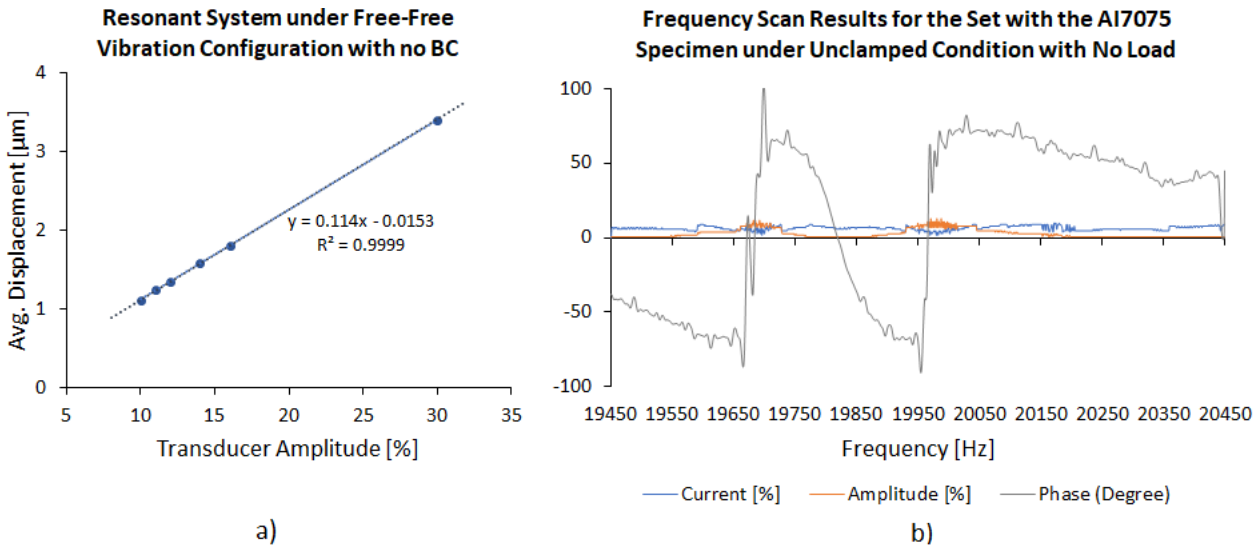

Figure 5.12: Preliminary experimental tests concerning the system comprising the first horn, the specimen, and a second horn under the unclamped condition. a) Evolution of the average displacement, measured at the lower end of the system, with the transducer amplitude. b) Frequency Scan result.

A thermographic camera was used to identify the regions of higher stress along the specimen. The surface of the specimen was painted with a high emissivity black paint so that thermographic imaging could be used to detect temperature changes in the specimen and horn-specimen connections during the dynamic test. The thermal conductivity of the specimen material made it necessary to conduct the test under a 30% transducer amplitude, since for lower powers the temperature fluctuations were not clearly perceptible. The test was conducted under an ambient temperature of 21 ℃ and a relative air humidity of 30.0%.

Figure 5.13 shows the temperature evolution of the specimen during the experiment. Since higher temperatures indicate higher stresses, then one may verify that that the higher stresses develop in the centre of the specimen, where the strain and stress are higher, whereas no significant stresses occur at the horn-specimen connections. The achieved results were as expected.

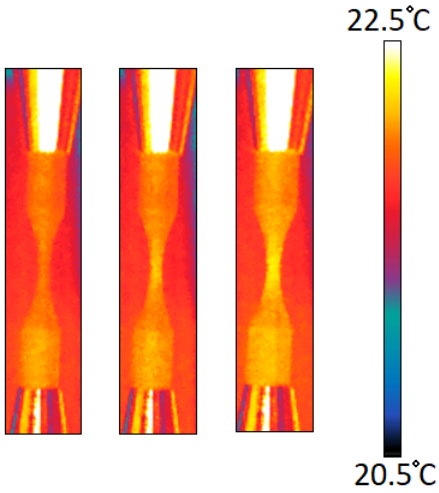

Figure 5.13: Thermographic image of the specimen under tension/compression testing under the unclamped condition.

5.2.4 Dynamic Testing under the Clamped Condition

In order to evaluate the cyclic stress amplitude of the resonant system, a strain gauge was carefully placed in the middle section of the specimen. Due to technical difficulties associated with the laser vibrometer, it was not possible to perform the present experiment (and all the subsequent ones) using this equipment.

Figure 5.14 displays the strain and stress fluctuations in the middle section of the aluminium alloy specimen in the *Clamped Condition* for a transducer amplitude of 10% over the entire testing time. The strain values were obtained straight from the ID 2310 signal amplifier. The Hooke's Law was subsequently applied to obtain the stress values associated with the experimental strain results.

Each test commenced with the resonant system in static equilibrium. Once the piezoelectric transducer started inducing the longitudinal mechanical wave into the superior horn, the system initiated its transient regime. When completely adjusted to the imposed forced vibration, the mechanical system reaches the steady-state regime. Once the piezoelectric transducer ceases inducing the mechanical wave into the superior horn, the system proceeds to vibrate freely. The free vibration response is characterised by successively smaller response amplitudes due to hysteretic damping, until the system reaches its static equilibrium once again.

Figure 5.15 displays the stress fluctuations for a transducer amplitude from 10% to 13% over a time interval of 0.001 seconds so that the stress variations over time could be analysed in further detail. The results for the remaining transducer amplitudes may be consulted in Figure C.2. The time interval of each test was carefully chosen so that only the stationary response was included. It is possible to observe that for every applied transducer amplitude, the stress curve displays a sinusoidal behaviour and zero mean stress.

The tests were conducted under several transducer amplitudes, P[%], which results are listed in Table 5.4. The maximum and minimum stress were registered and the *stress ratio* was determined. The absence of an imposed load is characteristic of the fully reversed condition, meaning the absolute maximum and minimum stresses should be identical, resulting in stress ratios equal to -1. In order to evaluate

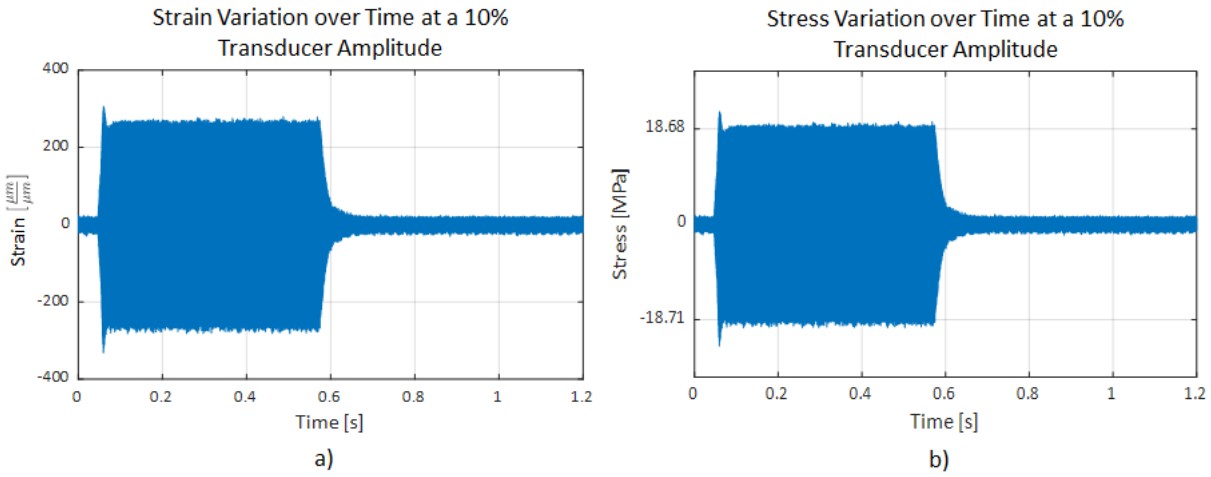

Figure 5.14: Fluctuations of the complete ultrasonic system over time for a 10% transducer amplitude under the clamped condition. a) Strain. b) Stress.

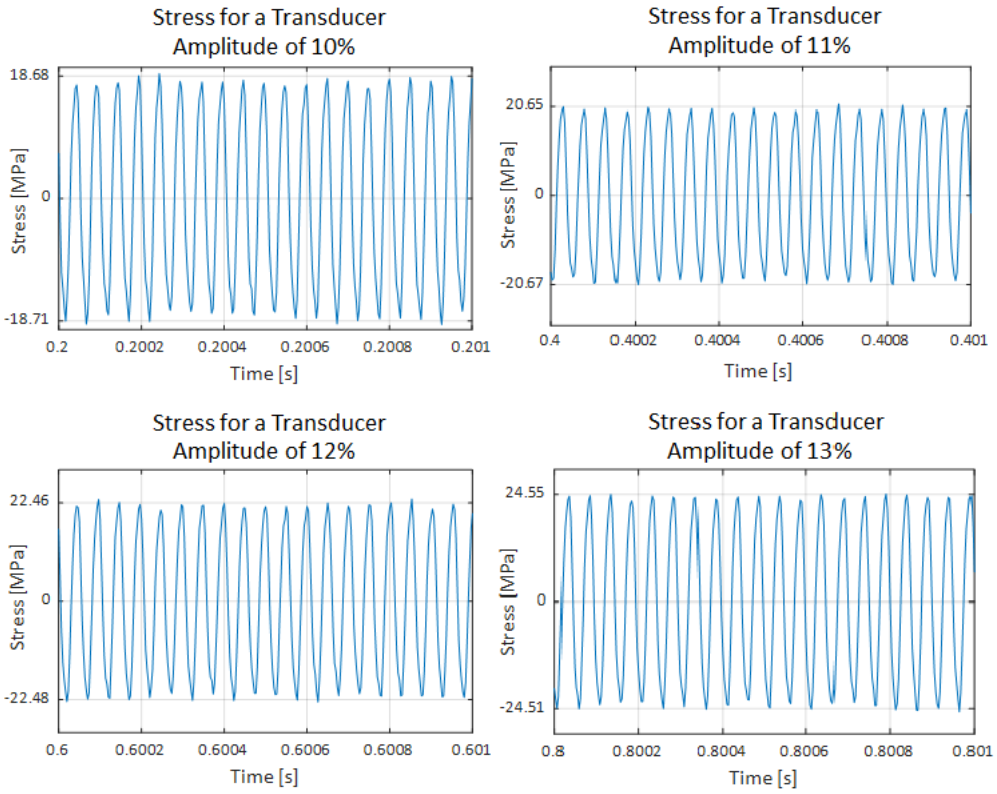

Figure 5.15: Stress fluctuations of the complete ultrasonic system under the clamped condition for a transducer amplitude of 10%, 11%, 12% and 13% over a time interval of 0.001 seconds in the stationary regime.

Table 5.4: Stress parameters at the centre of the aluminium alloy specimen under the clamped condition.

P[%]	σ_{max} [MPa]	σ_{min} [MPa]	*E*[%]	*R*	σ_{avg} [MPa]	σ_{pkpk} [MPa]
10	18.68	-18.71	-0.17	-1.002	18.70	37.39
11	20.65	-20.67	-0.11	-1.001	20.66	41.32
12	22.46	-22.48	-0.09	-1.001	22.47	44.94
13	24.55	-24.51	0.15	-0.998	24.53	49.06
14	26.30	-26.51	-0.77	-1.008	26.41	52.81
15	28.36	-28.41	-0.18	-1.002	28.39	56.77
16	30.29	-30.37	-0.28	-1.003	30.33	60.66
17	32.27	-32.28	-0.02	-1.000	32.28	64.55
18	34.11	-34.38	-0.80	-1.008	34.25	68.49
19	35.97	-35.93	0.09	-0.999	35.95	71.90
20	38.03	-37.94	0.24	-0.998	37.99	75.97
30	57.25	-57.09	0.28	-0.997	57.17	114.34

the equipment calibration, the relative *error* between the absolute maximum (σ_{max}) and minimum (σ_{min}) stresses for each transducer amplitude was determined using equation 5.2. The determined relative *errors* range from 0.02% to 0.80%, indicating a good calibration of the equipment.

$$E[\%] = \frac{|\sigma_{largest}| - |\sigma_{smallest}|}{|\sigma_{largest}|} \times 100 \tag{5.2}$$

To determine the relation between the transducer amplitude employed and the stress amplitude in the middle section of the specimen, the arithmetic average (σ_{avg}) between the absolute maximum (σ_{max})

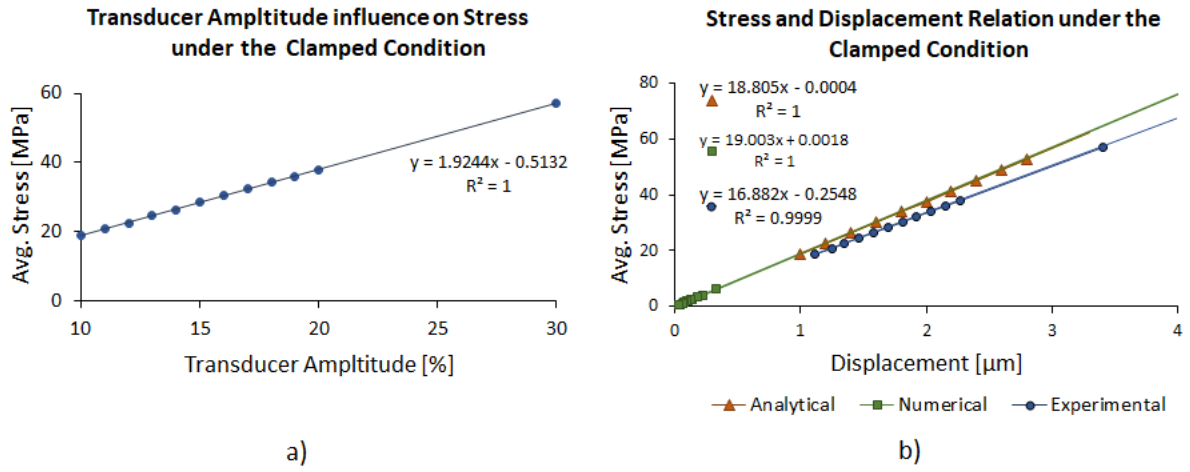

a) b)

Figure 5.16: Complete ultrasonic system under the clamped condition. a) Stress evolution with the transducer amplitude. b) Stress-displacement relations.

and minimum (σ_{min}) stresses was considered. Figure 5.16a shows that σ_{avg} increases linearly with the applied power of the transducer, with a coefficient of determination, R^2, of 1, meaning 100% of the stress changes are explained by the changes in the employed transducer amplitude.

Figure 5.16b shows the linear amplitude response of the stress at the centre of the uniaxial specimen, as the displacement at the bottom of the inferior horn increases. The approaches considered throughout the present work (analytical, numerical, and experimental) may therefore be compared. The analytical solution was obtained resorting to equation 2.19 at $x = 0$, i.e., at the centre of the specimen. The computation of the stress values at $x = 0$ was performed by relating a displacement input value at the free surface of the inferior horn and the displacement of the specimen $A0$. Said relation was attained by means of the horn experimental amplification factor, mathematically translating to $A0 = 2.1 \times A0_c$, being $A0_c$ the displacement input value at the free surface of the inferior horn.

The numerical stress-displacement relation represented in Figure 5.16b was obtained by use of a direct frequency response analysis (SOL 108 Direct Frequency Response), with fixed boundary conditions on both outer rings and no applied static load (*Loading Condition 2)*. However, a 1 N tensile load being exerted on the horn-transducer contact surface to simulate the action of the piezoelectric transducer was defined. The numerical *stress-displacement* relation was computed by plotting the stress results at a surface node in the strain gauge region against the displacement at the central node of the free surface of the inferior horn. The plotted dataset accounts for a set of frequencies ranging from 20180 Hz to 20205 Hz, being the working frequency at 20193.8 Hz (as mentioned in subsection 4.3.3).

Finally, concerning the experimental approach, is it important to note that due to the laser vibrometer technical issues it was impossible to measure the displacement at the bottom of the inferior horn in the present loading condition, which theoretically would make it impossible to relate the displacement amplitude at this location with the stress at the centre of the specimen. To overcome this situation, the displacement results of the unclamped condition were assumed to be similar to the clamped condition for the different transducer amplitudes, as it is not expected that the boundary condition influences significantly the displacement of the resonant system due to being placed in a displacement node. As such,

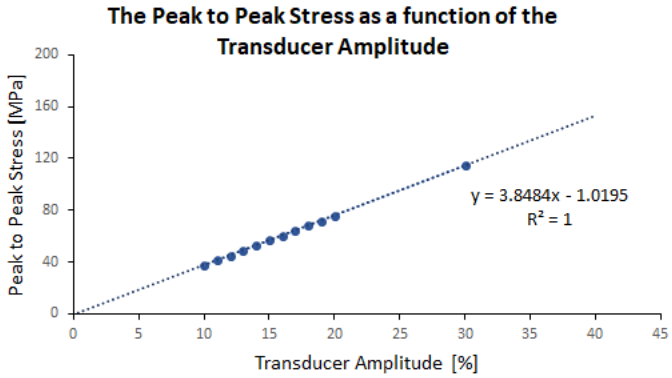

Figure 5.17: Evolution of the peak-to-peak stress with the transducer amplitude for the clamped condition.

the evolution of the displacement amplitude against the applied transducer amplitude for the clamped condition is similar to the one presented on Figure 5.12a. This assumption allowed for estimating the stress at the centre of the specimen for a given displacement amplitude at the lower end of the inferior horn.

The slopes of the linear regression equations of Figure 5.16b indicate the *stress-displacement* relation for the analytical, numerical and experimental procedures. The results show a difference of 1.04% between the analytical and the numerical *stress-displacement* relations. Regarding the experimental *stress-displacement* relation, a difference of 10.23% and 11.16% , respectively, from the analytical and numerical relations have been found.

Additionally, the peak-to-peak stress data (σ_{pkpk}) of Table 5.4 was plotted as a function of the transducer amplitude. The linear regression equation fits the data perfectly, and therefore may be used to determine the peak-to-peak stress as a function of the transducer amplitude and vice versa (figure 5.17).

A frequency scan analysis between a frequency of 19450 Hz and 20450 Hz with a 1 Hz step was also conducted. Figure 5.18 shows the frequency scan results regarding the clamped condition. Similarly to the unclamped, there are two modes of vibration developing within the considered frequency range, however, their respective resonance frequencies rise relatively to the previous condition: the first mode develops at 19701 Hz, and the second mode at 19990 Hz. Comparing quantitatively the frequency scan results for the unclamped and clamped conditions, one may observe that the frequency rises 17 Hz for the first emerging mode of vibration, and 24 Hz for the second mode. This rise is a consequence of the imposition of the boundary conditions, which led to an increase of the stiffness of the ultrasonic set.

According to the numerical results of the clamped condition (see subsection 4.3.3), two modes of vibration are expected in the range $[19450; 20450]$Hz: the 3^{rd} and 4^{th} longitudinal modes, resonating respectively at 19939.3 Hz and 20193.8 Hz. The difference observed between the numerical and experimental resonance frequencies were of (i) 238.3 Hz for the first longitudinal mode, and (ii) 203.8 Hz for the second longitudinal mode. The difference between the numerical and experimental resonance frequencies is due to the fact that the modal analyses consider infinite stiffness in the constrained region, which in reality is impossible to achieve. As such, the stiffness of the resonant system tends to be higher in the modal analysis when compared with the experimental results.

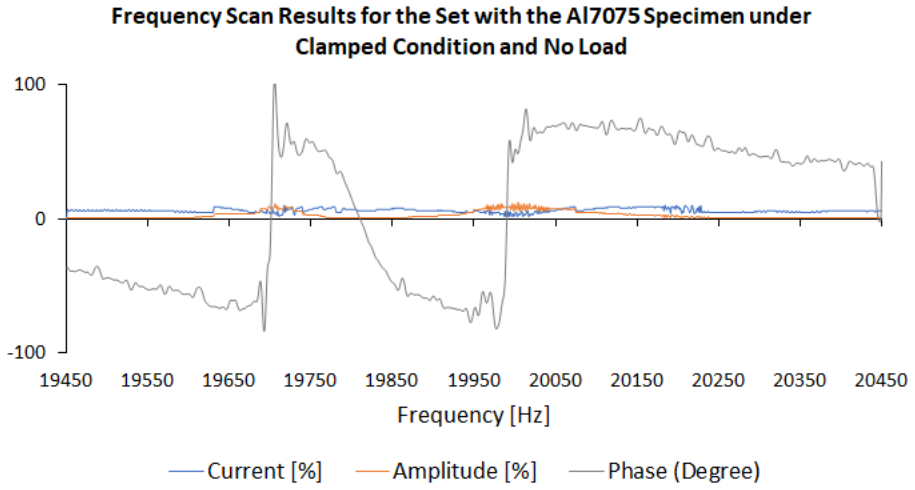

Figure 5.18: Frequency scan results for the clamped condition.

5.3 Ultrasonic System under Static Loading

5.3.1 Stress Evolution Assessing under Static Conditions

A set of static tests, i.e., with no induced vibration, were performed to assess the stress in the centre of the specimen, and its response to the increase of the applied load. The tests were conducted with both outer rings properly clamped. The clamping must be executed carefully, since the resonant system may be put under tension or compression during the process. To avoid damaging the resonant system and/or the load cell by exceeding the specimen yield stress or by reaching the limit of the load cell (10 kN), it is imperative that the load remains within a safe limit. In the particular case of the 7075 aluminium alloy, for a cross section area of $(1.5)^2\pi$ mm^2 , that limit is of 4241.4 N. Nevertheless, ideally the load should always be as close to zero as possible, which implies to be constantly adjusting the crosshead of the electromechanical machine.

The static tests were initiated with a residual load of 45.6 N due to difficulties associated with setting the electromechanical testing machine into perfect equilibrium. The initial residual load does not however impact the strain gauge measurements. The load was then gradually increased and the correspondent strain registered. The static tests results are listed in Table 5.5. The strain results were then transformed into stress values according to equation 5.3.

$$\sigma[MPa] = E[MPa] \times \varepsilon \times 10^{-6}[m/m] \tag{5.3}$$

Figures 5.19a and 5.19b display, respectively, the evolution of the measured strain and stress as the load increases. As expected, both strain and stress response to the increase of the applied static load describe a linear response with a coefficient of determination of 0.999.

After applying the successive static loads listed on Table 5.5, the initial residual load was reapplied, producing a strain of 15 $\mu m/\mu m$. Therefore the procedure led to an accumulated error of 15 $\mu m/\mu m$, which is inferior to the characteristic signal fluctuations of the ID 2310 signal amplifier ($\pm$25 $\mu m/\mu m$), meaning the accumulated error may be neglected.

Table 5.5: Strain and stress values at the centre of the specimen for different applied static loads under the static condition.

Load [N]	Strain [$\mu m/\mu m$]	Stress [MPa]
45.6	0	0.0
162.4	225	16.2
216.5	335	24.1
338.7	605	43.6
471.0	865	62.3
595.6	1090	78.5
708.0	1310	94.3
819.0	1515	109.1
945.7	1730	124.6

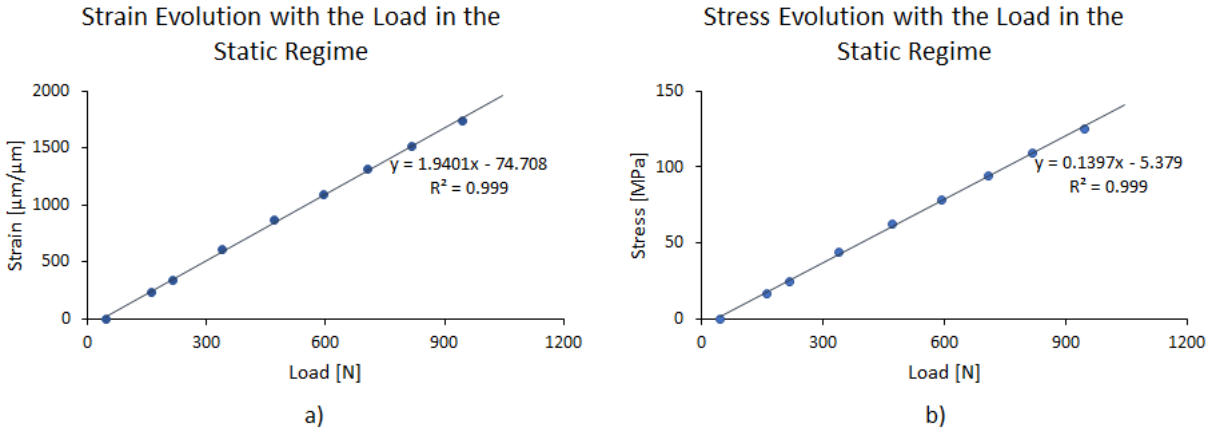

Figure 5.19: Strain and stress evolution with the imposition of an increasing static load under the static regime. a) Strain evolution. b) Stress evolution.

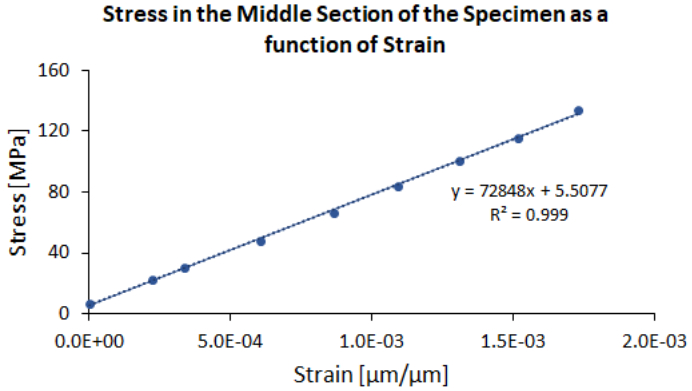

Figure 5.20: Assessment of the Modulus of Elasticity based on the experimental results obtained from the tests conducted under static conditions.

Finally, the Modulus of Elasticity of the aluminium alloy specimen was determined by plotting the *strain* data of Table 5.5 against the *load* data divided by the area of the middle section of the specimen ($\pi 1.5^2$), and is displayed in Figure 5.20. The slope of the plotted line represents the Modulus of Elasticity of the material (72848 MPa). This result is consistent with the Modulus of Elasticity provided by the manufacturer. The relative error between the theoretical and experimental Modulus of Elasticity is of 1.16%.

5.3.2 Dynamic Response under Static Loading

Concerning safety reasons, the first dynamic test with a superimposed mean stress was conducted with a relatively low static load of 193 N (see Figure 5.21). A comparison between the peak-to-peak amplitudes at a 20% transducer amplitude in the clamped condition (Table 5.4) and in the *clamped condition with a static load of 193 N* (Table 5.6), was carried out, and a difference of 0.72% was found. The similarity of both conditions indicates that the only parameter that varies with the applied static load is the mean stress of the propagating mechanical wave, and consequently the associated stress ratio. The static and dynamic regimes are therefore independent from one another.

Table 5.6: Stress parameters at the centre of the specimen for an applied tensile static load of 193 N under dynamic conditions.

P[%]	σ_{max} [MPa]	σ_{min} [MPa]	R	σ_{mean} [MPa]	σ_{pkpk} [MPa]
20	61.60	-13.82	-0.224	23.89	75.42

Afterwards, a frequency scan analysis with a static load of 1000 N applied on the resonant system was carried out. The analysis was conducted between a frequency of 19450 Hz and 20450 Hz with a 1 Hz step. The frequency scan results provided by the transducer controller are displayed in Figure 5.22. Similarly to the clamped condition (see Figure 5.18), there are two modes of vibration developing within the considered frequency range. The first mode of vibration develops at 19626 Hz, and the second mode at 19984 Hz. Comparing these results with the ones for the clamped condition, one may notice a drop of frequency of 75 Hz for the first developing mode, and 6 Hz for the second mode (the working mode). The 6 Hz frequency difference in the working resonant mode represents a negligible 0.03% decrease. This means that the imposed static load does not influence the dynamic behaviour of the resonant system, hence corroborating the conclusion presented in the current subsection that ”the static and dynamic regimes are independent from one another”.

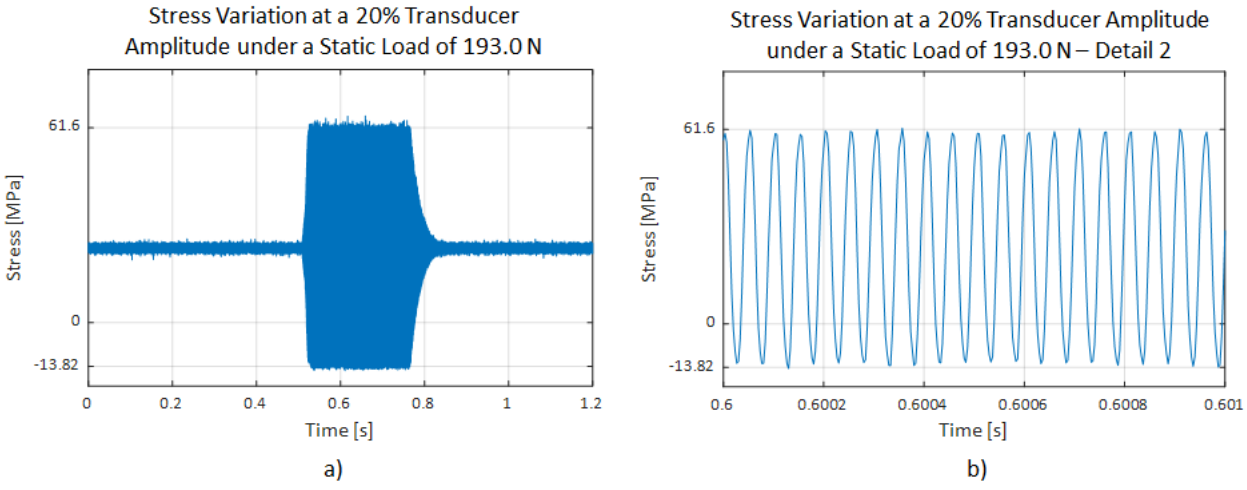

Figure 5.21: Stress fluctuation at the centre of the specimen measured with the strain gauge for an applied static load of 193 N and a 20% transducer amplitude. a) Over the entire test. b) Over a period of 0.001 s.

Furthermore, it is pertinent to associate the mean stress and stress ratio to a particular applied static load at a given transducer amplitude. In that regard, the line *Mean Stress* of the graph of Figure 5.23 was obtained considering the following statements: (i) a null static load produces a null mean stress, (ii) a 193 N static load at a 20% transducer amplitude produces a 23.89 MPa mean stress, and (iii) being the tests conducted in the elastic regime, a linear behaviour and hence evolution of the mean stress as the applied load rises is expected.

Based on the linear regression equation regarding the *Mean Stress* parameter, it was possible to estimate the mean stress value for further static loads. These results, combined with the fact that the peak-to-peak amplitude of the propagating wave remains independent from the static load, allowed the estimation of the maximum and minimum stresses. These results are listed in Table 5.7 and also plotted in Figure 5.23. Ultimately, the stress ratio for each distinct load was computed, being the results listed on Table 5.7. Additionally, equation 5.4 allows to compute both the maximum and minimum stress as a function of the mean and peak-to-peak stresses. When put into equation 2.23, one may establish a correlation between the mean and peak to peak stresses, and also the stress ratio (see equation 5.5).

Table 5.7: Expected stress parameters for different values of the applied static load for a 20% transducer amplitude.

Load[N]	σ_{mean} [MPa]	σ_{pkpk} [MPa]	σ_{max} [MPa]	σ_{min} [MPa]	*R*
0	0	75.97	38.03	-37.94	-1
54	6.69	75.42	44.40	-31.02	-0.7
102	12.63	75.42	50.34	-25.08	-0.5
250	30.95	75.42	68.66	-6.76	-0.1
307	37.98	75.42	75.69	0.27184	0
375	46.43	75.42	84.14	8.72	0.1
920	113.90	75.42	151.61	76.19	0.5
1739	215.23	75.42	253.0	177.58	0.7

$$\sigma_{max/min} = \sigma_{mean} \pm \frac{\sigma_{pkpk}}{2} \tag{5.4}$$

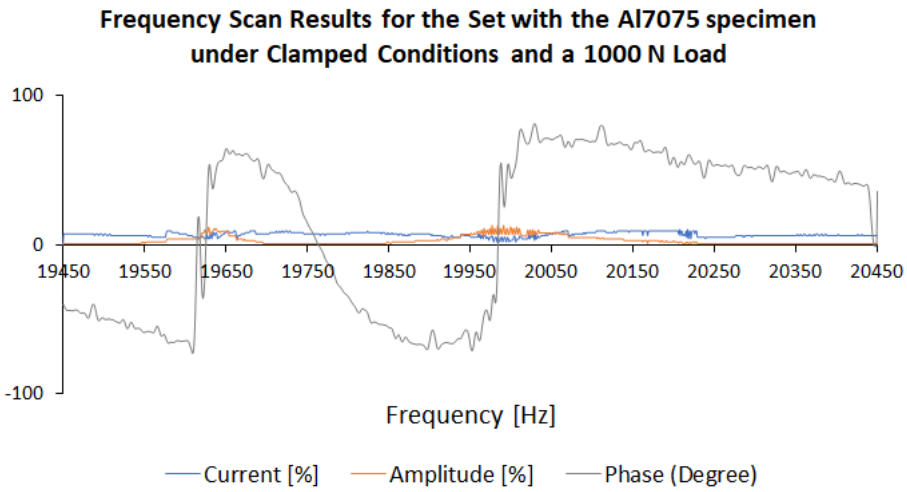

Figure 5.22: Frequency scan results for the clamped condition with an 1000 N applied static load.

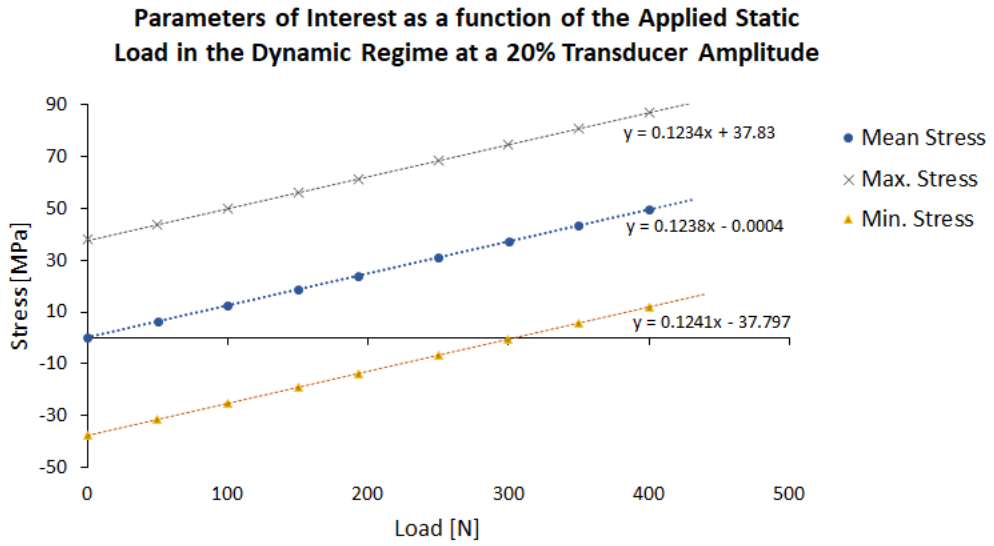

Figure 5.23: Evolution of the stress parameters (mean stress, maximum stress and minimum stress) as the applied static load increases.

$$\sigma_{mean} = \frac{\sigma_{pkpk}}{2}\left(\frac{-1-R}{R-1}\right) \tag{5.5}$$

5.4 Ultrasonic Fatigue Tests

With the proven resonant behaviour of the system and the induction of the desired stress state a ultrasonic mean stress experimental methodology was drawn. The developed methodology sequence for establishing the desired ultrasonic conditions for conducting ultrasonic fatigue tests with a superimposed mean stress is as follows:

1. Define R;
2. Conduct a dynamic test under the clamped condition as described in section 5.2.4 to obtain σ_{pkpk} parameter as a function of P(%) (see Figure 5.17);
3. Define P(%) and use the computed linear regression equation found on step 2 to determine σ_{pkpk}, or vice versa;
4. Determine σ_{mean} by substituting R and σ_{pkpk} in equation 5.5, which is showcased below:

$$\sigma_{mean} = \frac{\sigma_{pkpk}}{2}\left(\frac{-1-R}{R-1}\right)$$

5. Compute the *Load* (Figure 5.23) using the linear regression equation *mean stress* from the graph of Figure 5.23, where x represents the load, in N, and y the mean stress, in MPa. The steps for obtaining said equation are the following:
   (a) Conduct a static experimental test with a stipulated superimposed static load as described in subsection 5.3.2 to determine the σ_{mean} produced by the applied static load.

(b) Consider the aforementioned statements of subsection 5.3.2: (i) a null static load produces a null mean stress, (ii) a given static load at an established transducer amplitude produces a mean stress at the centre of the specimen, and (iii) being the tests conducted in the elastic regime, a linear behaviour and evolution of the mean stress as the applied load rises is expected;

(c) Determine the *mean stress* equation as a function of the *Load* by defining a straight line between the (0,0) and the (applied static load, measured σ_{mean}) points (see Figure 5.23). The equation that characterises said straight line allows for determining the *Load* (Figure 5.23) needed to produce the desired mean stress determined on step 4.

6. Establish a method within the control software of the electromechanical machine for applying and controlling the static load:

   (a) define a load variation parameter that, when detected, leads to the control system to immediately stop applying the load or performing the dynamic test (for the conducted tests, that parameter was defined as $\Delta F = 100$ N);

   (b) define the rate at which the static load will be applied (for the conducted tests, that parameter was initially defined as 0.1 kN/min, and was then increased to 0.2 kN/min);

   (c) define the *start of hold value* parameter, in kN , at which the machine will stabilise the applied static load (for the conducted tests, that parameter was defined as the required static load for each test).

7. Once the static load has stabilised, the ultrasonic fatigue test may be initiated.

5.4.1 Specimen 1

The established conditions for the first fatigue experiment were the following: (i) R=0.5, (ii) P=60%, that corresponds to $\sigma_{pkpk} = 230$ MPa, which in turn represents approximately 0.38% of the yield stress, (iii) $\sigma_{mean} = 345$ MPa, (iv) $F = 2.79$ kN.

The experimental procedure started with the imposition of a preload of 474 N and the subsequent increasing of the load at a rate of 0.1 kN/min until reaching the hold value of 2.79 kN. Figure 5.24 shows

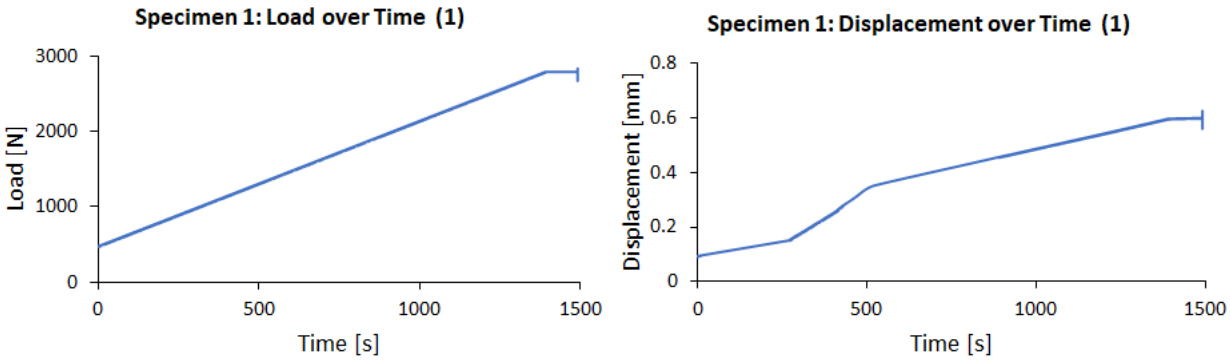

Figure 5.24: Load and displacement evolution regarding specimen 1 - first attempt.

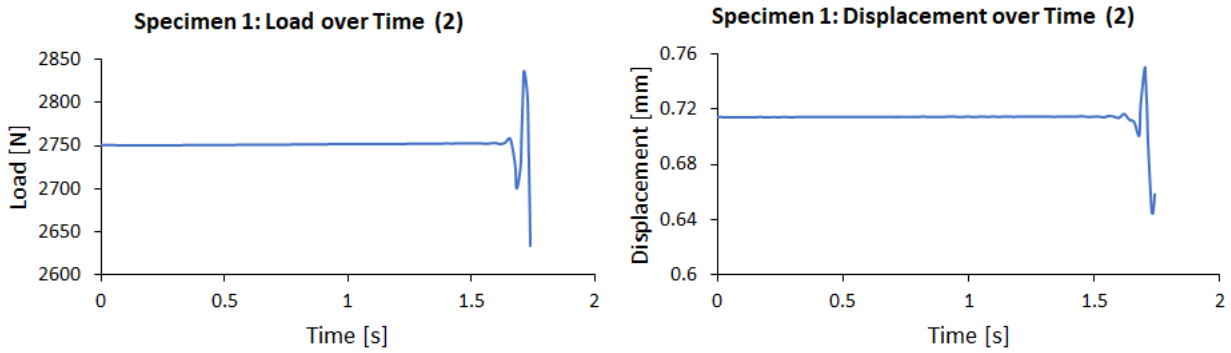

Figure 5.25: Load and displacement evolution regarding specimen 1 - second attempt.

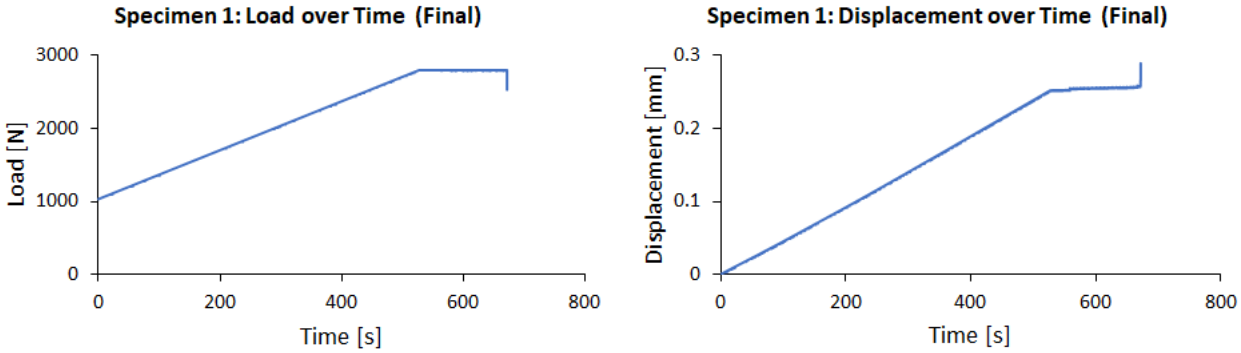

Figure 5.26: Load and displacement evolution regarding specimen 1 - final attempt.

the load and displacement evolution over time. The displacement curve exhibits a non-linear behaviour of the machine at the beginning of the attempt, indicating the existence of displacements besides the elastic deformation of the ultrasonic system and correspondent supporting structure. These displacements were attributed to dislocations on the structure. When the dynamic test started, the system vibrated producing a low-pitched sound, evidencing that there were elements vibrating a low frequency. The only possible elements that could vibrate at such frequencies were the structural elements of the machine, so the low-pitched sound suggested that the structure needed to be tighten further. The test was hence interrupted.

Then, the structure was further tighten to mitigate the effect of the slacks on the machine, and a preload of 2.75 kN was applied. Having eliminated some of the slacks, a new problem appeared: it was not possible to apply the required load, since the procedure was immediately interrupted by the control system of the machine that detected a change in the load of more than 100 N (see Figure 5.25). Several attempts to apply the static load were made without success.

The cause of the interruption was thought to be resistance that the guide rods may be applying upon the machine when the crosshead attempted to rise. On this account, it was decided to remove the guide rods from the structure and conduct other test to comprehend if these elements were in fact interfering with the test. This decision was nonetheless made considering the risk of causing misalignment of the ultrasonic assembly, and consequently the imposition bending stresses on the specimen.

Before applying the load, the entire structure was further tightened and the guide rods were subsequently removed. Figure 5.26 shows not only the linear behaviour of the machine from the start of

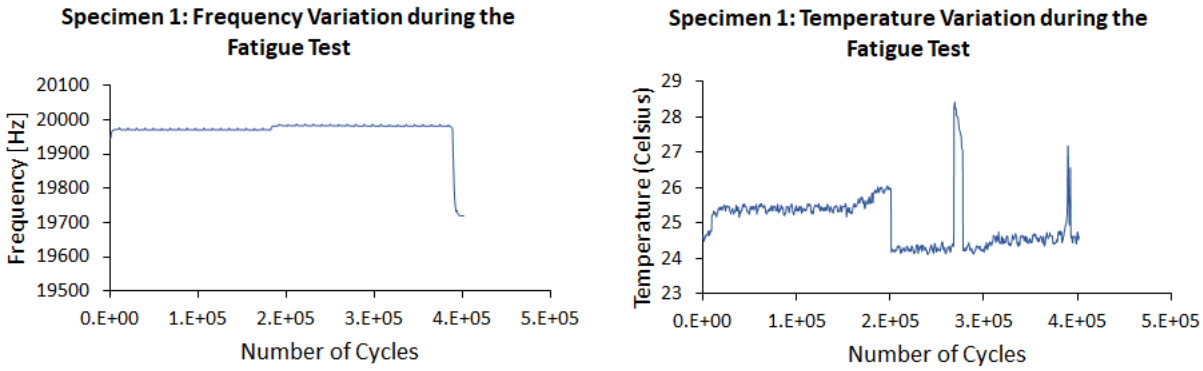

Figure 5.27: Frequency and temperature fluctuations from the beginning of the fatigue test until total rupture of specimen 1.

the procedure, but also an inferior displacement of the machine at 2.79 kN than the one of Figure 5.24, proving the non-linear behaviour of the latter was in fact a consequence of existent slacks. These results evidence the need of ensuring that the structure is adequately tighten before starting any experimental procedure. It is also important to highlight the fact the removal of the guide rods allowed the imposition of the static load to occur without any impediments, suggesting that the guide rods were the structural elements responsible for the difficulties regarding the imposition of the static load.

Once the necessary conditions were reached, the fatigue test was started and the static load was kept constant throughout the experiment. The displacement curve of Figure 5.26 presents a slight displacement variation at the beginning of the fatigue test. These displacement variations may be due to persistent slacks. They are, however, inappreciable. The fatigue test terminated with the total rupture of the specimen, being that moment characterised by an abrupt decrease of the load and rise of the displacement of the machine.

Figure 5.27 displays the frequency and temperature fluctuations during the fatigue test. It was not possible to achieve the gigacycle regime since total rupture occurred at 4×10^5 cycles. This event is clearly depicted on both plots: an abrupt decrease of the frequency and a temperature peak occur simultaneously.

As mentioned before, difficulties associated with applying the static load led to the decision of removing the guide rods, resulting in an increase of approximately 10 Hz in the frequency occurring at approximately 1.8×10^5 cycles. The FEA results indicate the existence of a bending mode at 21047 Hz, which could be having a greater influence on the longitudinal mode due to the bending stresses the specimen is under as a result of the guide rods being removed. Concerning the temperature variations throughout the fatigue test, there are two moments that should be addressed: there is a sudden temperature drop at approximately 2×10^5, and a temperature rise at 2.7×10^5 cycles. The temperature drop is related with a change in the room temperature probably caused by air conditioning. On the contrary, the abrupt and brief temperature rise is probably just a result of a reading error of the pyrometer as it is not reflected on the frequency of the system, meaning it cannot be associated with crack initiation nor propagation.

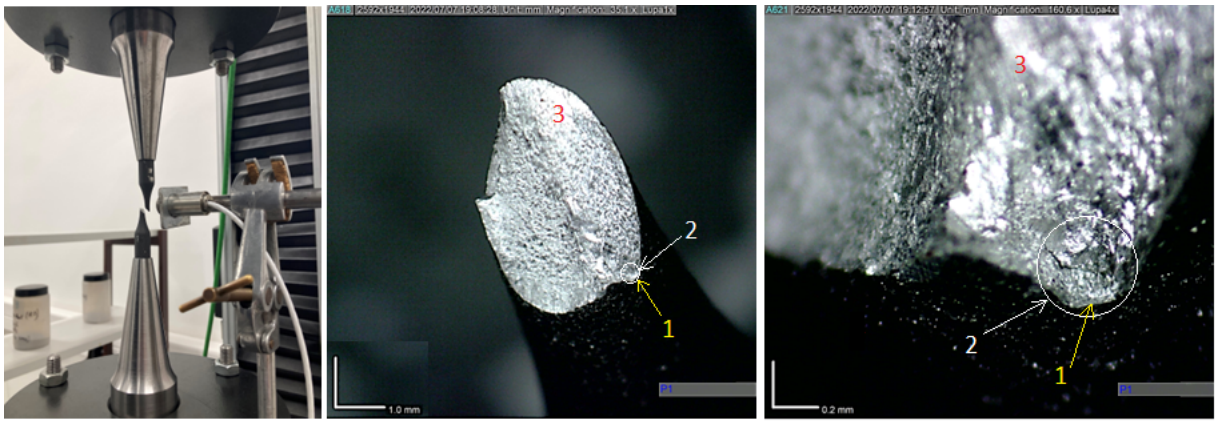

Figure 5.28: Total rupture of specimen 1. Area identification: 1, crack initiation site; 2, crack propagation area; 3, total rupture area.

Figure 5.28a shows the fractured specimen immediately after total rupture. It is clear that the upper and lower halves of the specimen are misaligned, indicating that bending stresses were being applied on the specimen during the fatigue test as a result of removing the guide rods. Mayer (1999) suggested that if perfect alignment could not be guaranteed, the fractured specimen would present an inclined crack front due to the influence of the undesirable superimposed bending loads, which has in fact occurred with specimen 1 (see Figures 5.28a and 5.28b). The fracture surface of specimen 1 is shown in Figures 5.28b and 5.28c. The crack initiated at the surface, which is typical of aluminium alloys (Lesperance et al., 2021), however the crack propagation area represents a small fraction of the surface. Despite not resembling a typical tension-compression fracture surface in all its extension due to the influence of the bending stresses, the fracture surface presents proof that the crack initiation was fatigue related.

5.4.2 Specimen 2

The established conditions for the first fatigue experiment were the following: (i) R=0.5, (ii) P=52% that corresponds to $\sigma_{pkpk} = 199.2$ MPa, which in turn represents approximately 0.33% of the yield stress, (iii) $\sigma_{mean} = 298.8$ MPa, (iv) $F = 2.40$ kN. The guide rods were lubricated in an effort to reduce the resistance they were applying upon the electromechanical machine.

The first attempt to apply the static load resulted in an occurrence similar as the one illustrated in Figure 5.25. It was then decided to reapply the load with the blower and engine fan off. By doing so, it was possible to gradually increase the static load until reaching the defined *start of hold value* (see Figure 5.29). However, when the fatigue test started, it was immediately interrupted by the control system.

The only remaining factor that could be affecting the dynamic tests was the presence of the guide rods. It was hence decided to perform a dynamic test with one of the guide rods at a time, which resulted in the control system (and consequently the electromechanical machine) instantly interrupting the dynamic test once again. On that account, it was determined that given the present circumstance, the only way to proceed with the fatigue test was by removing the primary alignment elements, i.e., the

guide rods, despite the presence of bending stresses on the specimen. The load was reapplied under the described conditions, and the fatigue test was conducted. The load and displacement evolution over time are displayed in Figure 5.30. As can be observed, the displacement curve presents a tendency of increasing over time during the fatigue test, which is explained by the specimen temperature rise and the fact that the test was conducted in a hot day (over 30° C), reducing the Young's Modulus of the materials and consequently making the ultrasonic set more susceptible to deform. To confirm that the room temperature was indeed affecting the test, the air conditioner was turned on and a stabilisation of the displacement was observed (approximately from second 2250 until rupture time).

Figure 5.31 shows the frequency and temperature fluctuations during the fatigue test. The total fracture of the specimen occurred at 5.5×10^6 cycles. A frequency decrease from 20014 Hz to 20003 Hz

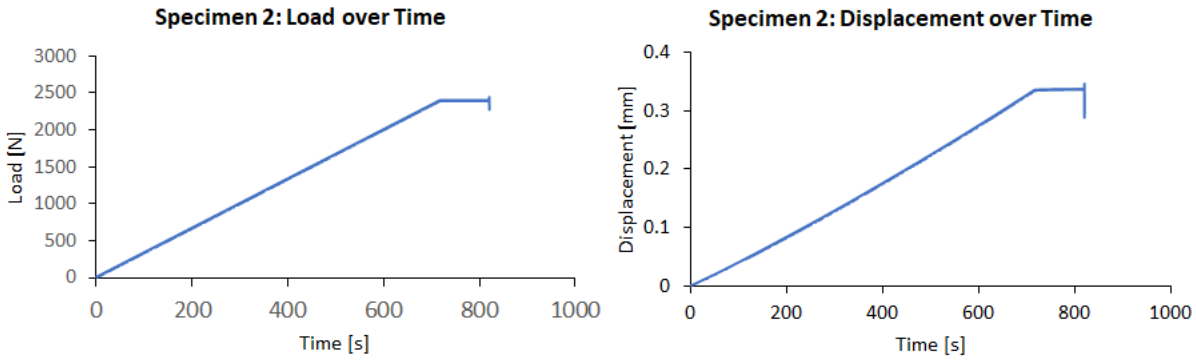

Figure 5.29: Load and displacement evolution regarding specimen 2 - first attempt.

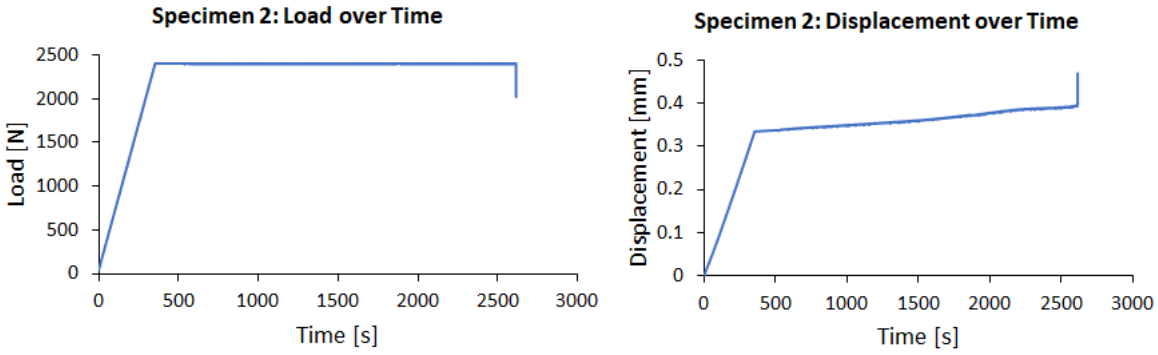

Figure 5.30: Load and displacement evolution regarding specimen 2 - final attempt.

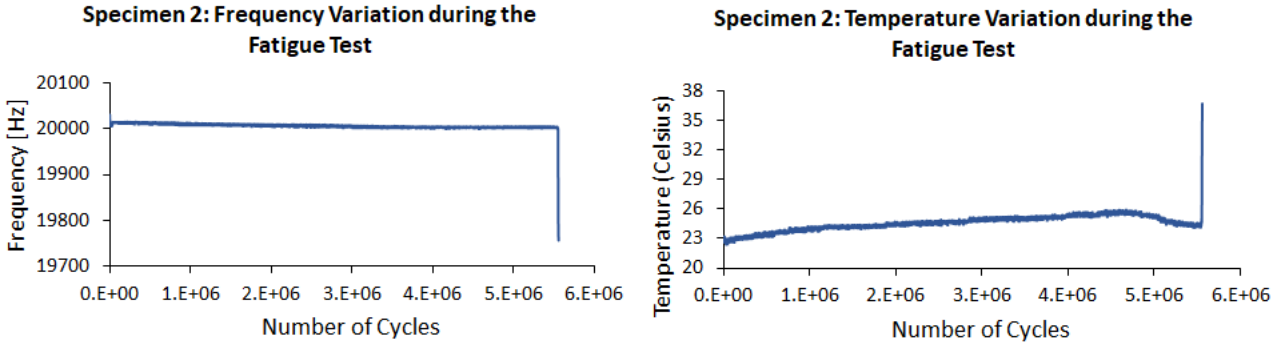

Figure 5.31: Frequency and temperature fluctuations from the beginning of the fatigue test until total rupture of specimen 2.

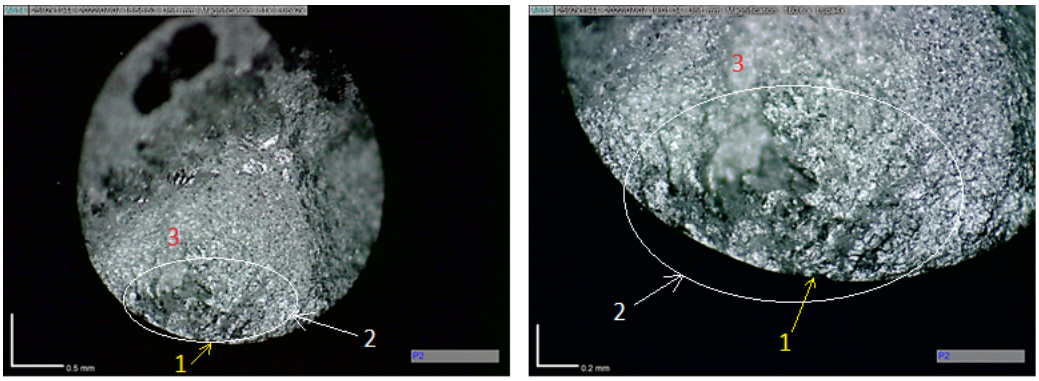

Figure 5.32: Total rupture of specimen 2. Area identification: 1, crack initiation site; 2, crack propagation area; 3, total rupture area.

was observed throughout the fatigue test due to the temperature rise, which in turn was a consequence of the fatigue test itself. However, from approximately 5×10^6 cycles until total failure, a temperature drop was registered due to the air conditioning activation.

Figures 5.32a and 5.32b show the fracture surface of specimen 2. The crack initiation site is located at the surface of specimen 2, and the fracture surface presents a more widespread propagation area than the one of specimen 1, exhibiting a radial ridge pattern similar to the one presented on Sakai et al. (2006) concerning a high carbon chromium bearing steel under axial loading for different stress ratios.

The overall fracture surface of Specimen 2 is considerably different from Specimen 1. The propagation surface is orthogonal to the applied stress, while specimen 1 shows a crack propagation angle. The fracture surface of Specimen 2 is more coherent with the predicted behaviour for mean stress tension-compression ultrasonic fatigue. This change in behaviour is a consequence of the improvements employed on the experiment conducted on Specimen 2, in which the number of loading and unloading operations regarding the imposition of the static load on the specimen before conducting the ultrasonic fatigue test was reduced in comparison to the experiment conducted on Specimen 1.

Chapter 6

Conclusions and Future Work

With the increasingly larger demand for mechanical components that should withstand a very high number of loading cycles, the ability to reliably and efficiently evaluate their life is crucial to prevent catastrophic failure. Traditionally, the methods used to predict the life of such components relied on statistical analyses. Given that statistical methods are not always able to accurately predict fatigue failure in the very high cycle fatigue regime, the gigacycle fatigue testing field has been under great attention by the scientific community (Bathias, 1999).

This dissertation further expanded the available literature by contributing with the design, manufacture and evaluation of both an ultrasonic system for specimen high frequency testing, and a support structure, which allows the imposition of an applied static load. Both the ultrasonic system and the support structure were assembled into an electromechanical machine to evaluate the behaviour of specimens in the very high cycle fatigue regime. The mechanical behaviour of the ultrasonic system was evaluated analytically, using the equations of the available literature, numerically, resorting to FEA software, and experimentally.

The obtained experimental results show that the developed structure and ultrasonic system allow for the specimens' fatigue testing in the ultrasonic regime with a superimposed mean stress. With the required stress state and at approximately 20 kHz, the results also demonstrate that the dynamic behaviour of the ultrasonic system is not affected by the imposition of a static load, as the only parameter varying with the static load is the mean stress and, consequently, the stress ratio. Additionally, the frequency scan results of the conducted analyses for the clamped condition both with and without static load proved that the frequency of the working mode remains undisturbed when a static load is added to the system. This means that the system may be initially studied as if it was under the fully reversed condition.

The first attempts to perform the ultrasonic fatigue experiments revealed that the guide rods were interfering with the tests, and consequently had to be removed. The removal of the guide rods led to the loss of alignment of the ultrasonic system, causing the development of undesired bending stresses. It was possible to conduct the fatigue tests and observe total rupture of both tested specimens, and also to identify the crack initiation site, the crack propagation area and the total rupture area in both speci-

mens, despite them presenting noticeably different fracture surfaces caused by the presence of bending stresses and the improvements employed on the experiment conducted on Specimen 2. Specimen 1 failed at 4×10^5 cycles, and Specimen 2 at 5.5×10^6 cycles. It was also observed that the cooling devices in direct contact with the structure and/or electromechanical machine induce vibration onto the structure and therefore preclude the fatigue tests from being conducted. In the light of that event, one should only resort to cooling devices external to the structure and/or electromechanical machine.

The results also show that the stress-displacement relations obtained via the analytical and numerical procedures exhibit a negligible difference, with both procedures leading to a difference of approximately 10% between the respective stress-displacement relations and the experimental stress-displacement relation. This means one may resort to the analytical method to estimate the dynamic behaviour of the ultrasonic system (namely the stress-displacement relation) hence eliminating the need for performing extensive and time consuming numerical analyses in an FEA software. Furthermore, the stress-displacement relation allows for estimating the mean stress at the centre of the specimen, based on the displacement measured with a laser vibrometer at the lower end of the ultrasonic system.

To conclude, the obtained results strongly showcase that the developed resonant system and support structure allow to experimentally conduct ultrasonic fatigue tests with a superimposed mean stress, without the need to perform time consuming numerical analyses in order to determine the stress-displacement relation.

Given that during the experimental evaluation the guide rods had to be removed in order for them not to interfere with the trials, a next logical line of work would be to design and evaluate a new alignment system, for example, with shortened guide rods for the inferior cage. Such approach would reduce the propagation of the deviation in the ultrasonic system, caused by the misalignment of the cages. The resulting system may then be evaluated using the same methods presented in this dissertation.

Another possible topic of work would be to adapt the developed structure and system to conduct ultrasonic fatigue tests under bending conditions. The inferior cage developed and presented in this dissertation would have to be discarded, while the superior cage could be reused. Depending on the nature of the experiment (three-point bending or biaxial bending), it would be necessary to design and manufacture a specimen with the required geometry and the respective support system. Also, an hemispherical indenter would have to be added to the resonant system.

Bibliography

Bathias, C. (1999). There is no infinite fatigue life in metallic materials. *Fatigue & fracture of engineering materials & structures (Print)*, 22(7):559–565.

Bathias, C. (2006). Piezoelectric fatigue testing machines and devices. *International Journal of Fatigue*, 28(11):1438–1445.

Bathias, C. and Paris, P. (2005). *Gigacycle Fatigue in Mechanical Practice*. Marcel Dekker.

Brugger, C., Palin-Luc, T., Osmond, P., and Blanc, M. (2016). Gigacycle fatigue behavior of a cast aluminum alloy under biaxial bending: experiments with a new piezoelectric fatigue testing device. *Procedia Structural Integrity*, 2:1173–1180.

Costa, P. R., Montalvão, D., Freitas, M., Baxter, R., and Reis, L. (2019). Cruciform specimens' experimental analysis in ultrasonic fatigue testing. *Fatigue & Fracture of Engineering Materials & Structures*, 42(11):2496–2508.

de Moura Branco, C. A. (1998). *Mecânica dos materiais*.

Eisner, E. (1963). Design of sonic amplitude transformers for high magnification. *The Journal of the Acoustical Society of America*, 35(9):1367–1377.

Freitas, M., Anes, V., Montalvao, D., Reis, L., and Ribeiro, A. (2011). Design and assembly of an ultrasonic fatigue testing machine. *Anales de Mecânica de la Fractura*.

Furuya, Y. (2008). Specimen size effects on gigacycle fatigue properties of high-strength steel under ultrasonic fatigue testing. *Scripta Materialia*, 58(11):1014–1017.

Furuya, Y. and Takeuchi, E. (2014). Gigacycle fatigue properties of ti–6al–4v alloy under tensile mean stress. *Materials Science and Engineering: A*, 598:135–140.

Gielen, D., Boshell, F., Saygin, D., Bazilian, M. D., Wagner, N., and Gorini, R. (2019). The role of renewable energy in the global energy transformation. *Energy Strategy Reviews*, 24:38–50.

Halliday, D., Resnick, R., and Walker, J. (2013). *Fundamentals of physics*. John Wiley & Sons.

Huang, Z. Y., Liu, H. Q., Wang, H. M., Wagner, D., Khan, M. K., and Wang, Q. Y. (2016). Effect of stress ratio on vhcf behavior for a compressor blade titanium alloy. *International Journal of Fatigue*, 93:232–237.

Kovacs, S., Beck, T., and Singheiser, L. (2013). Influence of mean stresses on fatigue life and damage of a turbine blade steel in the vhcf-regime. *International Journal of Fatigue*, 49:90–99.

Lage, Y., Freitas, M., Montalvao, D., Ribeiro, A., and Reis, L. (2012). Ultrasonic fatigue analysis on steel specimen with temperature control: Evaluation of variable temperature effect.

Lesperance, X., Ilie, P., and Ince, A. (2021). Very high cycle fatigue characterization of additively manufactured alsi10mg and alsi7mg aluminium alloys based on ultrasonic fatigue testing. *Fatigue & Fracture of Engineering Materials & Structures*, 44(3):876–884.

Mahfuz, H., Maniruzzaman, M., Krishnagopalan, J., Haque, A., Ismail, M., and Jeelani, S, a. (1995). Effects of stress ratio on fatigue life of carbon-carbon composites. *Theoretical and applied fracture mechanics*, 24(1):21–31.

Marines, I., Bin, X., and Bathias, C. (2003). An understanding of very high cycle fatigue of metals. *International Journal of fatigue*, 25(9-11):1101–1107.

Marines-Garcia, I., Doucet, J.-P., and Bathias, C. (2007). Development of a new device to perform torsional ultrasonic fatigue testing. *International journal of fatigue*, 29(9-11):2094–2101.

Mayer, H. (1999). Fatigue crack growth and threshold measurements at very high frequencies. *International materials reviews*, 44(1):1–34.

Mayer, H. (2006). Ultrasonic torsion and tension–compression fatigue testing: Measuring principles and investigations on 2024-t351 aluminium alloy. *International Journal of Fatigue*, 28(11):1446–1455.

Mayer, H. (2016). Recent developments in ultrasonic fatigue. *Fatigue & Fracture of Engineering Materials & Structures*, 39(1):3–29.

Mayer, H., Fitzka, M., and Schuller, R. (2013). Constant and variable amplitude ultrasonic fatigue of 2024-t351 aluminium alloy at different load ratios. *Ultrasonics*, 53(8):1425–1432.

Mayer, H., Schuller, R., Karr, U., Irrasch, D., Fitzka, M., Hahn, M., and Bacher-Höchst, M. (2015). Cyclic torsion very high cycle fatigue of vdsicr spring steel at different load ratios. *International Journal of Fatigue*, 70:322–327.

Montalvão, D. and Wren, A. (2017). Redesigning axial-axial (biaxial) cruciform specimens for very high cycle fatigue ultrasonic testing machines. *Heliyon*, 3(11):e00466.

Nastran, N. (2010). Advanced nonlinear theory and modeling guide.

Nikitin, A., Bathias, C., and Palin-Luc, T. (2015). A new piezoelectric fatigue testing machine in pure torsion for ultrasonic gigacycle fatigue tests: application to forged and extruded titanium alloys. *Fatigue & Fracture of Engineering Materials & Structures*, 38(11):1294–1304.

Pyttel, B., Schwerdt, D., and Berger, C. (2011). Very high cycle fatigue–is there a fatigue limit? *International Journal of fatigue*, 33(1):49–58.

Ritz, F. and Beck, T. (2017). Influence of mean stress and notches on the very high cycle fatigue behaviour and crack initiation of a low-pressure steam turbine steel. *Fatigue & Fracture of Engineering Materials & Structures*, 40(11):1762–1771.

Sakai, T., Sato, Y., Nagano, Y., Takeda, M., and Oguma, N. (2006). Effect of stress ratio on long life fatigue behavior of high carbon chromium bearing steel under axial loading. *International Journal of Fatigue*, 28(11):1547–1554.

Schijve, J. (2003). Fatigue of structures and materials in the 20th century and the state of the art. *International Journal of Fatigue*, 25(8):679–702.

Schuller, R., Mayer, H., Fayard, A., Hahn, M., and Bacher-Höchst, M. (2013). Very high cycle fatigue of vdsicr spring steel under torsional and axial loading. *Materialwissenschaft und Werkstofftechnik*, 44(4):282–289.

Serway, R. A. and Jewett, J. W. (2018). *Physics for scientists and engineers*. Cengage learning.

Soares, H., Costa, P., Freitas, M., and Reis, L. (2018). Fatigue life assessment of a railway wheel material under hcf and vhcf conditions. In *MATEC Web of Conferences*, volume 165, page 09003. EDP Sciences.

Willertz, L. (1980). Ultrasonic fatigue. *International metals reviews*, 25(1):65–78.

Xue, H. and Bathias, C. (2010). Crack path in torsion loading in very high cycle fatigue regime. *Engineering Fracture Mechanics*, 77(11):1866–1873.

Xue, H., Tao, H., Montembault, F., Wang, Q., and Bathias, C. (2007). Development of a three-point bending fatigue testing methodology at 20 khz frequency. *International Journal of Fatigue*, 29(9-11):2085–2093.

Zenner, H. and Hinkelmann, K. (2019). August wöhler–founder of fatigue strength research: On the 200th anniversary of august wöhler's birth. *Steel Construction*, 12(2):156–162.

Appendix A

FEA Results - Displacement and Stress Along the Al7075 Specimen

Table A.1: Displacement distribution along the 7075 alloy specimen. The *reference* value was established as the zero displacement amplitude.

Longitudinal Coord. [mm]	Normalised Displacement Amplitude	Deviation from Reference [%]
0.0	-1.000	-100.00
...	...	...
29.0	-0.168	-16.80
30.4	0.000	0.00
31.8	0.168	16.80
...	...	...
60.8	1.000	100.00

Table A.2: Stress distribution along the 7075 alloy specimen. The *reference* value was established as the zero stress amplitude.

Longitudinal Coord. [mm]	Normalised Stress Amplitude	Absolute Deviation from Reference [%]
0.0	0.002	0.20
1.4	0.007	0.70
...	...	...
29.0	0.965	96.50
30.4	1.000	100.00
31.8	0.965	96.50
...	...	...
59.4	0.007	0.70
60.8	0.002	0.20

Appendix B

FEA Results - Loading Condition 2

Table B.1: Mode shapes and respective resonance frequency for the ultrasonic set comprising the steel specimen under Loading Condition 2.

Mode Shape Identification	Mode Numbering	Resonance Frequency [Hz]
LONGL	1^{st}	15925.2
BNDG	1^{st}	16247.7
LONGL	2^{nd}	16334.7
TOR	1^{st}	16750.1
TOR	2^{nd}	16792.1
LONGL	3^{rd}	19434.5
LONGL	4^{th}	**20182.8**
BNDG	2^{nd}	20666.6
BNDG	3^{rd}	21025.9
BNDG	4^{th}	21471.8

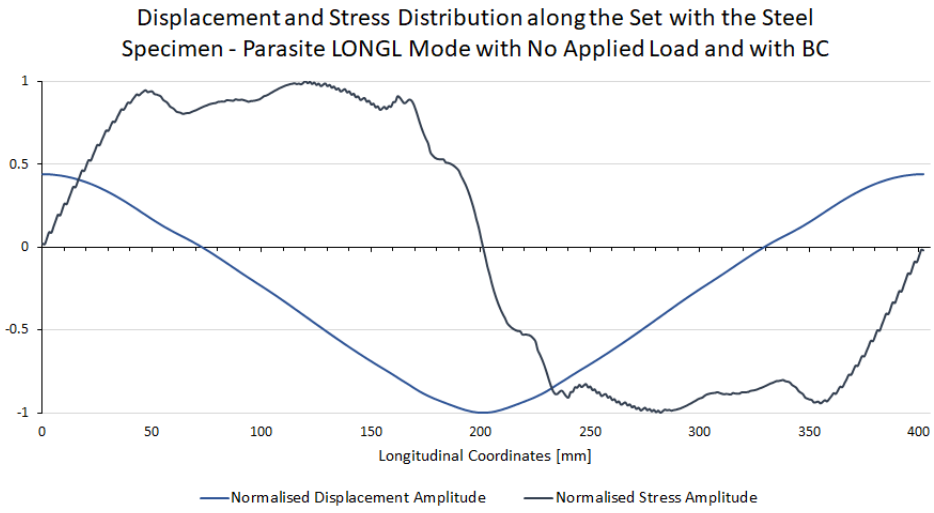

Figure B.1: Displacement and stress distribution of the 3^{rd} longitudinal mode, along the ultrasonic set comprising the steel specimen.

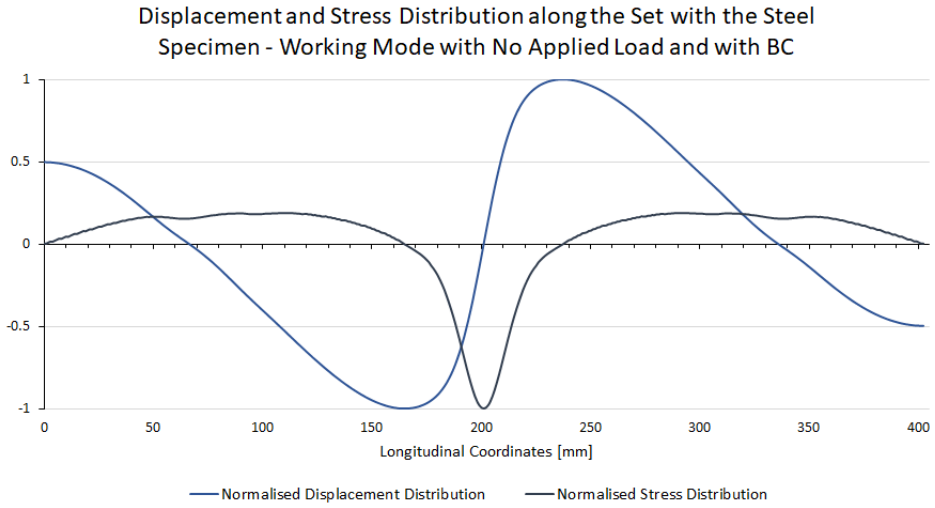

Figure B.2: Displacement and stress distribution of the 4^{th} longitudinal mode, along the ultrasonic set comprising the steel specimen.

Table B.2: Displacement distribution along the ultrasonic set comprising the steel specimen under *Loading Condition 2*. The *reference* value was established as the zero displacement amplitude.

Longitudinal Coord. [mm]	Normalised Displacement	Deviation from Reference [%]
0.0	0.497	49.70
...	...	...
62.0	0.041	4.10
63.0	0.031	3.10
64.0	0.022	2.20
65.0	0.013	1.30
66.0	0.003	0.30
67.0	-0.006	0.60
68.0	-0.016	1.60
...	...	...
165.1	-1.000	100.00
...	...	...
201.1	0.00	0.00
...	...	...
237.1	1.000	100.00
...	...	...
334.2	0.016	1.60
335.2	0.006	0.60
336.2	-0.003	-0.30
337.2	-0.013	-1.30
338.2	-0.022	-2.20
339.2	-0.031	-3.10
340.2	-0.041	-4.10
...	...	...
402.2	-0.497	-49.70

Table B.3: Stress distribution along the ultrasonic set comprising the steel specimen under *Loading Condition 2*. The *reference* value was established as the zero stress amplitude.

Longitudinal Coord. [mm]	Normalised Stress	Deviation from Reference [%]
0.0	0.003	0.30
...	...	...
165.1	-0.002	-0.20
...	...	...
196.1	-0.886	-88.60
197.1	-0.925	-92.50
198.1	-0.957	-95.70
199.1	-0.980	-98.00
200.1	-0.995	-99.50
201.1	-1.00	-100.00
202.1	-0.995	-99.50
203.1	-0.980	-98.00
204.1	-0.957	-95.70
205.1	-0.925	-92.50
206.1	-0.886	-88.60
...	...	...
237.1	-0.002	-0.20
...	...	...
402.2	0.003	0.30

Table B.4: Displacement distribution along the ultrasonic set comprising the 7075 aluminium alloy specimen under *Loading Condition 2*. The *reference* value was established as the zero displacement amplitude.

Longitudinal Coord. [mm]	Normalised Displacement	Deviation from Reference [%]
0.0	0.498	49.80
...	...	...
62.2	0.039	3.90
63.2	0.030	3.00
64.2	0.021	2.10
65.1	0.012	1.20
66.1	0.003	0.30
67.1	-0.006	-0.60
68.0	-0.015	-1.50
...	...	...
165.0	-1.000	100.00
...	...	...
195.4	0.00	0.00
...	...	...
225.8	1.000	100.00
...	...	...
322.8	0.015	1.50
323.7	0.006	0.60
324.7	-0.003	-0.30
325.7	-0.012	-1.20
326.6	-0.021	-2.10
327.6	-0.030	-3.00
328.6	-0.039	-3.90
...	...	...
390.8	-0.498	-49.80

Table B.5: Stress distribution along the ultrasonic set comprising the 7075 aluminium alloy specimen under *Loading Condition 2*. The *reference* value was established as the zero stress amplitude.

Longitudinal Coord. [mm]	Normalised Stress	Deviation from Reference [%]
0.0	0.007	0.70
...	...	...
165.0	-0.001	-0.10
...	...	...
192.5	-0.854	-85.40
193.5	-0.931	-93.10
194.4	-0.980	-98.00
195.4	-1.00	-100.00
196.4	-0.980	-98.00
197.3	-0.931	-93.10
198.3	-0.854	-85.40
...	...	...
225.5	-0.001	-0.10
...	...	...
390.8	0.006	0.70

Appendix C

Experimental Results

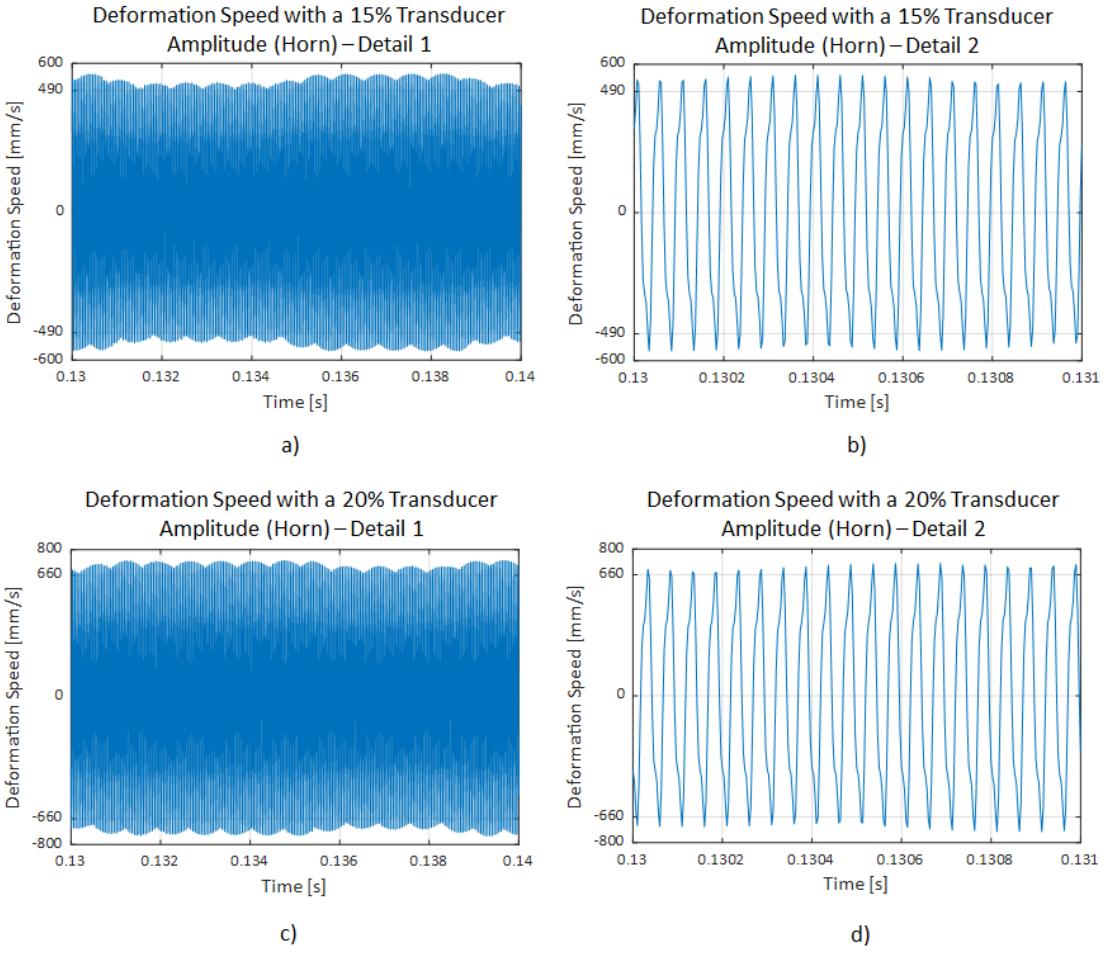

Figure C.1: Deformation speed fluctuations of the system comprising solely one horn at a 15% and 20% transducer amplitude. a) Over the entire test. b) Over a period of 0.001 s.

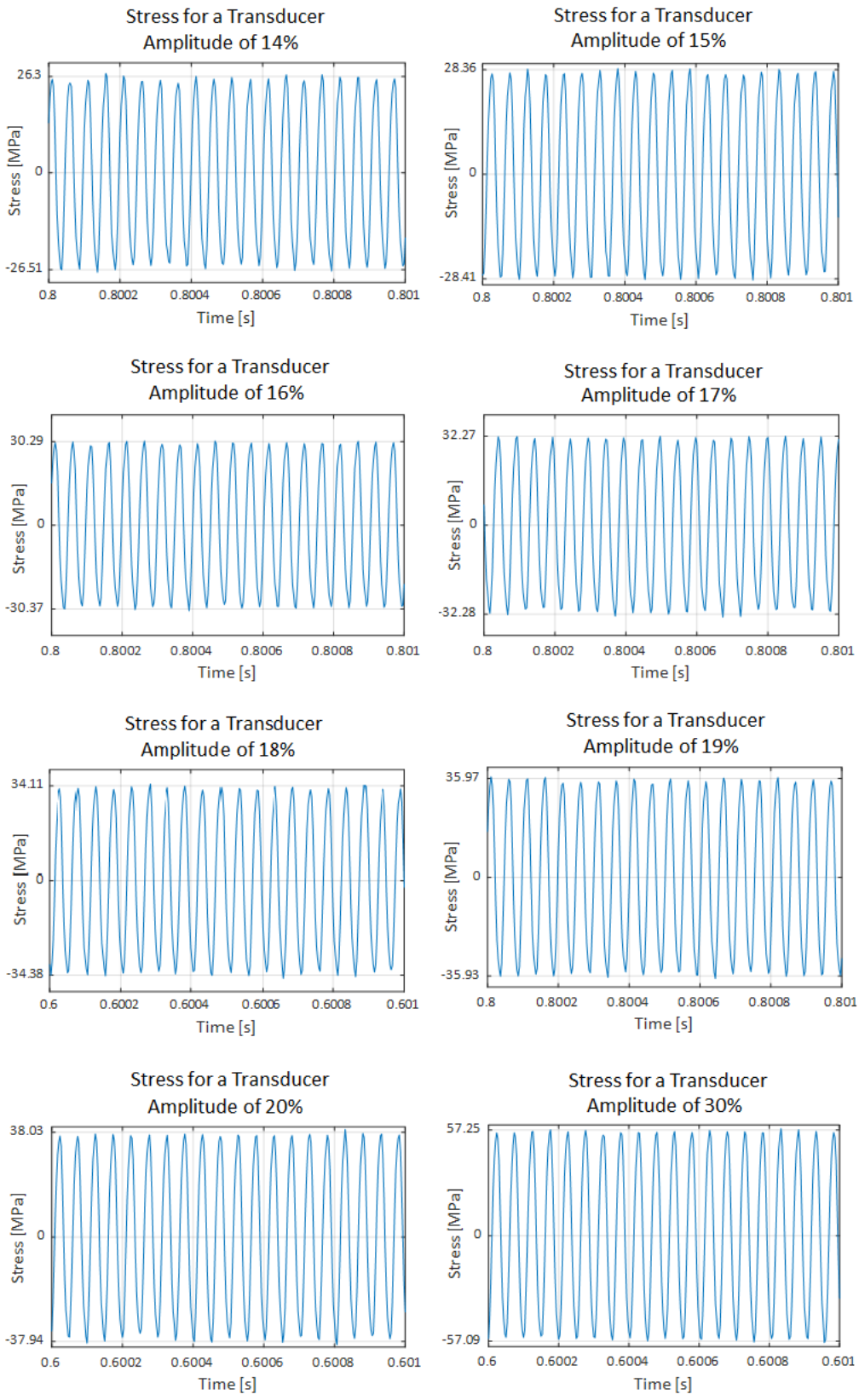

Figure C.2: Stress fluctuations of the complete ultrasonic system under the clamped condition for a transducer amplitude from 14% to 20%, and also for 30%, over a time interval of 0.001 seconds in the stationary regime.